Applied Research Laboratory

④

AD-A193 733

Technical Report

A MULTIPLE-SCALES PARTIAL SOLUTION OF THE
PULSE-FORCED RAYLEIGH-PLESSET EQUATION OF
CAVITATION BUBBLE DYNAMICS

by

B. B. Baker and B. R. Parkin

DTIC
SELECTED
APR 0 8 1988
H

PENNSTATE

1855

88 4 8 031

The Pennsylvania State University
APPLIED RESEARCH LABORATORY
P. O. Box 30
State College, PA   16804

A MULTIPLE-SCALES PARTIAL SOLUTION OF THE
PULSE-FORCED RAYLEIGH-PLESSET EQUATION OF
CAVITATION BUBBLE DYNAMICS

by

B. B. Baker and B. R. Parkin

Technical Report No. TR 88-002

February 1988

ADA193733

REPORT DOCUMENTATION PAGE

1a. REPORT SECURITY CLASSIFICATION Unclassified	1b. RESTRICTIVE MARKINGS
2a. SECURITY CLASSIFICATION AUTHORITY	3 DISTRIBUTION/AVAILABILITY OF REPORT Unlimited
2b. DECLASSIFICATION/DOWNGRADING SCHEDULE	

4 PERFORMING ORGANIZATION REPORT NUMBER(S) TR 88-002	5. MONITORING ORGANIZATION REPORT NUMBER(S)

6a NAME OF PERFORMING ORGANIZATION Applied Research Laboratory The Penna. State University	6b OFFICE SYMBOL (If applicable) ARL	7a. NAME OF MONITORING ORGANIZATION Naval Sea Systems Command Department of the Navy
6c ADDRESS (City, State, and ZIP Code) P. O. Box 30 State College, PA 16804		7b. ADDRESS (City, State, and ZIP Code) Washington, DC 20362

8a. NAME OF FUNDING/SPONSORING ORGANIZATION Naval Sea Systems Command	8b. OFFICE SYMBOL (If applicable) NAVSEA	9. PROCUREMENT INSTRUMENT IDENTIFICATION NUMBER N-00024-85-C-6041

8c. ADDRESS (City, State, and ZIP Code) Department of the Navy Washington, DC 20362	10. SOURCE OF FUNDING NUMBERS			
	PROGRAM ELEMENT NO.	PROJECT NO.	TASK NO.	WORK UNIT ACCESSION NO.

11 TITLE (Include Security Classification)
A Multiple-Scales Partial Solution of the Pulse-Forced
Rayleigh-Plesset Equation of Cavitation Bubble Dynamics

12 PERSONAL AUTHOR(S)
B. B. Baker and B. R. Parkin

13a. TYPE OF REPORT thesis	13b. TIME COVERED FROM _____ TO _____	14. DATE OF REPORT (Year, Month, Day) February 1988	15. PAGE COUNT 163

16 SUPPLEMENTARY NOTATION

17	COSATI CODES		18. SUBJECT TERMS (Continue on reverse if necessary and identify by block number)
FIELD	GROUP	SUB-GROUP	Bubble formation, Cavitation, Fluid Flow, Laminar Flow

19 ABSTRACT (Continue on reverse if necessary and identify by block number)

A partial multiple scales analysis of the forced Rayleigh-
Plesset equation of cavitation bubble dynamics is performed.

Previous studies of cavitation inception on hemispherical

headforms have revealed the existence of "bubble-ring" cavitation

on hemispherical headforms having a laminar separation region.

Nuclei passing through the low pressure region that exists prior

20 DISTRIBUTION/AVAILABILITY OF ABSTRACT ☒ UNCLASSIFIED/UNLIMITED ☐ SAME AS RPT. ☐ DTIC USERS	21. ABSTRACT SECURITY CLASSIFICATION Unlimited
22a NAME OF RESPONSIBLE INDIVIDUAL	22b. TELEPHONE (Include Area Code) 22c. OFFICE SYMBOL

DD FORM 1473, 84 MAR   83 APR edition may be used until exhausted.
All other editions are obsolete.

to the separation bubble experience vaporous growth which is characterized by two time scales. The forcing function pulse which acts on the nuclei is characterized by the "laboratory time" t which varies slowly compared to the characteristic "bubble time" τ which characterizes the response time of a typical microscopic cavitation nucleus.

Expanding the forced Rayleigh-Plesset equation and its initial conditions to the second order in ε, one finds that the zero-order equation is an autonomous nonlinear equation with non-homogeneous initial conditions. The first-order equation is a nonautonomous linear system with homogeneous initial conditions. The second-order equation is a linear autonomous differential equation with homogeneous initial conditions. The second-order equation is needed to establish integrability conditions for the first-order equation.

The zeroth order equation was analyzed in the phase plane which established integration limits. Approximation of the logarithmic air content parameter allowed an approximate solution, $\tau = \tau(u)$, to be found in terms of elliptic integrals and functions. The inverse of this solution could not be found so the inverse $u = u(\tau)$ was found numerically. These data are to be used to find an analytic approximation of future first-order calculations.

By _____

Distribution/

Availability Codes

Dist	Avail and/or Special
A-1	

ABSTRACT

A partial multiple scales analysis of the forced Rayleigh-
Plesset equation of cavitation bubble dynamics is performed.
Previous studies of cavitation inception on hemispherical
headforms have revealed the existence of "bubble-ring" cavitation
on hemispherical headforms having a laminar separation region.
Nuclei passing through the low pressure region that exists prior
to the separation bubble experience vaporous growth which is
characterized by two time scales. The forcing function pulse
which acts on the nuclei is characterized by the "laboratory time"
t which varies slowly compared to the characteristic "bubble time"
τ which characterizes the response time of a typical microscopic
cavitation nucleus.

Expanding the forced Rayleigh-Plesset equation and its
initial conditions to the second order in ϵ, one finds that the
zero-order equation is an autonomous nonlinear equation with
non-homogeneous initial conditions. The first-order equation
is a nonautonomous linear system with homogeneous initial
conditions. The second-order equation is a linear autonomous
differential equation with homogeneous initial conditions. The
second-order equation is needed to establish integrability
conditions for the first-order equation.

The zeroth order equation was analyzed in the phase plane
which established integration limits. Approximation of the
logarithmic air content parameter allowed an approximate
solution, $\tau = \tau(u)$, to be found in terms of elliptic integrals

and functions. The inverse of this solution could not be found so the inverse $u = u(\tau)$ was found numerically. These data are to be used to find an analytic approximation of future first-order calculations.

TABLE OF CONTENTS

TABLE OF CONTENTS [continuation]

LIST OF TABLES

LIST OF FIGURES

LIST OF FIGURES [continuation]

LIST OF FIGURES [continuation]

LIST OF FIGURES [continuation]

NOMENCLATURE

C_p	pressure coefficient $= \dfrac{P - P_o}{1/2\rho V_o^2}$
D	hemispherical headform diameter
$E(\phi, k)$	incomplete elliptic integral of the second kind
$F(\epsilon\tau)$	forcing function
$F(\phi, k)$	incomplete elliptic integral of the first kind
J_p	impulse $= \int F(\epsilon\tau)d(\epsilon\tau)$
K	cavitation number $= \dfrac{P_o - P_v}{1/2\rho V_o^2}$
k	modulus of elliptic functions
k'	complementary modulus of elliptic functions
P	static pressure at any point in the flow
P_a	saturation dissolved air pressure
P_o	free-stream static pressure
P_s	static pressure in the laminar separation bubble
P_v	vapor pressure of water
Q	bubble radius increment, $(Q < 1)$, where $Q = \dfrac{W_r K}{8}$
$R(t)$	bubble radius at any instant
Re	diametral Reynolds number $= \dfrac{V_o D}{\nu}$
Rm	maximum bubble radius
R_o	free-stream nucleus radius
r	dimensionless radius $= \dfrac{R(t)}{R_o}$
s	arc length along headform meridian
Snu, Cdu, ndu	Jacobian elliptic functions
t	"laboratory time"

NOMENCLATURE

t_s, t_f	slow and fast time scales
u	normalized bubble radius $= \dfrac{r}{1 + Q}$
V	potential energy
V_o	free-stream velocity
We	diametral Weber number $= V_o/\sqrt{\sigma/(\rho D)}$
ϵ	small parameter $= \dfrac{1}{T}\sqrt{\dfrac{\rho R_o^3}{2\sigma}}$
γ	air content parameter $= Pa/(\dfrac{2\sigma}{R_o})$
ϕ	modular angle of elliptic functions
ρ	density of water
σ	coefficient of surface tension
τ	"bubble time"
ν	kinematic viscosity of water
ω	vibrational frequency

ACKNOWLEDGMENTS

CHAPTER 1

INTRODUCTION

1.1 Previous Investigation

In this investigation, an analysis of the dynamics of bubble-ring cavitation is performed. The analysis employs perturbation methods for analytically solving the governing nonlinear ordinary differential equation for the flow. In an effort to describe the physical aspects of bubble-ring cavitation, the main phases of bubble growth in a region of laminar separation are discussed.

For a flow about a hemispherical headform containing a laminar separation region, we assume the fluid contains a distribution of nuclei, invisible to the unaided eye, containing air and/or water vapor. These nuclei translate downstream at some velocity close to the free stream velocity, V_0. Some of these will come in contact with the body. When a nucleus moves into the boundary layer on the headform, it will encounter a low pressure region which is favorable to vaporous growth. This low pressure region has a local static pressure less than the vapor pressure within the bubble. The bubble which had an initial radius, R_0, in the free stream will grow to a maximum radius, R_m, after reaching a point on the body where the local static pressure first equals the vapor pressure. The fluid conveys the bubble through the favorable pressure zone so that the collapse phase commences and it is here that the maximum radius occurs. If there is no separation on the body, the bubble will continue to collapse rapidly and violently. For some bodies, however, there can be laminar separation for sufficiently low

Reynolds numbers. Then it seems possible that collapse may not occur and the bubble will come to rest within the laminar separation region where it undergoes further growth by diffusion of air from the liquid into the bubble. This growth continues until the bubble has grown large enough to interact with the free shear layer at the edge of the separation zone. This interaction causes the bubble to translate downstream to the turbulent reattachment region where the intense shear of this region breaks the bubble into froth. As a result, this froth creates a narrow ring of visible cavitation at the downstream end of the separation bubble. This ring is known as bubble-ring cavitation which is a form of attached cavitation and is controlled primarily by laminar boundary layer separation. Figure 1 shows the configuration of a hemispherical headform with a cylindrical afterbody and the laminar separation region located on the headform.

Previous experiments have shown the occurrence of bubble-ring cavitation to be related to several factors. Holl and Carroll [1] observed the variation of the influence of laminar boundary separation for different test models as a principal cause for bubble-ring cavitation. For a model whose configuration creates a large separated region of nearly constant pressure with strong pressure fluctuations in the turbulent reattachment region, bubble-ring cavitation was observed at higher cavitation numbers. Lowering the cavitation number brought on the formation of a more developed state of cavitation called band cavitation. Band cavitation is actually a cavity flow which occurs when the laminar separation region becomes filled with small attached cavities.
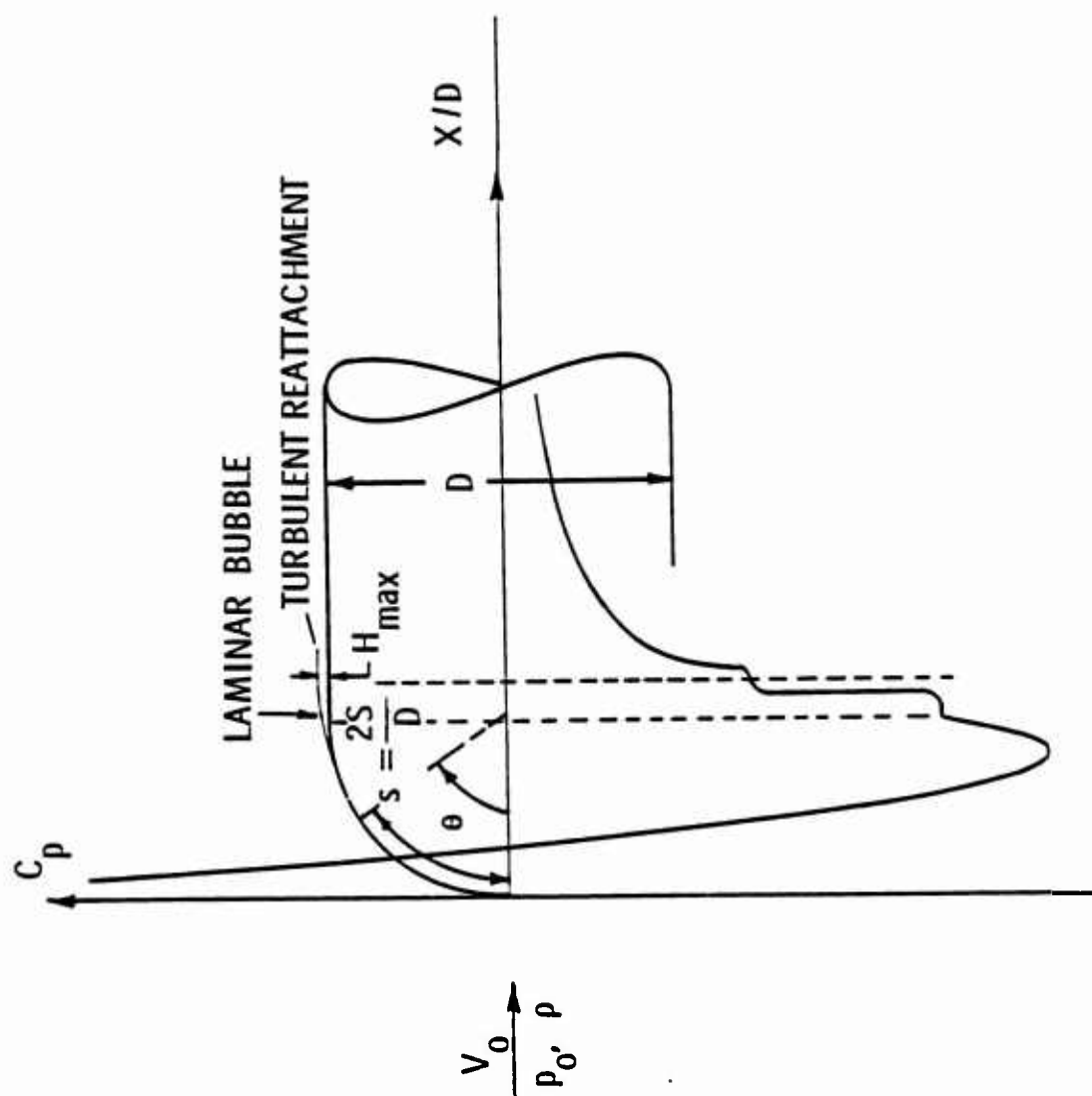
Figure 1. Schematic Diagram of Flow about a Hemispherical Headform when Short Bubble Laminar Separation is Present.

Because bubble-ring cavitation serves as a nuclei source for band cavitation it is important to look at the models on which band cavitation is also formed. Parkin and Holl [3] observed band cavitation on the hemispherical nose and the 1.5 caliber ogive nose. Band cavitation was also observed on a 2.0-inch, 1.0 caliber ogive nose by Carroll [2], a 1.755-inch diameter ITTC nose by Arakeri [4], a 2.0-inch, 1/8 caliber ogive nose[1] by Keller [5] and a 2.0-inch pointed headform used by Brockett [6]. The only models on which bubble-ring cavitation was observed were the hemispherical nose and the 1/8 caliber ogive nose[1] at various flow conditions. For a model whose configuration has a thin separation region with only a slight adverse pressure gradient and small pressure fluctuations at reattachment, bubble-ring cavitation did not exist at all.

Other factors influencing the occurrence of bubble-ring cavitation are the air content and temperature of the water. Carroll [2] observed no bubble-ring cavitation for air contents of less than 4.0 ppm. When the air content was held constant at 8.0 ppm, bubble-ring cavitation was observed to disappear and the limited cavitation number, K_ℓ, decreased when the temperature was increased at low velocities. Since raising the water temperature decreases the solubility of air in water, the number and size of the nuclei should also decrease suggesting that K_ℓ decreases for bubble-ring cavitation. Carroll [2] observed this trend for K_ℓ which suggests that air content is one of the important factors controlling this phenomenon.

---

1. First observed by Robertson, McGinley and Holl [20].

It should be noted that raising the temperature increases the
Reynolds number so that in marginal cases laminar separation
is lost.

Previous investigations by Arakeri [7], Arakeri and Acosta
[8] and van der Meulen [9] of the laminar separation region have
pinpointed the initial separation point to be downstream of the
minimum pressure point $C_{p_{min}}$. The location of the separation
zone did not vary with Reynolds number. Arakeri and Acosta [8]
were the first to verify this with Schlieren photographs of the
thermal boundary layer for velocities up to 60 fps. Arakeri [7]
and Gates [8] experimentally verified a dimensional variation of
the separated region for various Reynolds numbers. The tests
were performed on a 2.0-inch headform and showed a decrease in
size of the separation region with increasing Reynolds number.
This dependence, however, varies with the shape of the headform.

This investigation requires a pressure distribution in the
region of the separation bubble and the minimum pressure point.
A mean pressure distribution for an average free stream velocity
of 40 fps is used. The experimental values for the pressure
coefficient represent averages of the measurements made by
Carroll [2] and were plotted against the dimensionless axial
length X/D. Since it was desired to have the pressure coefficient
data plotted against the dimensionless arc length parameter s,
a conversion was made between X/D and s and is shown in Appendix B.
Figure 2 shows a plot of the pressure coefficient versus the
dimensionless arc length parameter. Figure 3 shows the selected
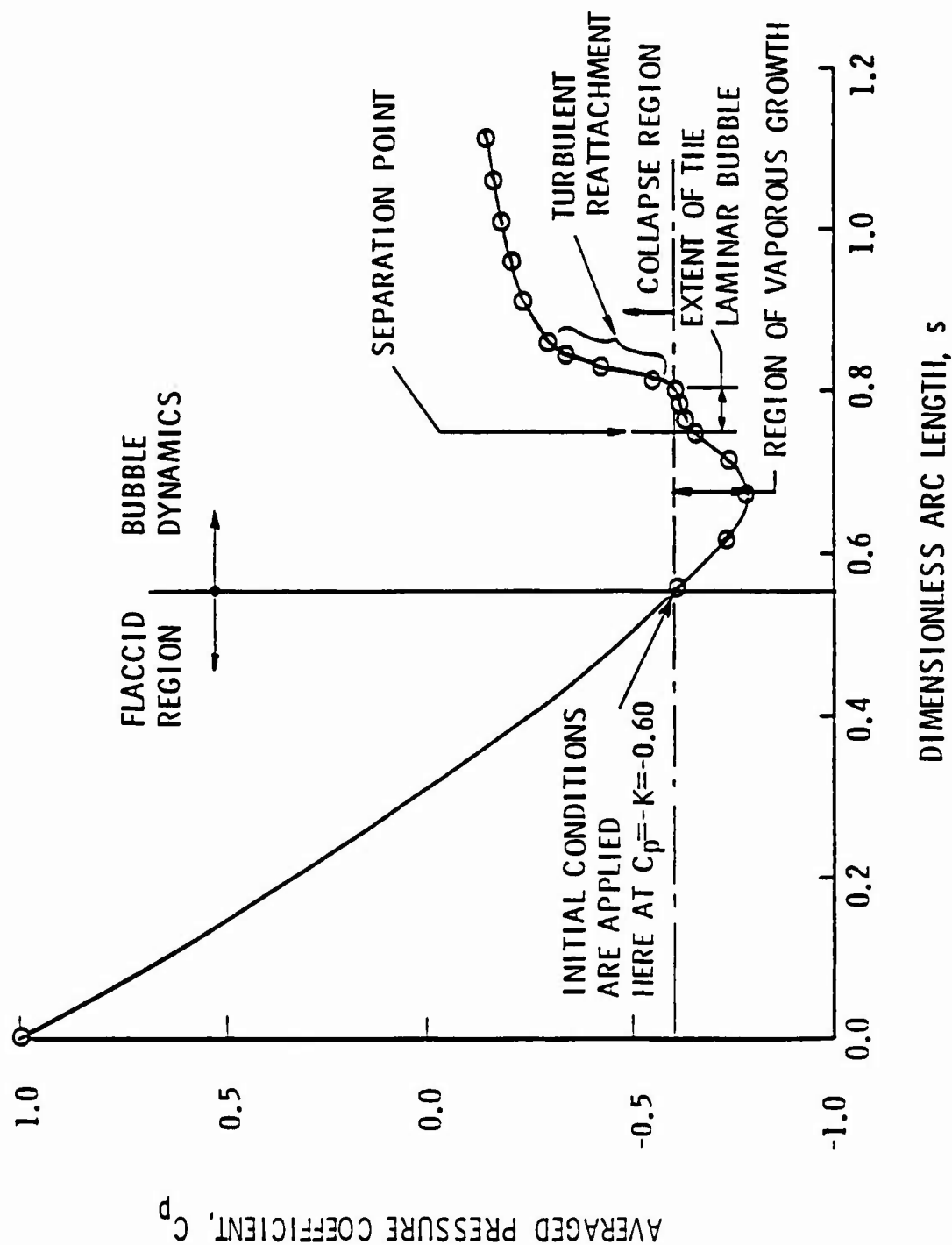
Figure 2. Plot of the Averaged Pressure Coefficient at an Average Velocity of V_o = 40 fps against the Dimensionless Arc Length Position along the Surface of the Hemispherical Headform.
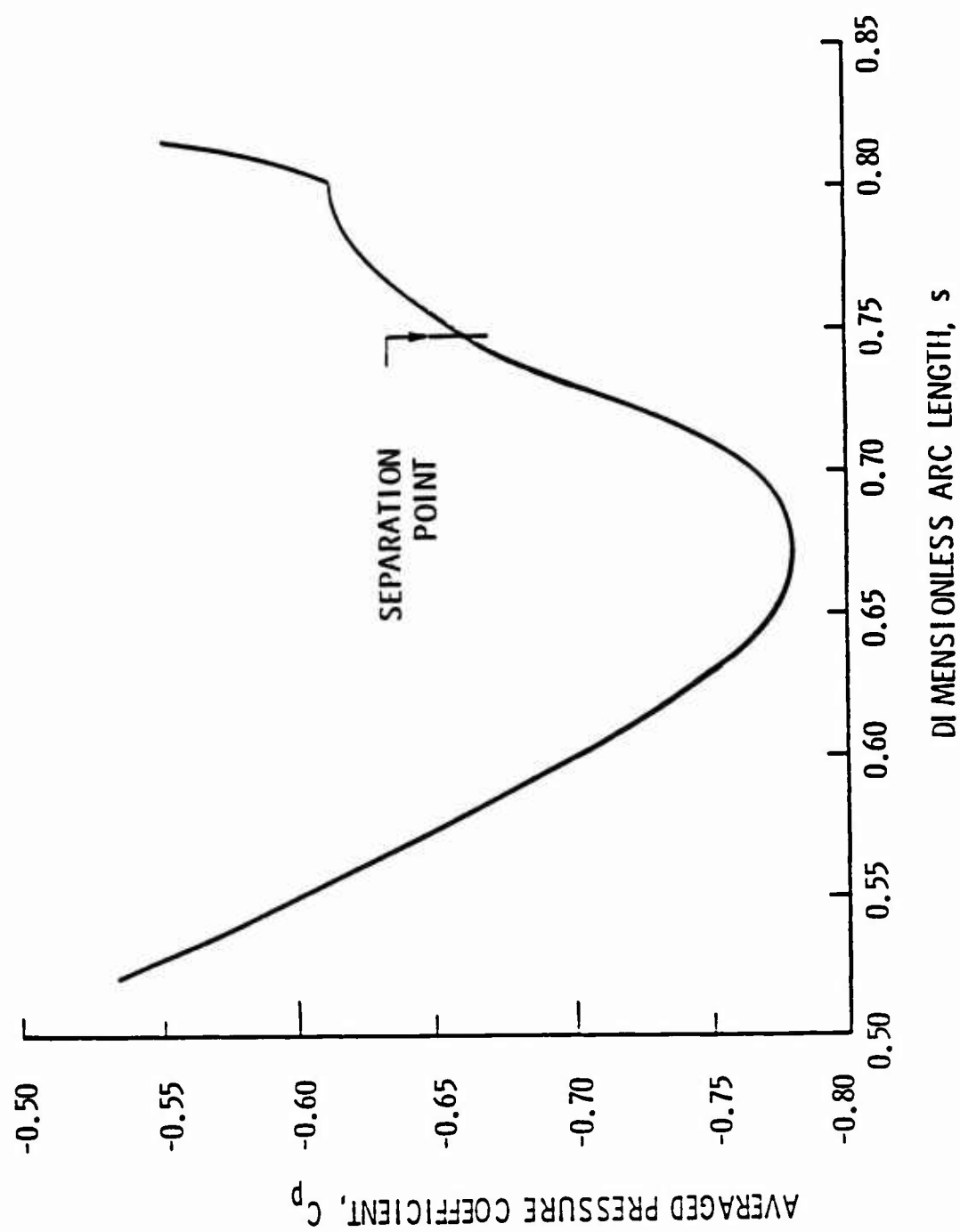
Figure 3. Isolated Section of the Averaged Pressure Coefficient Plot where Vaporous Growth Occurs along the Surface of the Body.

region of the pressure distribution used to analyze the forces that act on the bubbles and encourage the occurrence of vaporous bubble growth. Each figure shows the separation point located downstream of the minimum pressure point at a dimensionless arc length distance of s = 0.747. The location of this separation point agreed with theoretical calculations made by Arakeri and Acosta [8] and van der Meulen [9].

1.2 Scope of this Analysis

The governing equation which describes isothermal cavitation vapor bubble growth or collapse, where the static pressure is taken to be a function of time, is the Rayleigh-Plesset equation. Written in dimensionless form, excluding a viscous term, the isothermal Rayleigh-Plesset equation for a spherical bubble is

$$r \frac{d^2 r}{d\tau^2} + \frac{3}{2} \left(\frac{dr}{d\tau}\right)^2 = \frac{\gamma}{r^3} - \frac{1}{r} + F(\varepsilon\tau) \quad . \tag{1.1}$$

This is the form of the equation used by Parkin [11] and is the same form used in this investigation. It is a second order equation requiring two initial conditions and it is non-autonomous and nonlinear. The forcing function term, $F(\varepsilon\tau)$, is a time dependent pressure force which is responsible for driving the bubble growth. The parameter ε is a dimensionless small parameter of the equation which allows us to relate laboratory time or "real" time, t, to a dimensionless "bubble" time τ.

One can write the small parameter as

$$\varepsilon = \frac{1}{T} \sqrt{\frac{\rho R_o^3}{2\sigma}} \tag{1.2}$$

where

$$T = D/V_o \quad . \tag{1.3}$$

The parameter T is a long time duration which describes the laboratory time scale of the forcing function. The definition of T in Eq. (1.3) allows the small parameter ε to scale automatically with the value of the free stream velocity V_o and the body diameter D. The surface tension coefficient, σ, has units of N/m; the density, ρ, has units of Kg/m^3; and the initial nucleus radius, R_o, has units of meters.

When considering the effect of the forcing function, one must be aware of the characteristic time scales present in this problem. The laboratory time, t, is characterized by a slow time scale which defines a dimensionless time duration across which the forcing function produces an environment favorable for vaporous bubble growth. Thus, the dimensionless slow time scale is of order T and is written

$$t_s = \frac{t}{T} \quad . \tag{1.4}$$

The second time scale present in this problem characterizes the individual bubble oscillations that occur as a bubble passes through a varying pressure fie.d. This fast time scale corresponds to the dimensionless bubble time τ and is written

$$t_f = \tau \quad . \tag{1.5}$$

Using the definition of the small parameter ε as the ratio of the laboratory time to bubble time, one can write

$$\varepsilon = t_s/t_f \quad \text{or} \quad t_s = \varepsilon\tau \ . \tag{1.6}$$

Using Eq. (1.4), one can write

$$\frac{t}{T} = \varepsilon\tau \tag{1.7}$$

which defines the scaling parameter for the forcing function in the vaporous growth region. Relative comparison of the slow and fast time scales shows t_f and t_s to differ in magnitude by a factor of 10^{-3} so that t_f is a very short time duration compared to the time scale t_s which defines the time duration that the forcing function acts in the region of vaporous growth.

Parkin [11] derived an approximate parabolic form of the forcing function making $F(\varepsilon\tau)$ and the governing equation non-autonomous. In an effort to simplify the problem, a suitable combination of two step functions was used in place of the parabolic form making $F(\varepsilon\tau)$ piecewise autonomous and making the differential equation solvable by a suitable numerical method. The choice of the initial conditions was based on the assumption that vaporous growth began with initial radius R_o and $\dot{R}_o = 0$. The autonomous form of the isothermal Rayleigh-Plesset equation was then solved through the region of vaporous growth and to the maximum radius.

In this analysis, the problem was solved using a continuous parabolic representation of the forcing function which was derived from the experimental data of Carroll [2]. Since the parabolic forcing function caused the governing differential equation to be nonautonomous, the solution techniques used by Parkin [11] to

solve the piecewise autonomous Rayleigh-Plesset equation were not fully applicable. We know that initially the bubble acts as a flaccid bubble responding instantaneously to the varying pressure field encountered on the headform. The flaccid bubble region which is primarily used to determine the initial conditions for the dynamical problem has a valid solution only up to the initial point where vaporous growth begins. Beyond the flaccid region the bubble is influenced by the inertia of the fluid surrounding the bubble as well as the varying pressure field. The existence of fast and slow time scales in the region beyond the flaccid region requires an expansion of the governing differential equation as a function of the fast and slow time scales as well as the small parameter ϵ. This variation of the method of multiple scales is called the two-variable expansion procedure and uses a perturbation expansion based on ϵ to separate out the different solutions defining the bubble growth. Application of the two variable expansion procedure produced a series of nonlinear differential equations and initial conditions for only the ϵ^0 approximation. As a result, certain additional judicious approximations were required to put the ϵ^0 solution in a form which enables one to tackle the ϵ^1 and ϵ^2 systems of equations.

1.3 Motivation for the Investigation

Previous experimental investigations which analyzed bubble-ring cavitation on hemispherical headforms have revealed many important details about the particular flow phenomena taking place. As a result of these investigations, the basic fluid dynamics of

this type of flow are fairly well understood. On the analytical side, most attempts at solution of the governing equations are made using canned computer subroutines that produce large amounts of data showing a detailed history of bubble growth or collapse. The difficulty with these mass compilations is revealed when one desires the effect of constraining a particular flow parameter at a particular instant. Analysis can provide the option of looking at different classes of solutions and determining limiting cases of the flow without suffering the expense, frustration and eventual inefficiency of large computer routines. The mathematical techniques being employed are proven and work well with these complex flow equations. Estimates of the form of certain solutions can often be predicted and the existence of much literature on perturbation methods is readily available.

Since the initial attempt to solve the bubble-ring cavitation problem produced quite good agreement between inception data and theory, despite drastic simplifications, it seemed reasonable to assume that if perturbation methods are used one will produce equal to better agreement between theory and experiment. It should be noted that even though this method of solution is more advanced than most other forms of analysis, certain judicious approximations are required to obtain a solution. An effort was made to keep these approximations to a minimum so the true nature of the flow can be seen through the solution of the governing equations. Successful use of this form of analysis may extend the theory's range of applicability and encourage the use of this form of analysis for other types of cavitating flows.

1.4 Objective of this Investigation

The main objective of this investigation is to find a solution
of the nonautonomous form of the isothermal Rayleigh-Plesset
equation by use of appropriate perturbation techniques. To do this,
a thorough parametric formulation of the forcing function, flaccid
bubble radius of growth, flaccid bubble rate of growth of the radius
and initial conditions across a suitable range of cavitation numbers
is performed. It was determined, for cavitation numbers ranging
from $K = 0.600$ to $K = 0.700$, that the initial point of vaporous
growth corresponds to dimensionless arc length positions of
$s = 0.549$ and $s = 0.600$ respectively. The initial conditions, as
derived from the flaccid bubble relations, are applied at the
initial point of vaporous growth. The forcing function, which acts
across the region of vaporous growth, is derived from the experi-
mental data taken by Carroll [2] and is applied at the initial point
of vaporous growth. The effect of the forcing function terminates
at the separation point which corresponds to dimensionless arc
length positions of $s = 0.813$ and $s = 0.731$ for cavitation numbers
of $K = 0.600$ and $K = 0.700$ respectively. After completion of these
tasks, the governing differential equation was expanded using the
method of multiple scales. Of the resulting set of differential
equations, the nonlinear ε^0 system is solved and compared against
a Runge-Kutta solution of the Rayleigh-Plesset equation.
Suggestions are made for further study.

CHAPTER 2

FORMULATION OF THE PROBLEM

2.1 The Flaccid Bubble Problem

The initial description of the problem stated that the bubble
grows as a flaccid balloon, experiencing a state of equilibrium from
the stagnation point up to the initial point of vaporous growth. In
order to formulate the expressions representing the growth of the
bubble, it is necessary to discuss a few of the fundamental
assumptions and relations used in the flaccid bubble problem.

To begin, we must define a dimensionless meridional arc-length
parameter along the hemispherical nose of the body as

$$s = \frac{2S}{D} , \tag{2.1}$$

where S is the dimensional arc length on the body and D is the
diameter of the body. On the cylindrical afterbody, the arc length
is the axial distance, X/D. If we assume the boundary layer to be
a vortex sheet, we can assume its overall translational velocity
to be one half of the local flow speed at the edge of the boundary
layer. Thus, it is approximated as

$$v(s) = \frac{V_o}{2} \sqrt{1 - C_p(s)} . \tag{2.2}$$

Assuming a flaccid bubble nucleus which always stays in the
boundary layer, its convective speed is size independent because
of the assumptions in Eq. (2.2) but it does change size
instantaneously according to the pressure variations. Thus, we
can say

$$v(s) = \frac{dS}{ds} \frac{ds}{dt} \quad, \tag{2.3}$$

where

$$\frac{dS}{ds} = \frac{D}{2} \quad \text{or} \quad dS = \frac{dx}{D} \quad, \tag{2.4}$$

from Eq. (2.1). By substitution of Eq. (2.2) and Eq. (2.4) into Eq. (2.3) and solving for ds/dt, one gets

$$\frac{ds}{dt} = \frac{V_o}{D} \sqrt{1 - C_p(s)} \quad. \tag{2.5}$$

If we call the parameter t, the laboratory time, then we relate this actual time to a dimensionless bubble time by the following relation

$$\tau = \frac{t}{R_o} \sqrt{\frac{2\sigma}{\rho R_o}} \quad, \tag{2.6}$$

where R_o is the nucleus radius measured in the free stream. Then

$$d\tau = \sqrt{\frac{2\sigma}{\rho R_o^3}} \, dt \quad. \tag{2.7}$$

Substituting Eq. (2.5) into Eq. (2.7) and integrating over the range of experimental points, one gets the following equation for the dimensionless bubble time along the arc of the body

$$\tau_i = \frac{D}{V_o} \sqrt{\frac{2\sigma}{\rho R_o^3}} \int_{s_1}^{s_i} \frac{ds}{\sqrt{1 - C_p(s)}} \qquad i = 1, 2, \ldots, n \quad. \tag{2.8}$$

The integral of Eq. (2.8) depends on the experimental data of Holl and Carroll [1]. Development of a computer code that could produce an accurate value of the integral would allow us to correlate the arc length parameter with the bubble time parameter. Care must be taken when evaluating the integral numerically at the stagnation point because it has an integrable square root singularity. Evaluation of this singularity is discussed in Appendix A. The necessary requirements of a computer code to integrate across the range of experimental data are the following:

(1) Produce an accurate curve fit of the integrand using parabolic interpolation between data points,

$$f(s) = As^2 + Bs + C \quad .$$

where the coefficients A, B and C are computed for groups of three successive data points.

(2) Be able to handle an odd or even number of data points.

(3) Integrate the parabolic curve fit using the coefficients A, B and C for each successive triad of data points.

2.1.1 Calculation of the Flaccid Buddle Radius, r(s)

If we consider the isothermal transition of the bubble from the free stream radius R_o, to the radius on the body R_1, then we can write

$$P_a R_o^3 = P_g R_1^3 \quad , \tag{2.9}$$

where P_a is the partial pressure in the free-stream nucleus and P_g is the air partial pressure in the bubble when it has radius R_1. Figure 4 shows a typical nucleus and the internal and external pressures that act on the nucleus. The balance of pressures that act on the bubble in the free stream $(R = R_o)$ is written as

$$P_a + P_v = \frac{2\sigma}{R_o} + P_o \quad , \tag{2.10}$$

where σ is a coefficient of surface tension, P_a is the partial pressure of the dissolved air in the free stream nucleus, P_o is the free stream static pressure which establishes the external environment for the bubble and P_v is the vapor pressure inside the cavitation bubble. On the body $(R = R_1)$ one can write the balance of pressures as

$$P_g + P_v = \frac{2\sigma}{R_1} + P(s) \quad , \tag{2.11}$$

where P_g is the partial pressure of the same mass of gas as was in the nucleus at $R = R_o$, but measured at $R = R_1$ with the size of $R_1(s)$ being dependent upon its location on the headform. The external pressure term, $P(s)$, varies with the arc length of the body. Introducing a dimensionless radius as

$$r = \frac{R_1}{R_o} \quad , \tag{2.12}$$

Eq. (2.11) can be written as

$$P(s) = P_g + P_v - \frac{2\sigma}{R_o} \frac{1}{r} \quad . \tag{2.13}$$

$$\text{EXTERNAL PRESSURES} = \frac{2\sigma}{R} + P_0$$

INTERNAL
PRESSURES $= P_a + P_v$

R
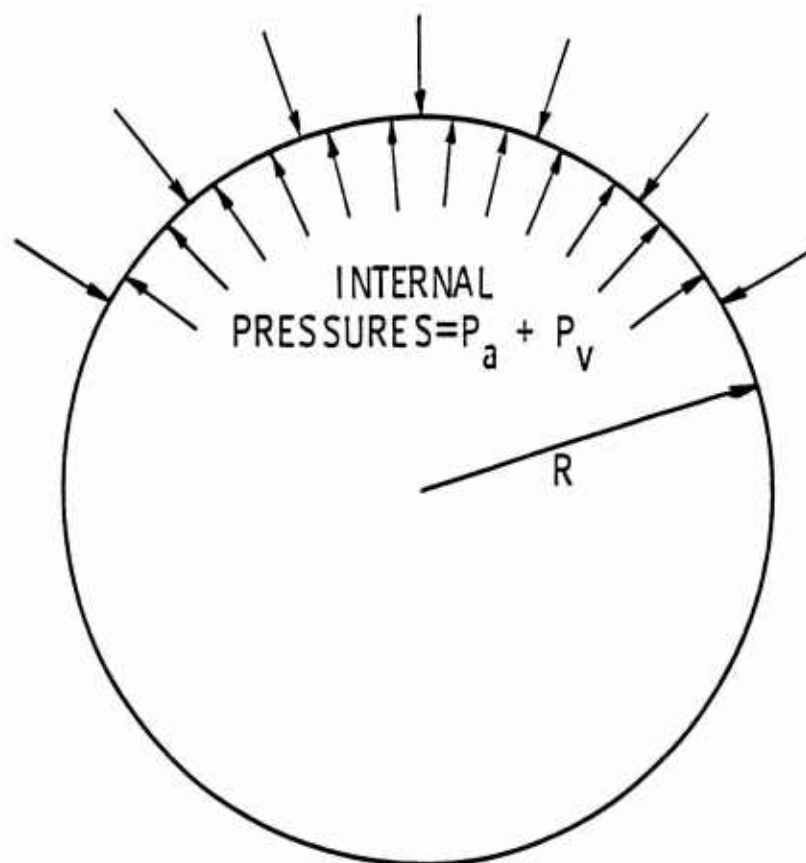
Figure 4. Schematic Diagram of a Typical Nucleus with Internal
and External Pressures that Act on the Nucleus.

Substituting Eqs. (2.10), (2.12) and (2.13) into Eq. (2.9) one can write

$$\left(\frac{2\sigma}{R_o} + P_o - P_v\right)R_o^3 = \left(\frac{2\sigma}{R_o}\frac{1}{r} + P(s) - P_v\right)r^3R_o^3 \quad . \tag{2.14}$$

Using the following definitions for the cavitation number and the pressure coefficient, one has

$$K = \frac{P_o - P_v}{1/2\rho V_o^2} \quad , \tag{2.15}$$

$$C_p = \frac{P(s) - P_o}{1/2\rho V_o^2} \quad . \tag{2.16}$$

Equation (2.14) can be written as

$$\frac{2\sigma}{R_o} + K\left(1/2\rho V_o^2\right) = \left[\frac{2\sigma}{R_o}\frac{1}{r} + \left(C_p + K\right)1/2\rho V_o^2\right]r^3 \quad . \tag{2.17}$$

Multiplying both sides of Eq. (2.17) by $R_o/2\sigma$ and using the definition of the Weber number,

$$We\left(R_o,V_o\right) = \frac{\rho V_o^2 R_o}{\sigma} \quad , \tag{2.18}$$

we write the cubic flaccid-bubble equation as

$$\frac{\left(C_p + K\right)We}{4}r^3 + r^2 - 1 - \frac{KWe}{4} = 0 \quad . \tag{2.19}$$

Equation (2.19) could be solved exactly, but because r is close to unity, an approximation of the form,

$$r = 1 - x \ , \tag{2.20}$$

is used where $0 < x \ll 1$. If one substitutes Eq. (2.20) into (2.19), he gets

$$A\left(- x^3 + 3x^2 - 3x\right) + x^2 - 2x + \frac{C_p We}{4} = 0 \ , \tag{2.21}$$

where

$$A = \frac{(C_p + K)We}{4} \ . \tag{2.22}$$

Because $A < \frac{KWe}{4}$ and $x \ll 1$, the term Ax^3 can be neglected and the remaining quadratic equation,

$$(3A + 1)x^2 - (3A + 2)x + \frac{C_p We}{4} = 0 \ , \tag{2.23}$$

has a solution of the form

$$x = \frac{3A + 2}{2(3A + 1)} \left[1 \pm \sqrt{1 - \frac{(3A + 1)}{(3A + 2)^2} C_p We} \right] \ . \tag{2.24}$$

In the limit as $A \to 0$, the negative square root must be chosen to satisfy the inequality $0 < x \ll 1$, therefore

$$\lim_{A \to 0} x = 1 - \sqrt{1 + \frac{KWe}{4}} \ . \tag{2.25}$$

Using a binomial expansion on the square root term in Eq. (2.25), one can write

$$1 - \sqrt{1 + \frac{KWe}{4}} = 1 - \left(1 + \frac{KWe}{8} - \frac{(KWe)^2}{8(16)} + \ldots\right) \quad , \tag{2.26}$$

which simplifies the expression for x to

$$x = \frac{KWe}{8}\left(- 1 + \frac{KWe}{16}\right) \quad . \tag{2.27}$$

In the limit as $C_p = - K \to 0$, Eq. (2.25) gives $x = 0$ which corresponds to a nucleus traveling in the free stream. The same result can be obtained directly from the cubic flaccid equation for (1) $C_p = - K = 0$ and (2) $C_p = - K \neq 0$.

For $C_p = - K = 0$, Eq. (2.19) simplifies to

$$r^2 - 1 = 0 \quad , \tag{2.28}$$

which has a root of $r = 1$ as we would expect. For $C_p = - K \neq 0$, the cubic term is neglected as before and the equation for r is written as

$$r^2 - 1 - \frac{KWe}{4} = 0 \tag{2.29}$$

or

$$r = \sqrt{1 + \frac{KWe}{4}} = 1 - x \quad . \tag{2.30}$$

Therefore,

$$x = 1 - \sqrt{1 + \frac{KWe}{4}} \quad , \tag{2.31}$$

which exactly agrees with Eq. (2.25). A check of the validity of Eq. (2.31) was made by solving Eq. (2.19) for C_p and substituting computed values of r from Eq. (2.29) at different cavitation numbers. The computed values of C_p were then compared with the

experimental C_p data. It is clear from Fig. 5 that there is good agreement between the values of C_p calculated from the cubic flaccid equation and the experimental data. Thus, Eq. (2.31) is accurate enough to be a useful expression for x.

Calculation of r(s) can now be made from the stagnation point up to the initial point of the vaporous growth region from Eqs. (2.20) and (2.24). Substitution of (2.22) and (2.24) into (2.20) gives an expression for r in terms of C_p, K and We. The equation

$$r = \frac{3(C_p + K)We}{8 + 6(C_p + K)We} \left[1 \pm \sqrt{1 - \frac{12(C_p + K)We + 16}{\left(3(C_p + K)We + 8\right)^2} C_p We} \right] ,$$

(2.32)

is plotted for various values of K in Fig. 6. Calculation of r for various cavitation numbers is necessary in the derivation of the initial conditions which is performed in a later section.

2.1.2 Calculation of the Flaccid Bubble Growth Rate, $\dot{r}(s)$

Another important facet of the flaccid bubble problem is the bubble growth rate $\dot{r}(s)$ where

$$\dot{r}(s) = \frac{dr(s)}{d\tau} .$$

(2.33)

Because the bubble is conveyed toward a region where the changing external pressure directly affects the radius and therefore the rate of growth of the radius, we say the growth rate is given by

$$\dot{r} = \frac{dr}{dC_p} \frac{dC_p}{ds} \frac{ds}{d\tau} .$$

(2.34)
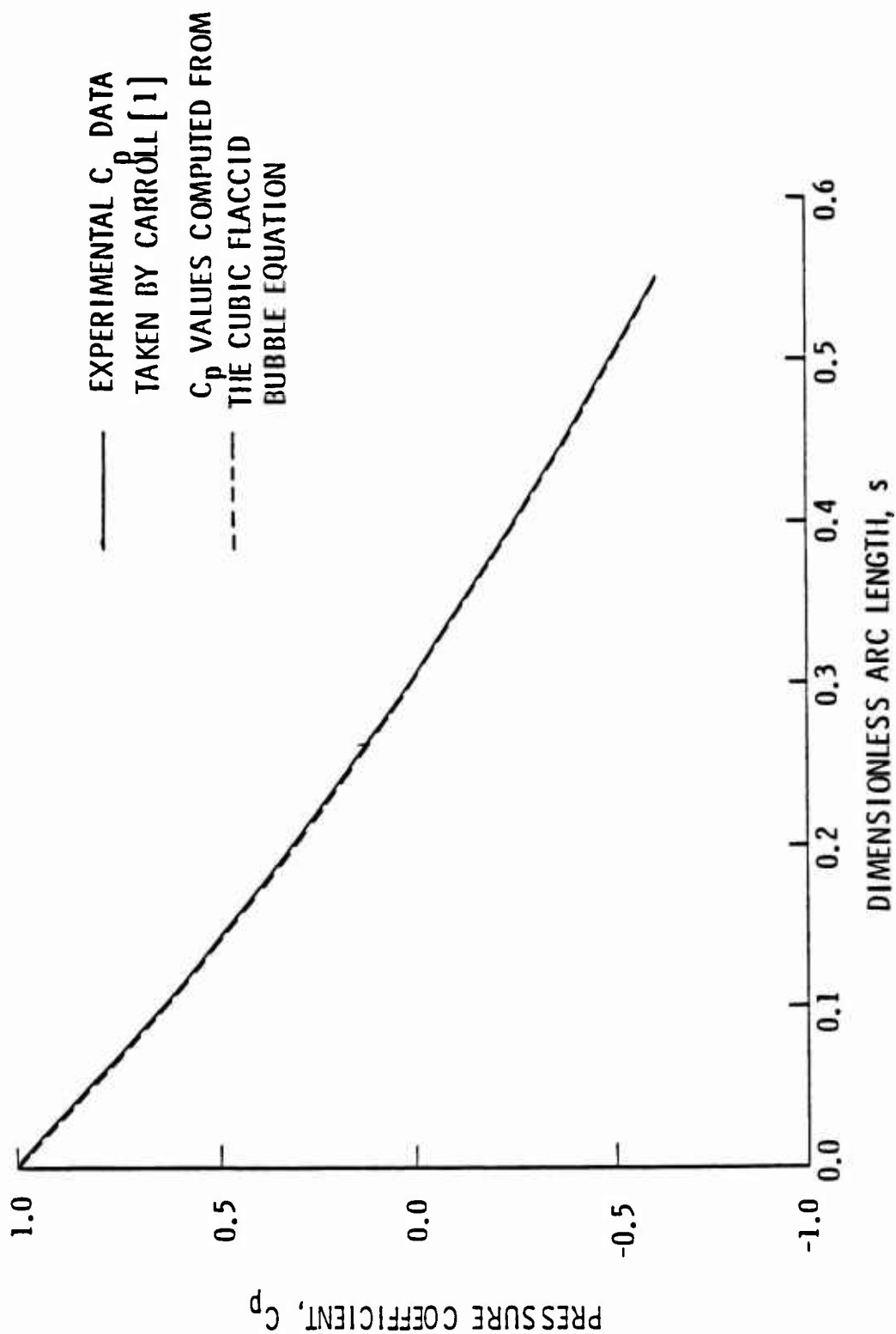
Figure 5. Comparison of the Experimental C_p Data against Values of C_p Calculated from the Cubic-Flaccid Bubble Equation.

24
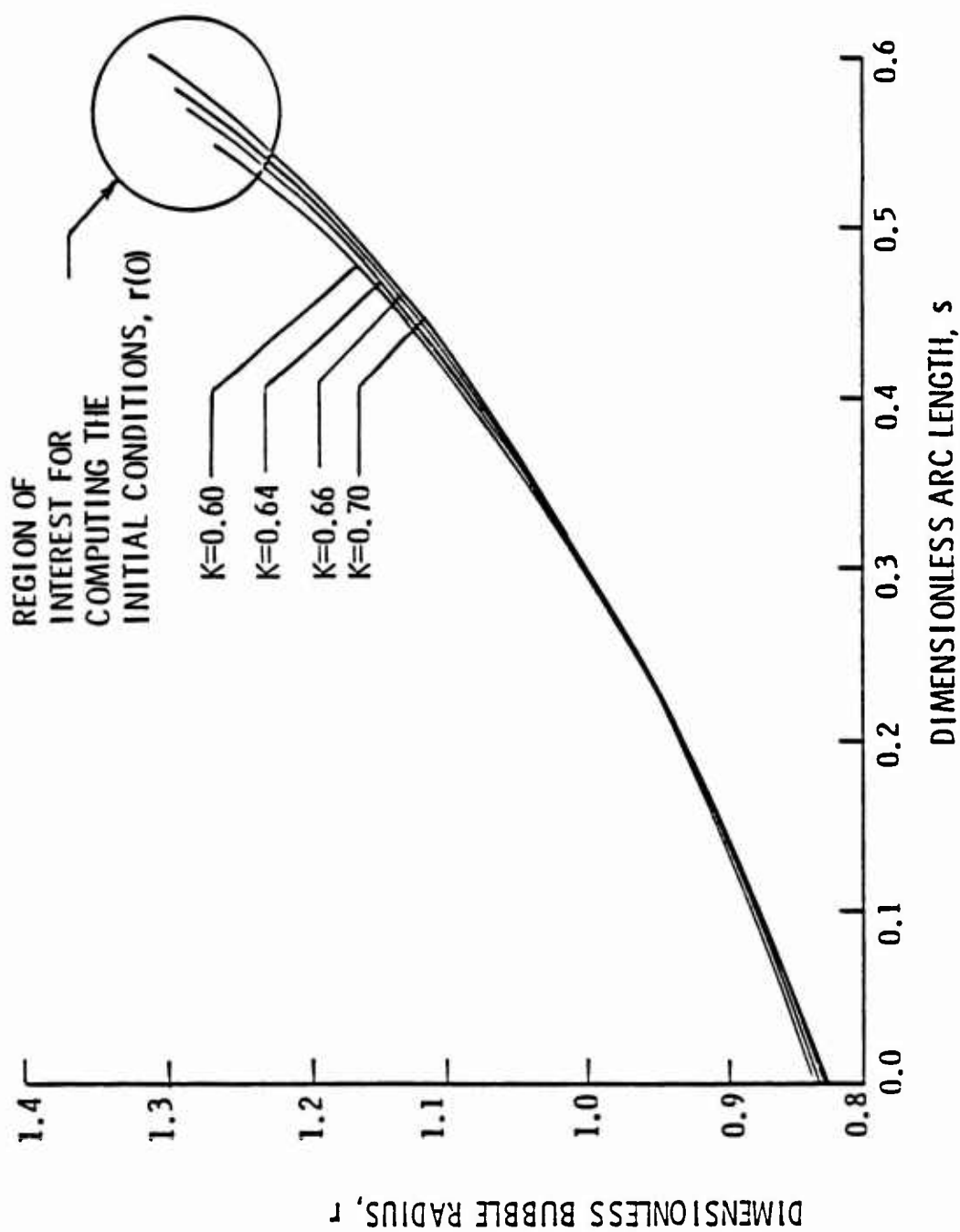
Figure 6. Plot of the Dimensionless Bubble Radius versus the Dimensionless Arc Length within the Flaccid Bubble Region for Cavitation Numbers of K = 0.60 → K = 0.70.

Derivation of each component derivative in Eq. (2.34) results in an expression for r(s). Writing the cubic flaccid bubble equation as

$$\frac{(C_p + K)We}{4} r^3 + r^2 - 1 - \frac{KWe}{4} = 0 \tag{2.35}$$

and using implicit differentiation of Eq. (2.35), one gets

$$\frac{(C_p + K)We}{4} 3r^2 \frac{dr}{dC_p} + r^3 \frac{We}{4} + 2r \frac{dr}{dC_p} = 0 \quad . \tag{2.36}$$

Solving for dr/dC_p, one has

$$\frac{dr}{dC_p} = - \frac{r^3 We}{3r^2(C_p + K)We + 8r} \tag{2.37}$$

which is dependent on the experimental data and the bubble radius r(s).

The term dC_p/ds depends on the approximated parabolic form of the experimental data which is

$$C_p(s) = As^2 + Bs + C \quad . \tag{2.38}$$

If one differentiates $C_p(s)$, he finds that

$$\frac{dC_p}{ds} = 2As + B \quad . \tag{2.38}$$

Finally, we know the differential form of the expression for the dimensionless time parameter is written as

$$d\tau = \sqrt{\frac{2\sigma}{\rho R_o^3}} \frac{D}{V_o} \frac{ds}{\sqrt{1 - C_p(s)}} \quad , \qquad (2.39)$$

where the term $D/V_o = T$ is the characteristic measure of laboratory time t, as defined by Eq. (1.3). Referring to Eqs. (1.2) and (1.3) and rearranging for $ds/d\tau$, one gets

$$\frac{ds}{d\tau} = \frac{1}{T} \sqrt{\frac{\rho R_o^3}{2\sigma}} \sqrt{1 - C_p(s)} \qquad (2.40)$$

$$= \epsilon \sqrt{1 - C_p(s)}$$

where ϵ is defined by Eq. (1.2). By substitution of Eqs. (2.37), (2.38) and (2.40) into (2.34), one gets

$$\dot{r}(s) = \frac{(2As + B)r^2 We^{3/2} \frac{R_o}{D} \sqrt{1/2(1 - C_p(s))}}{8 + 3r(C_p + K)We} \qquad (2.41)$$

The sign of $\dot{r}(s)$ depends on what the sign and magnitude of the parabolic coefficients are. Calculations for $\dot{r}(s)$ using the values of $r(s)$ and the parabolic coefficients up to the beginning of the vaporous growth region give the curves shown in Fig. 7 at $K = 0.60 \rightarrow K = 0.70$.
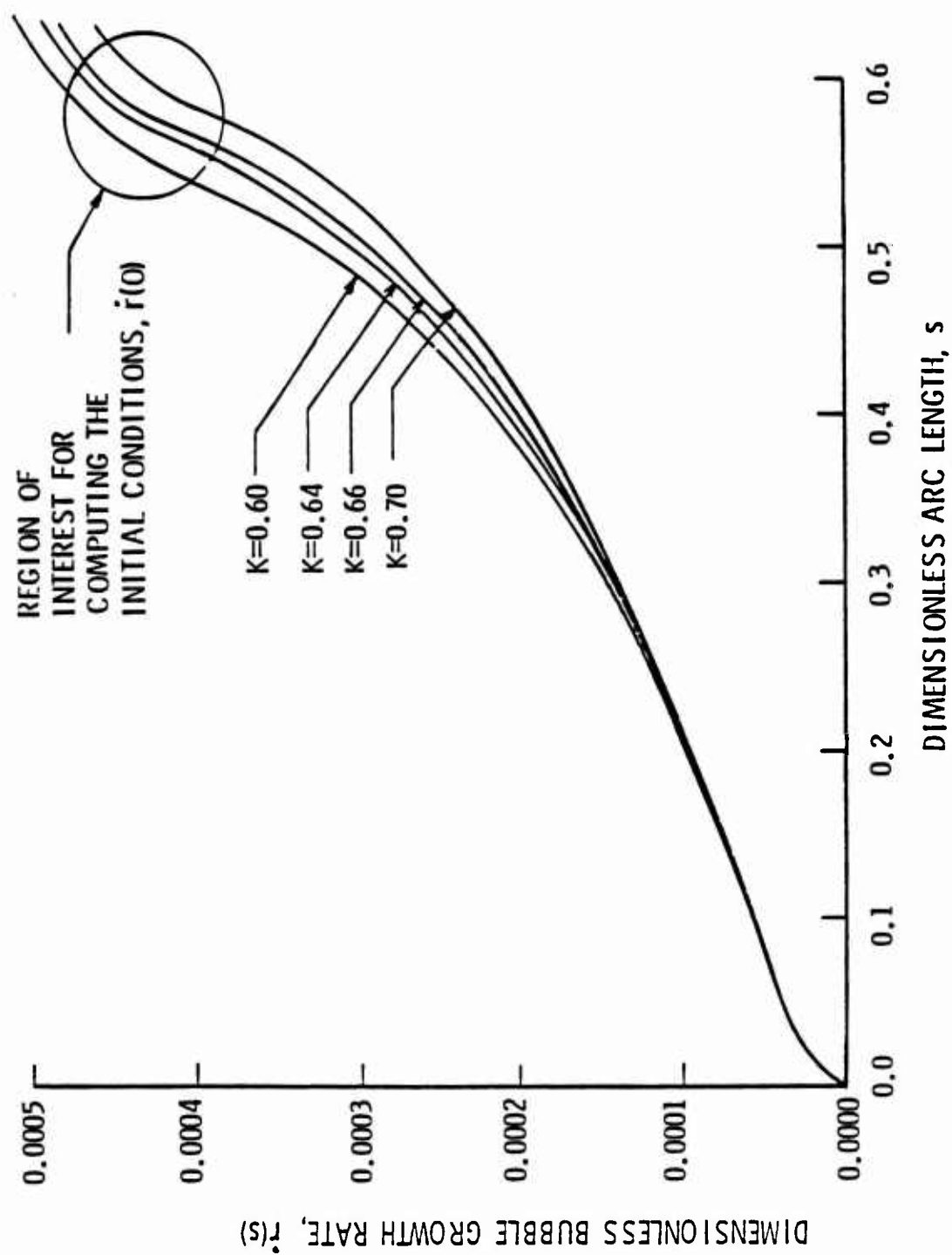
Figure 7. Plot of the Dimensionless Bubble Radius Growth Rate versus the Dimensionless Arc Length within the Flaccid Bubble Region for Cavitation Numbers of K = 0.60 → K = 0.70.

2.2 The Forcing Function

2.2.1 Definition of the Forcing Function

As we discuss the translation of the bubbles over a headform, we must be aware of the driving force which creates the environment for subsequent vaporous bubble growth and collapse. We have discussed the fact that for vaporous growth to occur there must be a region on the headform where the static pressure of the flow is less than the vapor pressure of the water. This region starts on the headform at various arc length positions depending on the choice of the cavitation number. Downstream of the initial point of this growth region the pressure is characterized by the inequality,

$$P_v > P > P_{min} \tag{2.42}$$

or

$$K > - C_p(s) > - C_{P_{min}} \quad . \tag{2.43}$$

Equation (2.43) suggests that the negative of the pressure coefficient can be used to measure the force on the bubble that causes vaporous growth.

If the bubble collapses, then we write the inequality as

$$K < - C_p(s) \quad . \tag{2.44}$$

Thus, we can set the zero of the forcing function at

$$C_p = - K \tag{2.45}$$

and define the forcing function which acts on the bubbles as $F(\varepsilon\tau)$ where

$$F(\epsilon\tau) = -C_p(s) - K = -\left(C_p(s) + K\right) \quad . \tag{2.46}$$

It should be noted in this particular case that the region of vaporous growth and collapse extends along the arc of the body only as far as the separation point of the laminar separation region. Once the bubbles enter the separation region we assume that the process of vaporous growth terminates and the growth that ensues is due to diffusion of air from the liquid into the bubble. The forcing function which is derived from the pressure distribution can be defined along the entire arc of the body, but will be used in this study only up to the separation point. Figure 8 is a schematic diagram of the forcing function with its vaporous growth and collapse regions. The beginning of the positive growth region is located at the intersection of the line of $C_p = -K$ and the forcing function. This initial point, where $F = 0$, is designated as the origin of the forcing function. The horizontal axis which coincides with the line $C_p = -K$ defines the shifted $\epsilon\tau$ axis along which the duration of the vaporous growth process is measured. As shown in Appendix B, this dimensionless time parameter, which is used to scale the forcing function, is derived from the dimensionless arc length parameter and has a zero value at the origin of the $\epsilon\tau - F$ coordinates. Growth or collapse is designated by $\epsilon\tau > 0$ up to the point of separation beyond which no more vaporous growth takes place.

When we consider different flow conditions causing the cavitation number to change, the line where $C_p = -K$ shifts up or down depending on the magnitude of K. For increasing values of K, the line of $C_p = -K$ shifts upwards, decreasing the positive
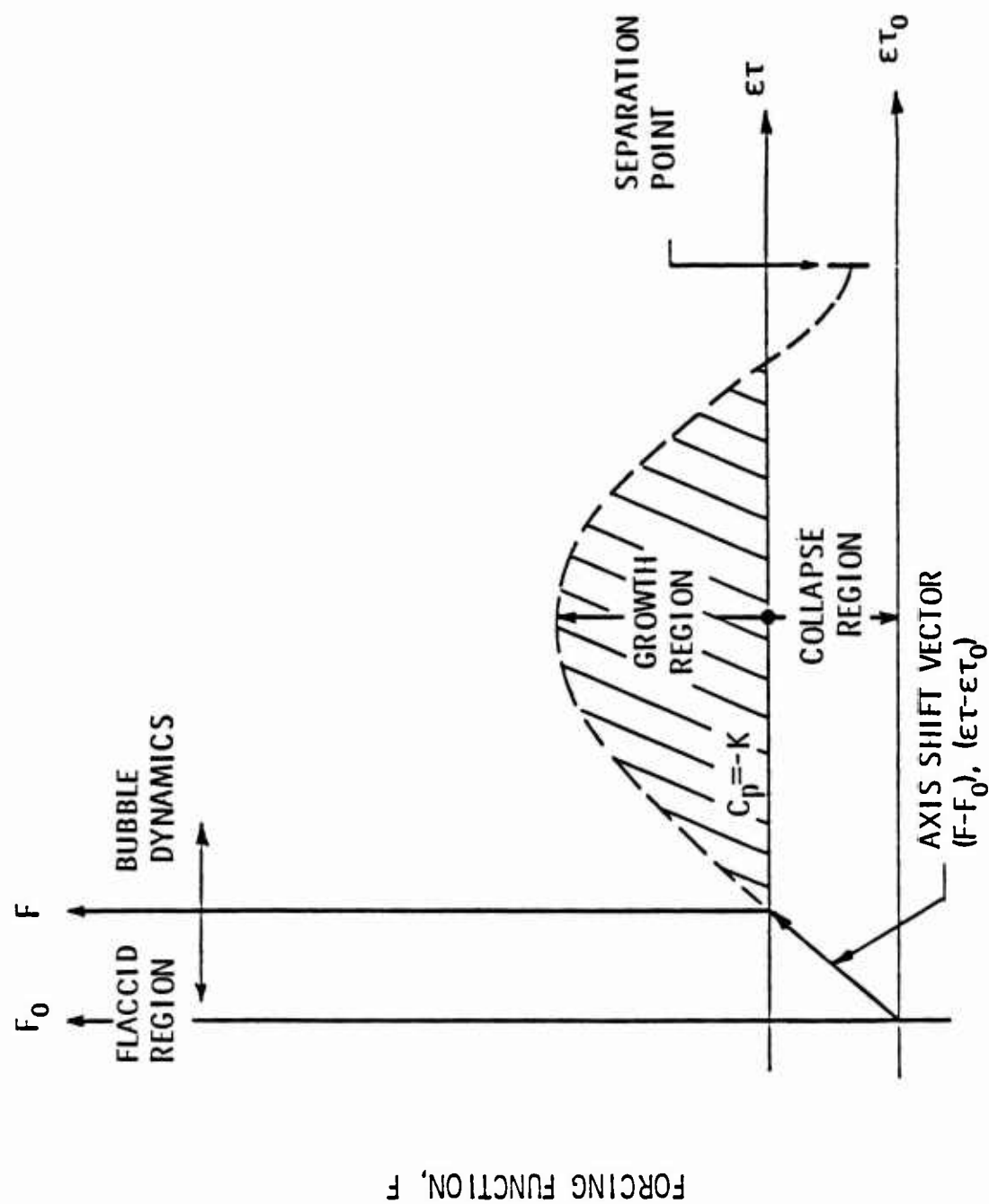
Figure 8. Schematic Diagram of the Forcing Function with its Growth and Collapse Regions and Axis Shift Vector Labeled.

vaporous growth region and increasing the negative collapse region. The opposite trend occurs when the value of K is decreased resulting in a downward shift of the line $C_p = -K$. In view of the location of the separation point and the value of the pressure coefficient at separation, choosing $K = -C_p$ at separation results in a favorable region for vaporous growth which is entirely positive. As stated earlier, separation occurs at a dimensionless arc length which corresponds to $C_p = -0.6597$. Thus, positive growth exists for all values of $C_p < -0.6597$ and growth and collapse occurs for $-0.6597 > C_p > C_{p_{min}}$. Figure 9 shows the selected region of the forcing function calculated from the experimental data of Carroll [2] across the region of vaporous growth for various values of the cavitation number.

2.2.2 Axis Shift for the Forcing Function

It was seen that by choosing different values of the cavitation number, significant changes in the forcing function take place with respect to the regions of growth and collapse. Accompanying this change in the growth and collapse regions is a shift in the origin of the forcing function which is defined as $F = 0$ at $\varepsilon\tau = 0$. As the line of $C_p = -K$ moves up or down, the origin of the forcing function translates along both the F axis and the $\varepsilon\tau$ axis. Figure 8 shows the line along which the axis shift takes place. It is important to know how much the origin translates for various cavitation numbers so that the analysis can be generalized for varying conditions. For the range of cavitation numbers being investigated, $K = 0.60$ to
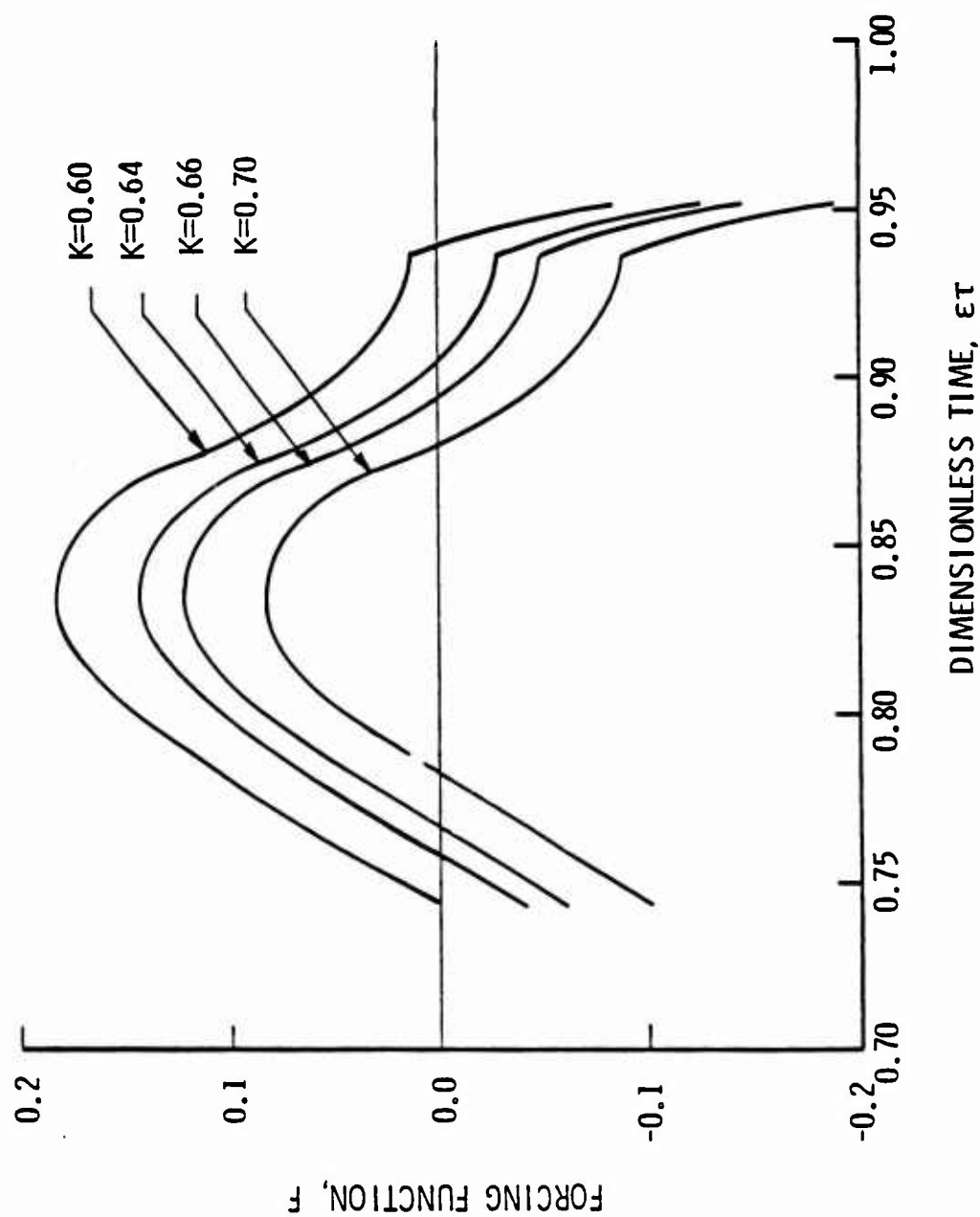
Figure 9.   Plot of the Select Region of the Forcing Function where Vaporous Growth Occurs for K = 0.60 → K = 0.70.

$K = 0.70$, the curve along which the axis shift occurs is a straight line. To define accurately the axis shift it is necessary to determine the variation of F and $\varepsilon\tau$ with respect to the cavitation number.

From Figure 10, the linear portion of the forcing function between the origin and the line $C_p = - K = - 0.70$ is the line along which the axis shifts. The equation defining this line is

$$F = 2.5954(\varepsilon\tau) \tag{2.47}$$

which can be expressed in terms of the cavitation number by the relation

$$\varepsilon\tau = 0.39276(K) - 0.23566 \quad . \tag{2.48}$$

Equation (2.48) defines the $\varepsilon\tau$ parameter along the line of axis shift for cavitation numbers between $K = 0.60$ and $K = 0.70$. Therefore, one can write

$$F = 1.01937(K) - 0.61162 \tag{2.49}$$

for $K = 0.60$ to $K = 0.70$. The reader may refer to Appendix B for the procedure used to calculate Eqs. (2.47) and (2.48). Equations (2.48) and (2.49) define the shift of the origin for different values of the cavitation number. Use of the axis shift is incorporated into the final formulation of the forcing function which is approximated by two different parabolic curve fits. It should be noted that the parameter $\varepsilon\tau$ is being used because of the forcing function dependence on the single power of the small parameter ε. Figure 11 shows a plot of the forcing function for
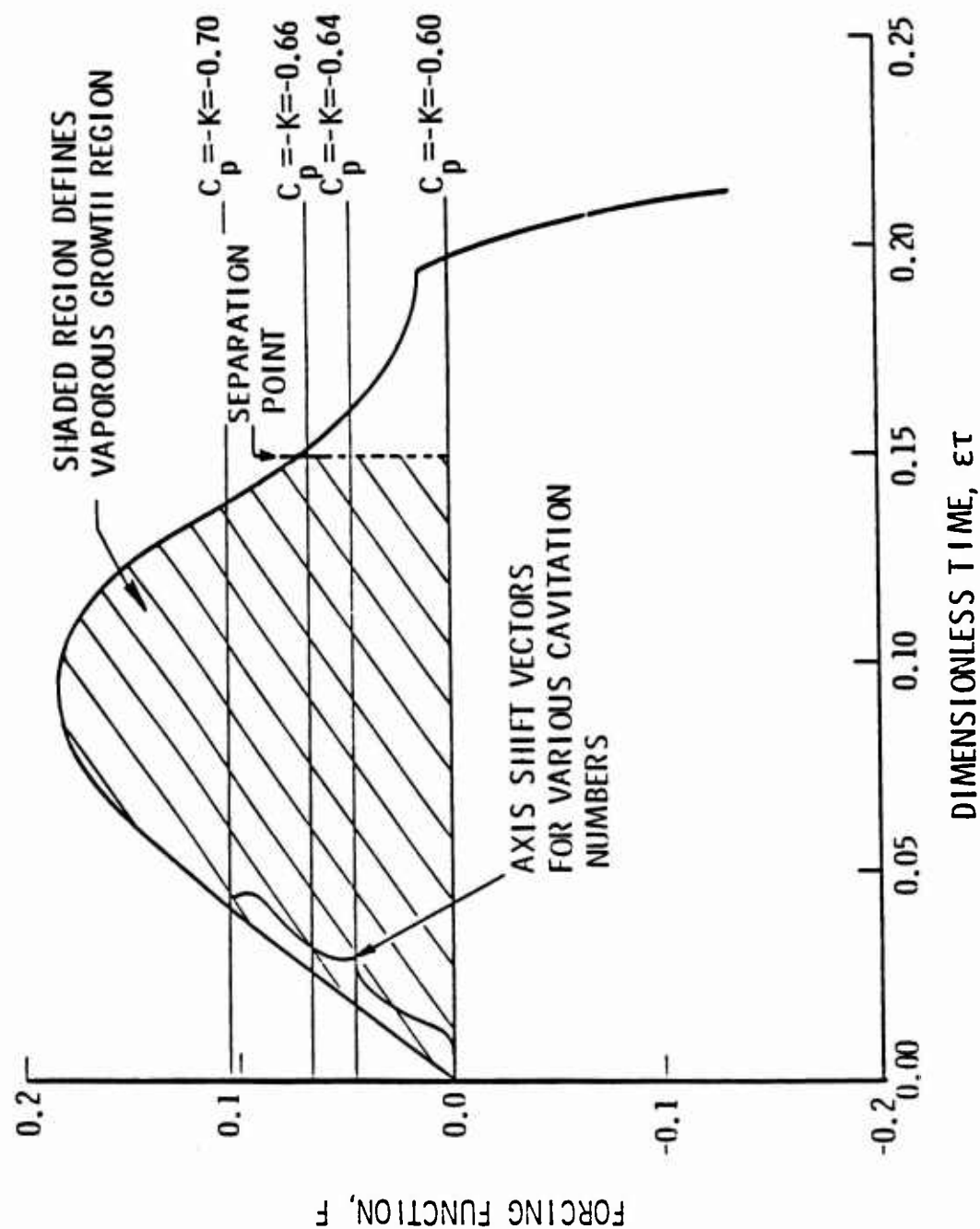
Figure 10. Plot of the Forcing Function versus the Dimensionless Time with Lines of $C_p = -K$ Superimposed on Top.
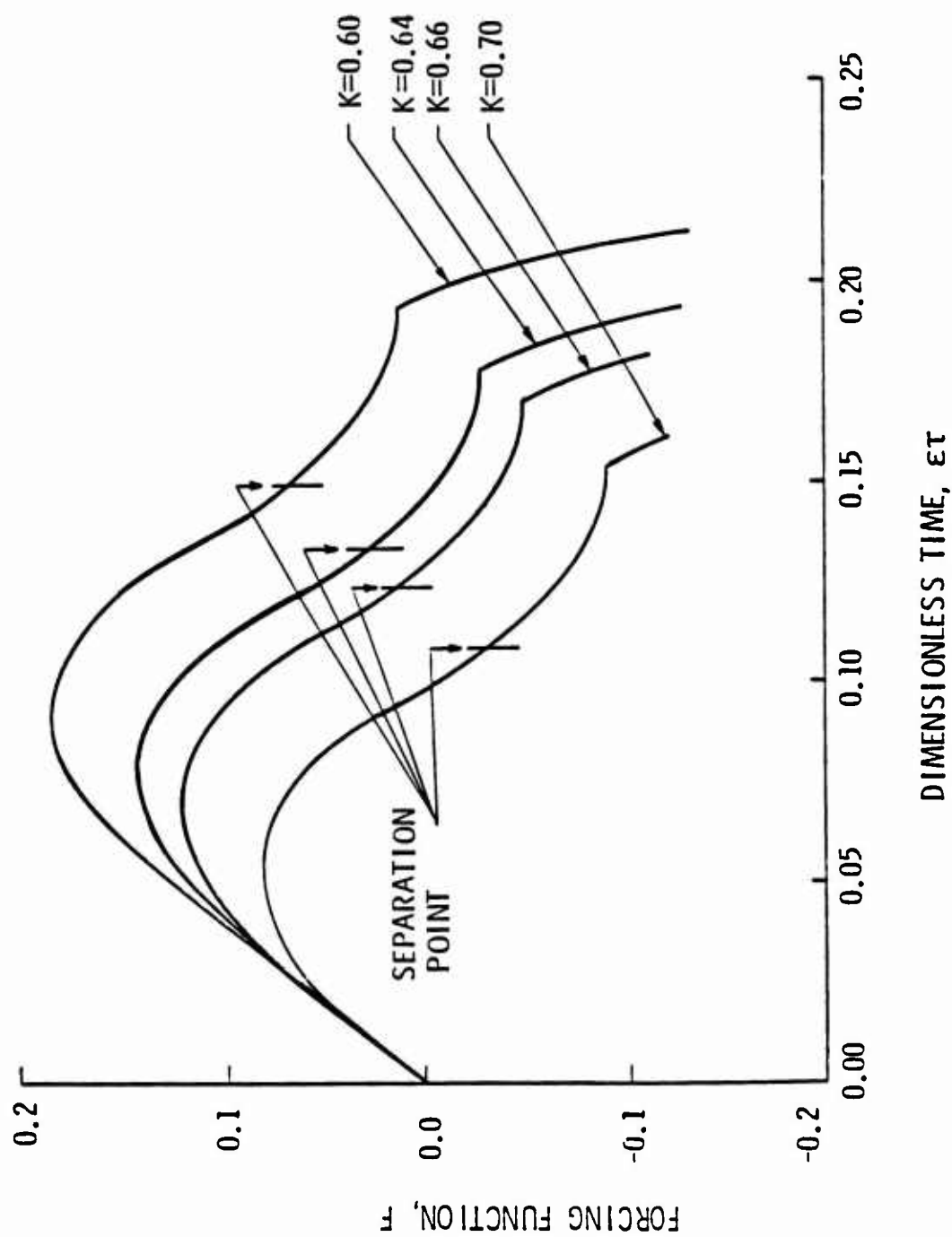
Figure 11. Plot of the Forcing Function versus Dimensionless Time after the Axis Shift on the τ-F Coordinates has been Applied.

various values of the cavitation number after the axis shift has

been applied. It is clear from the curves shown in Fig. 9 that

the axis shift places the initial point of each curve at a common

origin. Thus, we are able to see clearly the effect of the forcing

function for different cavitation numbers. Larger values of the

cavitation number will cause the forcing function to have a negative

effect near the separation point while smaller values of the

cavitation number will make the forcing function entirely positive

across the vaporous region. Choosing a cavitation number greater

than or equal to the negative of $C_{p_{min}}$ would result in zero

vaporous growth for a nucleus as it translates along the body.

2.2.3 Parabolic Curve Fit of the Forcing Function

Previous analysis of this problem was performed by Parkin [11]

in which the forcing function term included within the Rayleigh-

Plesset equation was approximated by a combination of step

functions. Using the definition of the forcing function given in

Eq. (2.46), three parabolic approximations were made to simplify

the solution of the Rayleigh-Plesset equation.

2.2.3.1 Piecewise Parabolic Curve Fit

In the same manner that the experimental data were

approximated by a piecewise parabolic curve fit, the forcing

function was approximated by the same method. Using Eq. (2.46),

values of F were computed for various cavitation numbers.

Parkin [11] scaled the "bubble" time parameter τ against the

laboratory time parameter t by a small parameter which we call

ϵ, where

$$\epsilon = \frac{1}{T}\sqrt{\frac{\rho R_o^3}{2\sigma}} \; .$$

Writing Eq. (2.8) as

$$\tau = \frac{D}{V_o}\sqrt{\frac{2\sigma}{\rho R_o^3}}\, I(s) \tag{2.50}$$

where

$$I(s) = \int_{s_1}^{s_1} \frac{ds}{\sqrt{1 - C_p(s)}} \tag{2.51}$$

one can rewrite Eq. (2.50) as

$$I(s) = \frac{V_o}{D}\sqrt{\frac{\rho R_o^3}{2\sigma}}\, \tau \tag{2.52}$$

or

$$I(s) = \epsilon\tau \; . \tag{2.53}$$

Recall that the laboratory time scale T across which the forcing function acts is

$$T = \frac{D}{V_o} \; . \tag{2.54}$$

Since the small parameter ϵ is the ratio of bubble time to laboratory time, its value gives the scaling factor between the two times. This scaling allows one the freedom of choosing a different diameter headform and at the same time

maintain a proper scaling through the small parameter, ϵ. Thus the calculated value of the integral equals the parameter $\epsilon\tau$ and is tabulated in Appendix B with the corresponding values of the forcing function. The tabulation of F and $\epsilon\tau$ was then used to interpolate using a piecewise parabolic fit of the forcing function for consecutive triads of points. The curve fit was performed for various cavitation numbers between $K = 0.60$ and $K = 0.70$. This form of the curve fit was used to inspect carefully the region of vaporous growth and collapse for different values of K.

2.2.3.2 Two-Parabola Curve Fit

In an effort to simplify the formulation of the problem, the forcing function was refit with two parabolas instead of a piece-wise parabolic fit. The two-parabola fit incorporated Eqs. (2.48) and (2.49) which defined the axis shift for different cavitation numbers. Figure 12 shows the key parameters and conditions used to fit the two parabolas to the forcing function. The derivation of the first parabola was based on the following conditions:

(1) The parabola has the form

$$F_1 = A_1(\epsilon\tau)^2 + B_1(\epsilon\tau) + C_1 \qquad ,$$

(2) $\quad F_1(\epsilon\tau = 0) = C_1 = 0 \qquad ,$

(3) $\quad F_1\left(\epsilon\tau_m\right) = F_m = A_1\left(\epsilon\tau_m\right)^2 + B_1\left(\epsilon\tau_m\right) + C_1 \quad ,$

(4) $\quad \dfrac{dF_1}{d(\epsilon\tau)}\left(\epsilon\tau_m\right) = 2A_1\left(\epsilon\tau_m\right) + B_1 = 0 \qquad .$
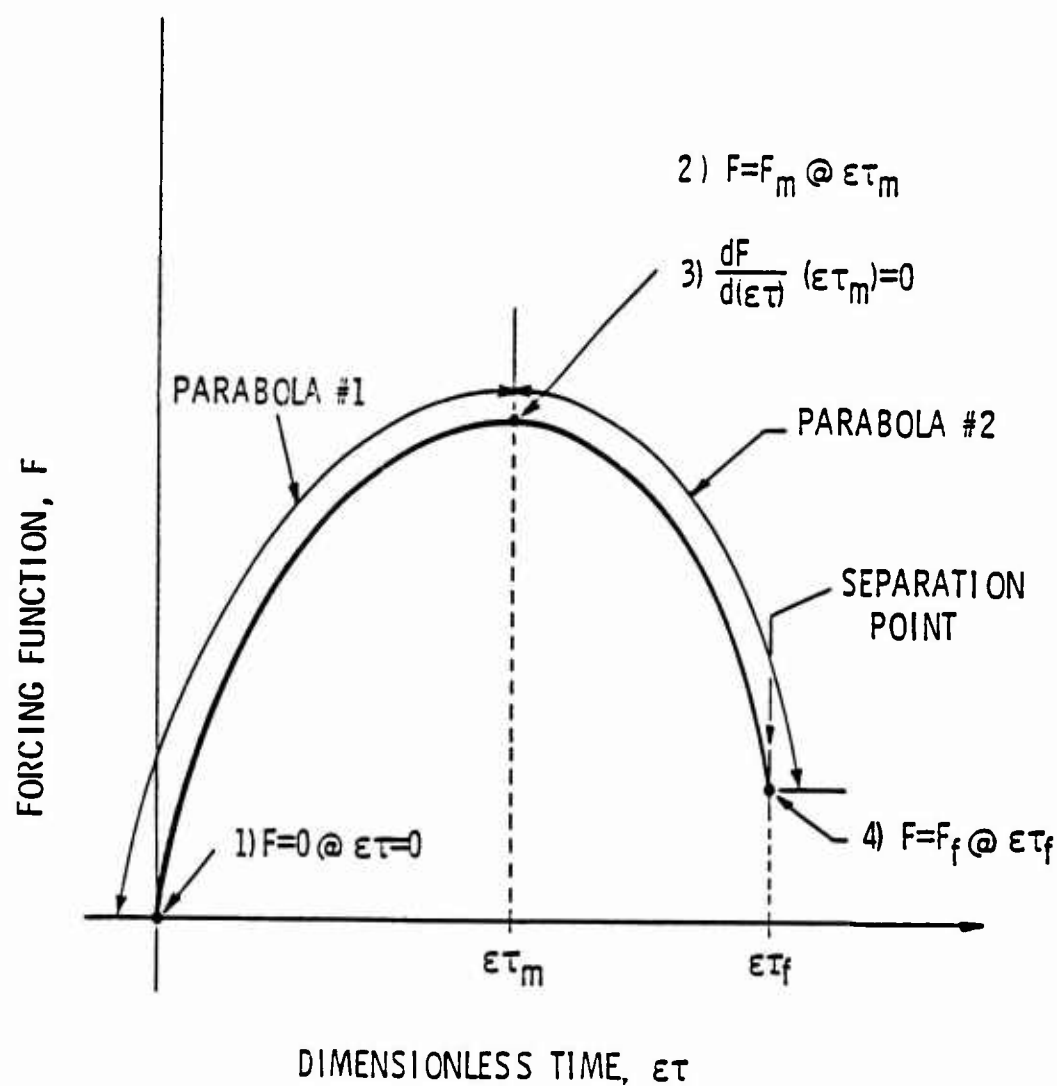
Figure 12. Schematic Plot of the Forcing Function Showing the Key Parameters used for a Two-Parabola Curve Fit.

Conditions (2) and (3) simply define the value of the forcing function at the origin and maximum point while Condition (4) states that the forcing function has zero slope at the maximum point. A simultaneous solution of these equations using Conditions (2), (3) and (4) gives the following expressions for the parabolic coefficients of the first parabola:

$$A_1 = -\frac{F_m}{(\epsilon\tau_m)^2} \quad ,$$

$$B_1 = \frac{2F_m}{\epsilon\tau_m} \quad , \tag{2.54}$$

$$C_1 = 0.0 \quad .$$

The conditions used to approximate the second parabola are:

(1) The parabola has the form

$$F_2 = A_2(\epsilon\tau)^2 + B_2(\epsilon\tau) + C_2 \quad ,$$

(2) $F_2(\epsilon\tau_m) = F_m = A_2(\epsilon\tau_m)^2 + B_2(\epsilon\tau_m) + C_2 \quad ,$

(3) $\dfrac{dF_2}{d(\epsilon\tau)}(\epsilon\tau_m) = 2A_1(\epsilon\tau_m) + B_2 = 0 \quad ,$

(4) $F_2(\epsilon\tau_f) = F_f = A_2(\epsilon\tau_f)^2 + B_2(\epsilon\tau_f) + C_2 \quad .$

Satisfaction of Conditions (2), (3) and (4) for the second parabola gives the parabolic coefficients

$$A_2 = \frac{F_f - F_m}{(\epsilon \tau_f - \epsilon \tau_m)^2} \quad ,$$

$$B_2 = \frac{2(F_m - F_f)(\epsilon \tau_m)}{(\epsilon \tau_f - \epsilon \tau_m)^2} \quad , \tag{2.55}$$

$$C_2 = F_m - \frac{(F_m - F_f)(\epsilon \tau_m)^2}{(\epsilon \tau_f - \epsilon \tau_m)^2} \quad .$$

Figure 13 shows the two-parabola fit plotted against the actual forcing function. To check the validity of the curve fit, a comparison of the total impulsive effect of the forcing function and the two-parabola fit was made. The impulse is written as

$$J_p = \int F(\epsilon \tau) d(\epsilon \tau) \tag{2.56}$$

and was calculated using the integration routine discussed earlier. Figure 14 shows the comparison of the impulses across the range of the vaporous growth region. The over-estimation of the curve fit resulted in a relative error of 3.0391%.
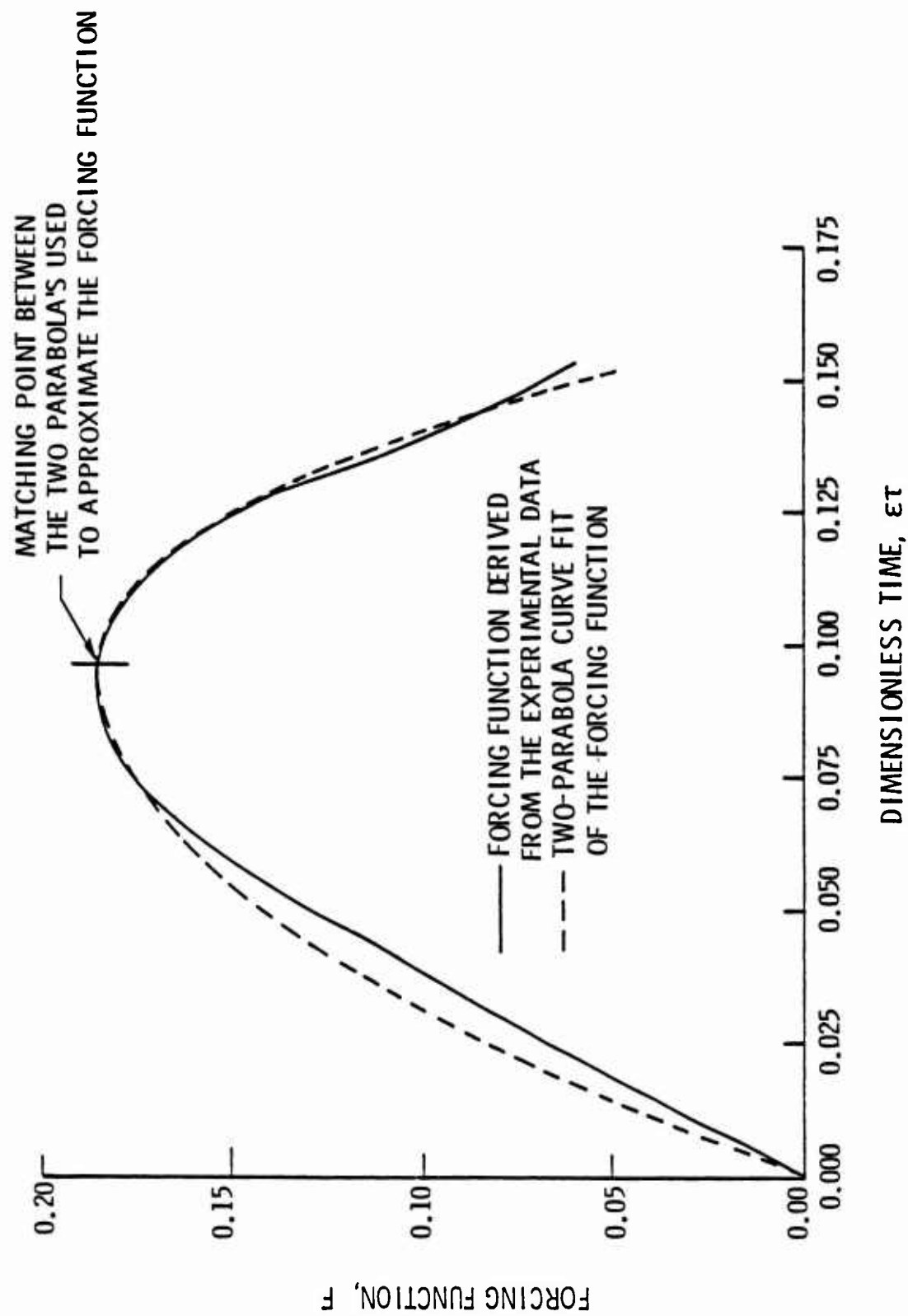
Figure 13. Comparison of the Actual Forcing Function Computed
from the Experimental Data with the Two-Parabola
Curve Fit of the Forcing Function.
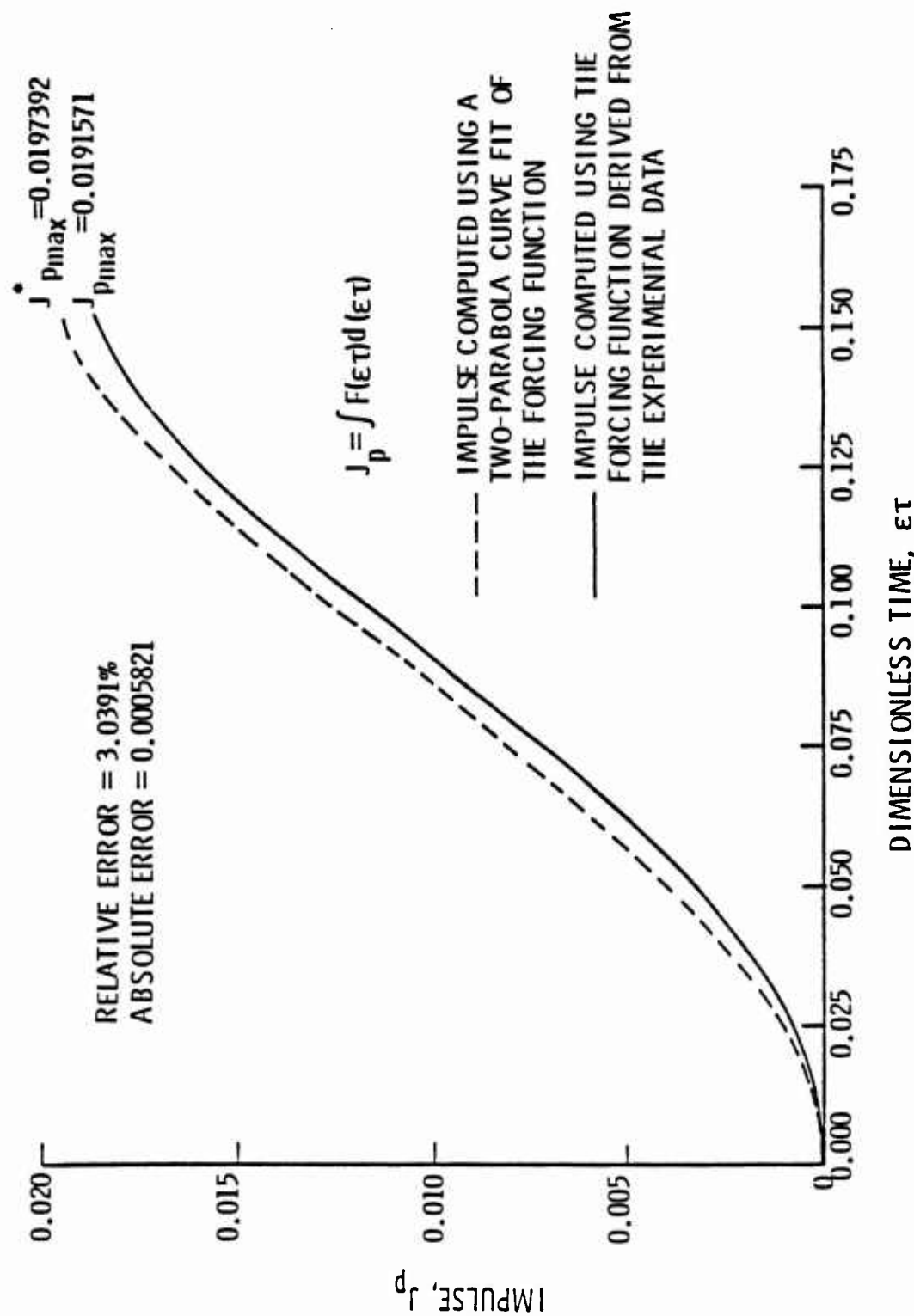
Figure 14. Comparison of the Impulsive Effect of the Actual Forcing Function and Two-Parabola Curve Fit.

2.2.3.3 Trigonometric Curve Fit

An alternative to the piecewise parabolic fit and the two-parabola fit of the forcing function is a curve fit using trigonometric functions to produce a smooth continuous curve fit across the entire range of vaporous growth. This type of curve fit eliminates the need to derive new initial conditions at the junction between the two parabolas discussed in the previous section. One can assume that in the interval

$$0 < t_s < t_f \quad ,$$

that

$$F(\epsilon \tau) = F(t_s) = F_f \mathrm{Sin}(\Omega t_s) \tag{2.57}$$

where $\Omega t_s = \pi/2$ when $t_s = t_f$. Therefore

$$\Omega = \frac{\pi}{2} \frac{1}{t_f}$$

and

$$F(\epsilon \tau) = F(t_s) = F_f \mathrm{Sin}\left(\frac{\pi}{2} \frac{t_s}{t_f}\right) \quad . \tag{2.58}$$

If we consider the forcing function to be the cause of all primary resonances in the system as discussed by Nayfeh and Mook [16], one writes the forcing function as

$$F_f \mathrm{Sin}\Omega t_s = \epsilon K \mathrm{Sin}\left(\omega_o T_o + \sigma T_1\right) \quad . \tag{2.59}$$

Thus, the primary effect will be in the ε^1 equation and we maintain an autonomous system in the ε^0 equation. That is to say the system is soft, not stiff. This result is consistent with the outcome of the parabolic forcing functions as can be seen by the inspection of those results.

2.3 Formulation of the Initial Conditions

2.3.1 Derivation of the Initial Radius, r(0)

In an effort to solve the governing ordinary differential equation in the vaporous growth region, the initial conditions at the beginning of this region must be derived. The initial point was defined earlier as that point on the body where $C_p = -K$. Also, the initial point is designated by the dimensionless time $\tau = 0$. The conditions for the radius and rate of growth of the radius are derived as functions of τ at $\tau = 0$ and as functions of K across the range $K = 0.60 \rightarrow K = 0.70$. Thus, an arbitrary choice of the cavitation number would produce a corresponding set of initial conditions for $r(0)$ and $\dot{r}(0)$.

Since the initial conditions are functions of the parameter τ, a correlation is made between τ and s because the initial formulation of r and $\dot{r}$ was made against s. It was shown earlier that by choosing different values of the cavitation number the axis of the forcing function shifted because of the translation of the initial point of the vaporous growth region. To find the arc length positions corresponding to the initial point of the vaporous growth region, one must use the parabolic form of the pressure coefficient.

$$C_p(s) = As^2 + Bs + C$$

along with the condition that the initial conditions are derived at the point $C_p = -K$ from the flaccid bubble equations. The resulting equation is

$$As^2 + Bs + C + K = 0 \tag{2.60}$$

which can be solved with the quadratic formula to give

$$s(K) = \frac{B}{2A}\left[-1 \pm \sqrt{1 - \frac{4A(C+K)}{B^2}}\right] \tag{2.61}$$

where

$$\frac{4A(C+K)}{B^2} < 1 \quad . \tag{2.62}$$

Equation (2.61) is used to compute the arc length positions at the beginning of the vaporous growth region which define the range across which the equations for r and $\dot{r}$ are valid. Using the computed values of r and $\dot{r}$ at the beginning of the vaporous growth region gives the initial conditions for the problem at various values of K.

The initial condition for r is equivalent to Eq. (2.30) which was derived at the point $C_p = -K$. Use of a binomial expansion transforms (2.30) into the form

$$r(0) = 1 + \frac{KWe}{8} + 0\left[(KWe)^2\right] \quad . \tag{2.63}$$

Figure 6 shows the region of interest where the initial conditions are sought. Figure 15 is a blow-up of that region with the line representing the initial conditions drawn through the various r curves at different values of K. Equation (2.63) is linear which is exactly the line of the initial condition represented in Figure 15. Thus, Figure 16 represents the initial condition r(0) for various values of the cavitation number. In the formulation of the problem, a general initial condition of

$$r(0) = 1 + q \tag{2.64}$$

is used where q, from Eq. (2.63), is written as

$$q = \frac{KWe}{8} \; .$$

Equation (2.64) is a more precise form to use while exposing the difference in the initial condition used by Parkin [11] which stated

$$r(0) = 1 \; .$$

2.3.2 Derivation of the Initial Growth Rate, $\dot{r}(0)$

In the case of the initial condition for $\dot{r}$, the following conditions were substituted into (2.41) to get an expression for the initial rate of growth:

$$C_p = -K$$

$$r(0) = \sqrt{1 + \frac{KWe}{4}} \tag{2.65}$$

$$s(K) = \frac{B}{2A} \left[-1 \pm \sqrt{1 - \frac{4A(C + K)}{B^2}} \right] \; .$$
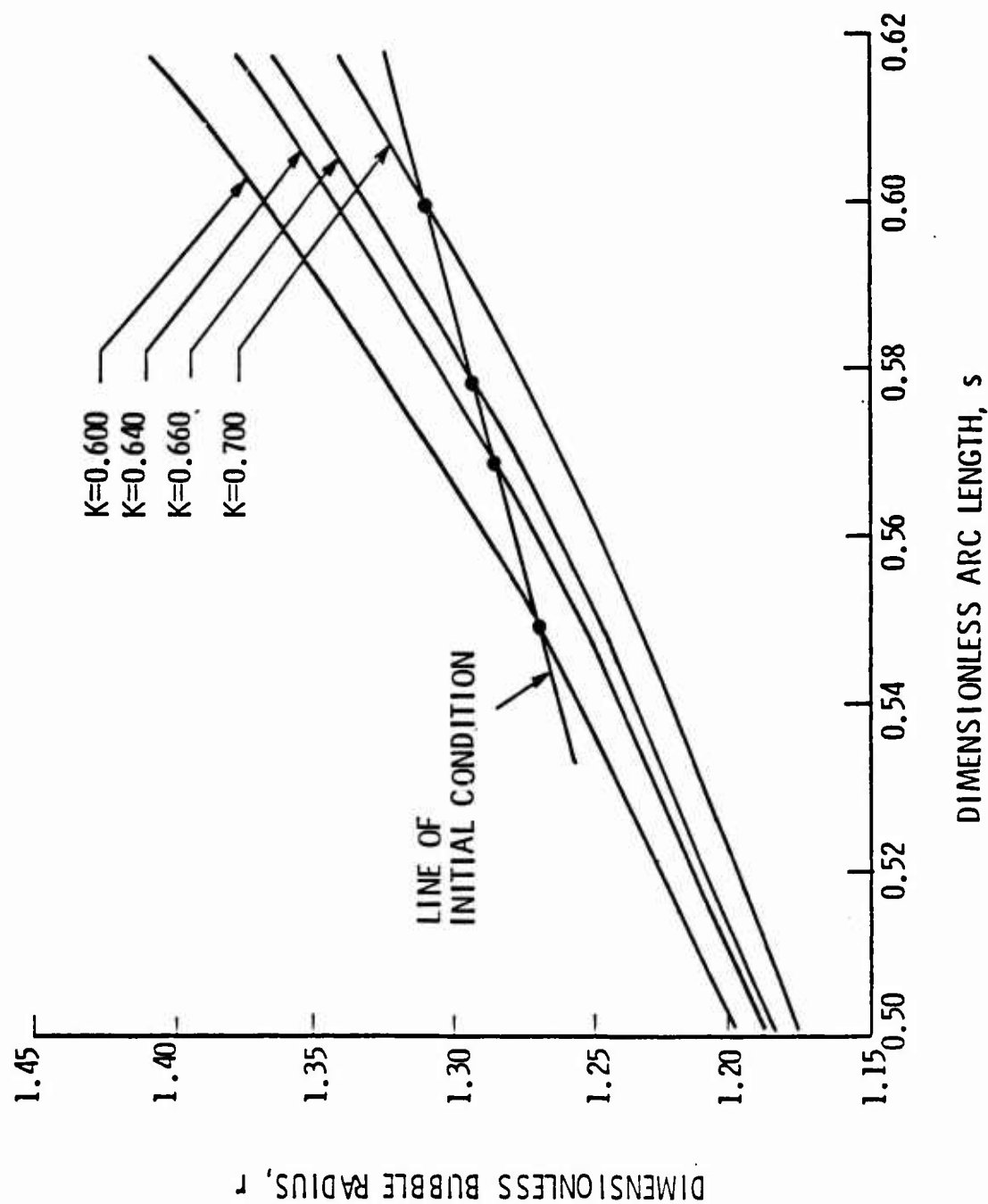
Figure 15. Plot of the Dimensionless Bubble Radius with the Line of Initial Condition for K = 0.60 → K = 0.70.
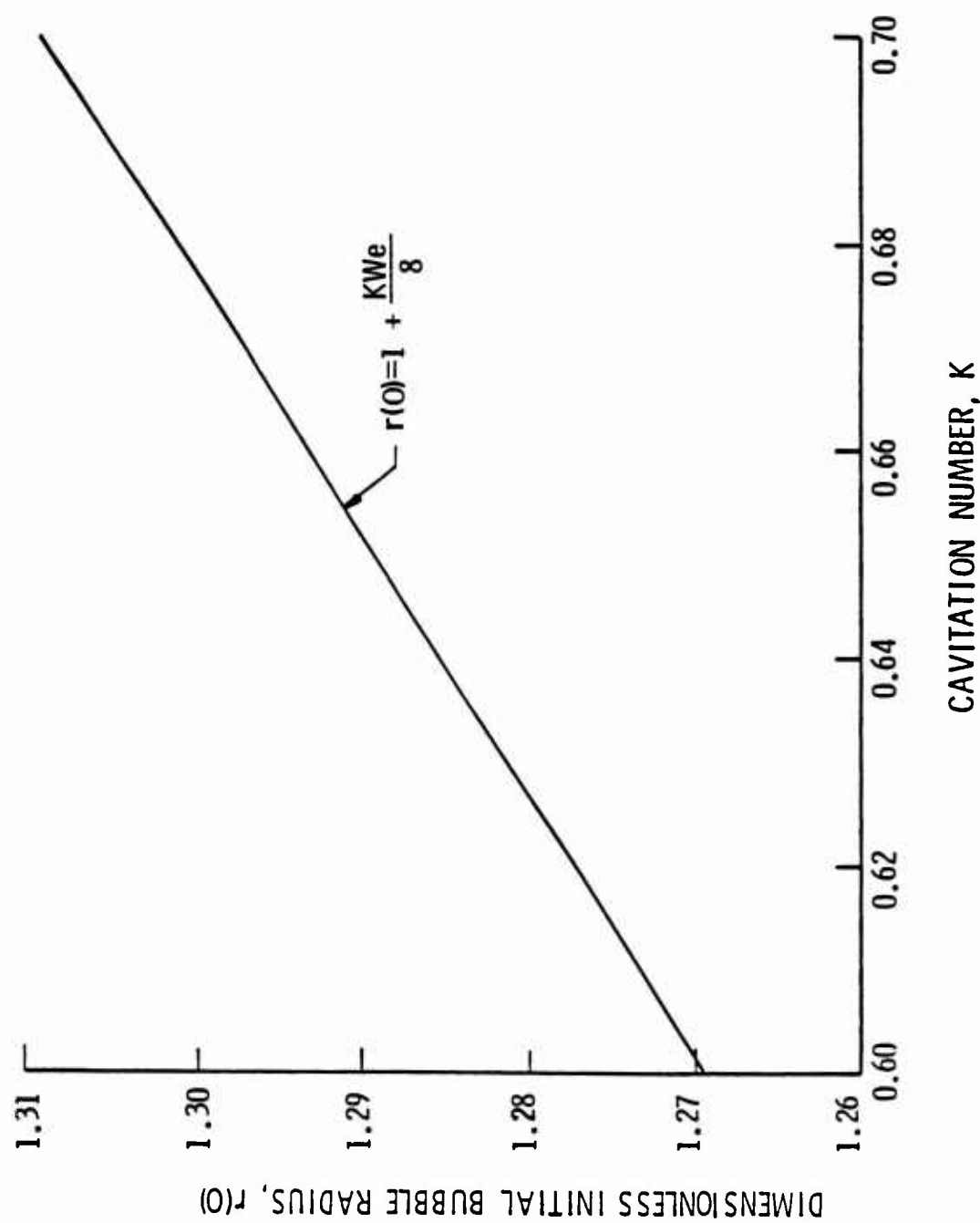
Figure 16. Plot of the Line of Initial Condition versus the Cavitation Number for K = 0.60 → K = 0.70.

The resulting equation is written as

$$\dot{r}(0) = \frac{1}{8}\left(1 + \frac{KWe}{4}\right)We^{3/2}\frac{R_o}{D}\sqrt{B^2 - 4A(C + K)} \qquad (2.66)$$

and is a function of the cavitation number and the physical parameters of the flow and headform. Figure 17 shows the line of initial condition for $\dot{r}(0)$ across the range of cavitation numbers being investigated. In bubble time the initial condition has a constant value with a magnitude of the order 1×10^{-5}. In laboratory time this translates to a velocity with a magnitude of the order 1×10^{-9} fps. Since the magitude is relatively small, the initial condition for $\dot{r}(0)$ is approximated as zero, although the fact that it is not actually zero is found to be conceptually important later. The zero value for $\dot{r}(0)$ corresponds to the initial condition used by Parkin [11].

In summary, using the properties of a flaccid bubble undergoing isothermal expansion, expressions were derived for the radius of growth and the rate of growth of the radius. These expressions are functions of the cavitation number, the particular parabolic coefficients used to approximate the experimental data and the physical parameters of the flow and the headform. These expressions are valid in the flaccid bubble region only, beginning at the stagnation point and ending where the pressure coefficient equals the negative of the cavitation number, i.e., $C_p = -K$. These values of r and $\dot{r}$ at the point $C_p = -K$ represent the
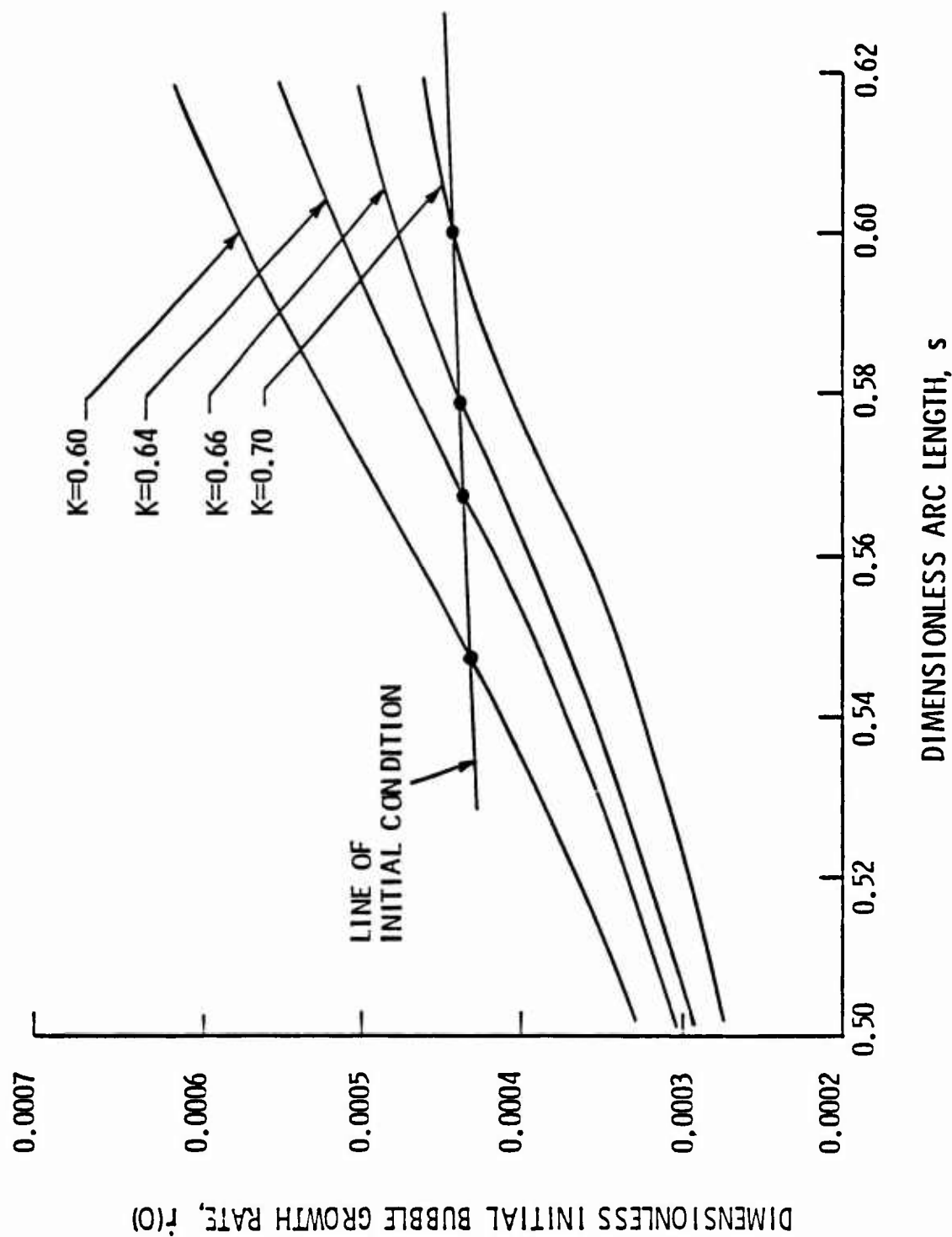
Figure 17. Plot of the Dimensionless Bubble Rate of Growth
with the Line of Initial Condition for
K = 0.60 → K = 0.70.

initial conditions used to solve the governing differential

equation. The resulting initial conditions are

$$r(0) = 1 + Q \quad , \quad Q < 1 \qquad \text{[from Eq. (2.64)]}$$

and (2.67)

$$\dot{r}(0) = 0 \qquad \text{[evaluation of Eq. (2.66)]}$$

for the range of cavitation numbers under investigation.

2.4 The Differential Equation for an Isothermal Bubble

Written in dimensionless form, the governing equation for

vaporous growth and collapse of a spherical isothermal cavitation

bubble is

$$r \frac{d^2 r}{d\tau^2} + \frac{3}{2} \left(\frac{dr}{d\tau}\right)^2 = \frac{\gamma}{r^3} - \frac{1}{r} + F(\epsilon\tau) \quad . \tag{2.68}$$

Equation (2.68) is a second order nonlinear ordinary differential

equation requiring two initial conditions for its complete

solution. The initial conditions for $r(0)$ and $\dot{r}(0)$ were derived

in the previous section, Eqs. (2.63) and (2.66). The forcing

function, $F(\epsilon\tau)$, which causes the bubble to grow from the initial

condition at $r(0)$, to some maximum radius r_m, was approximated by

two parabolas making Eq. (2.68) nonautonomous. Past studies of

the nonautonomous form of Eq. (2.68) have been performed using

appropriate numerical methods. In several unpublished numerical

studies by Parkin, it was found possible to distinguish four

classes of solution for Eq. (2.68). A Class 1 solution is

characterized by small-scale oscillations that make up the major

part of the bubble's motion. In a Class 2 solution, the bubble motion involves a periodic motion similar to a Class 1 solution but with a larger amplitude. A Class 3 solution has periodic solutions for the bubble's oscillations but with larger amplitudes. The size of the amplitudes was found to be dependent on the key parameters of the flow. Finally, a Class 4 solution represented a bubble growing infinitely large. Of interest here are the Class 1, Class 2 and Class 3 solutions. It is desired that a solution of Eq. (2.68) be obtained that would allow a parametric study of these different classes of solution to be performed. With the initial conditions and forcing function previously derived, one can now apply the method of multiple scales in an attempt to get an approximate analytic solution of the isothermal Rayleigh-Plesset equation.

CHAPTER 3

PARTIAL SOLUTION OF THE DYNAMICAL PROBLEM

3.1 The Method of Multiple Scales

Having established the governing differential equation and
initial conditions for isothermal cavitation bubble growth and
collapse, the method of multiple scales is used to find an
approximate analytical solution to the problem. The method of
multiple scales is used because of the two dissimilar time scales
that exist in this problem. Since there are two different time
scales, a variation of the method of multiple scales called the
two-variable expansion method is used. Application of the two-
variable expansion method begins with the expansion of the two
time scales.

3.1.1 The Time Scales

As discussed earlier, there are two time scales that
characterize this problem. The time measured in the laboratory is
the slow time scale t_s and is the characteristic time scale of the
forcing function. The fast time scale t_f is a very short time
compared to the slow time scale and is the characteristic time
scale of the individual bubble oscillations. Expansion of the
time scales based on the small parameter ε, defined by Eq. (1.2),
is derived by Cole and Kevorkian [14]. The slow time scale is
simply

$$t_s = \varepsilon\tau \tag{3.1}$$

while the fast time scale is written as

$$t_f = (1 + \epsilon^2 \omega_2 + \epsilon^3 \omega_3 + \ldots)\tau \quad . \tag{3.2}$$

Because the individual bubble oscillations are very fast, the expansion for t_f includes additional terms which allow for different frequencies of oscillation that may occur as the bubble passes through a varying pressure field. Based on these two time scales, the dynamical equation can be expanded to the order ϵ^3.

3.1.2 Formulation of the Dynamical Equations to Order ϵ^3

Formulation of the dynamical equations to order ϵ^3 is accomplished by using the expansions for the slow and fast time scales, Eqs. (3.1) and (3.2), to derive the first and second derivative expansions as functions of the dimensionless bubble time τ. One can write

$$\tau = f(t_s, t_f) \tag{3.3}$$

where the derivative with respect to Eq. (3.3) is

$$\frac{d}{d\tau} = (1 + \epsilon^2 \omega_2 + \epsilon^3 \omega_3) \frac{\partial}{\partial t_f} + \epsilon \frac{\partial}{\partial t_s} \quad . \tag{3.4}$$

It follows from Eq. (3.4) that the second derivative is

$$\frac{d^2}{d\tau^2} = (1 + \epsilon^2 \omega_2 + \epsilon^3 \omega_3)^2 \frac{\partial^2}{\partial t_f^2} + 2(\epsilon + \epsilon^3 \omega_2 + \epsilon^4 \omega_3) \frac{\partial^2}{\partial t_f \partial t_s}$$

$$+ \epsilon^2 \frac{\partial^2}{\partial t_s^2} \tag{3.5}$$

or written in ascending power of ϵ the second derivative expansion is

$$\frac{d^2}{d\tau^2} = \frac{\partial^2}{\partial t_f^2} + 2\varepsilon \frac{\partial^2}{\partial t_f \partial t_s} + \varepsilon^2 \left[2\omega_2 \frac{\partial^2}{\partial t_f^2} + \frac{\partial^2}{\partial t_s^2} \right]$$

$$+ \varepsilon^3 \left[2\omega_3 \frac{\partial^2}{\partial t_f^2} + 2\omega_2 \frac{\partial^2}{\partial t_f \partial t_s} \right] \quad . \tag{3.6}$$

Using the first and second derivative expansions, one can write Eq. (2.68) in a completely expanded form up to ε^3 using a general perturbation expansion for r having the form

$$r = r_0 + \varepsilon r_1 + \varepsilon^2 r_2 + \varepsilon^3 r_3 + \dots \quad . \tag{3.7}$$

Use of Eq. (3.7) in (3.6) and (3.4) leads to

$$\frac{dr}{d\tau} = \frac{\partial r_0}{\partial t_f} + \varepsilon \left[\frac{\partial r_1}{\partial t_f} + \frac{\partial r_0}{\partial t_s} \right] + \varepsilon^2 \left[\frac{\partial r_2}{\partial t_f} + \frac{\partial r_1}{\partial t_s} + \omega_2 \frac{\partial r_0}{\partial t_f} \right]$$

$$+ \varepsilon^3 \left[\frac{\partial r_3}{\partial t_f} + \frac{\partial r_2}{\partial t_s} + \omega_2 \frac{\partial r_1}{\partial t_f} + \omega_3 \frac{\partial r_0}{\partial t_f} \right] \tag{3.8}$$

and

$$\frac{d^2 r}{d\tau^2} = \frac{\partial^2 r_0}{\partial t_f^2} + \varepsilon \left[\frac{\partial^2 r_1}{\partial t_f^2} + 2 \frac{\partial^2 r_0}{\partial t_f \partial t_s} \right] + \varepsilon^2 \left[\frac{\partial^2 r_2}{\partial t_f^2} + 2 \frac{\partial^2 r_1}{\partial t_f \partial t_s} + 2\omega_2 \frac{\partial^2 r_0}{\partial t_f^2} + \frac{\partial^2 r_0}{\partial t_s^2} \right]$$

$$+ \varepsilon^3 \left[\frac{\partial^2 r_3}{\partial t_f^2} + 2 \frac{\partial^2 r_2}{\partial t_f \partial t_s} + 2\omega_2 \frac{\partial^2 r_1}{\partial t_f^2} + \frac{\partial^2 r_1}{\partial t_s^2} + 2\omega_3 \frac{\partial^2 r_0}{\partial t_f^2} + 2\omega_2 \frac{\partial^2 r_0}{\partial t_f \partial t_s} \right] \quad .$$

$$\tag{3.9}$$

If one assumes the bubbles under consideration are spherical, then the term $S(r,n)$ from Eq. (2.68) is set equal to unity. The term $F(\varepsilon\tau)$ from Eq. (2.68) has the form of a parabola as discussed in Section (2.2). Unfortunately, use of a parabola of the form

$$F = A\varepsilon^2 t_s^2 + B\varepsilon t_s + C \tag{3.10}$$

requires the solution of nonautonomous first and second order expansion equations to get a complete solution. By using a trigonometric form of the forcing function represented by Eq. (2.59), one needs to solve only the nonautonomous first order expansion equations since the trigonometric form is expressed only to the first order of the small parameter, ε.

Calculation of each term in Eq. (2.68) based on the general perturbation expansion for r and the first and second time derivative expansions, permits one to write the isothermal Rayleigh-Plesset equation in ascending powers of the small parameter ε as a function of the fast and slow time variables. The same procedure can be performed on the initial conditions. Introduction of a normalized radius u where

$$u = \frac{r}{1 + Q} \tag{3.11}$$

allows one to write the normalized isothermal Rayleigh-Plesset equation with initial conditions consistent with those used by Parkin [11]. The resulting set of differential equations and initial correlations up to ε^3 can be solved and substituted back into Eq. (3.7) using (3.11) to get the final solution for the dimensionless bubble radius as a function of time.

The normalized equations and initial conditions written in ascending powers of ϵ are:

Order ϵ^0

$$u_0 \frac{d^2 u_0}{dt_f^2} + \frac{3}{2}\left(\frac{du_0}{dt_f}\right)^2 = \frac{\gamma}{u_0^3}\frac{1}{(1+Q)^5} - \frac{1}{u_0(1+Q)^3} + \frac{F_C}{1+Q} \quad (3.11a)$$

$$u_0(0) = 1.0$$

$$\frac{du_0}{dt_f}(0) = 0.0 \qquad \text{Initial Conditions} \qquad (3.11b)$$

Order ϵ^1

$$\frac{d^2 u_1}{dt_f^2} + \left[\frac{3}{u_0}\frac{du_0}{dt_f}\right]\frac{du_1}{dt_f} + \left[\frac{4}{u_0}\frac{d^2 u_0}{dt_f^2} + \frac{9}{2}\frac{1}{u_0^2}\left(\frac{du_0}{dt}\right)^2 + \frac{2}{(1+Q)^3 u_0^3}\right] u_1$$

$$= \frac{F_B}{(1+Q)^2 u_0} t$$

$$u_1(0) = 0.0$$

$$\frac{du_1}{dt_f}(0) = 0.0 \qquad \text{Initial Conditions} \qquad (3.12b)$$

Order ϵ^2

$$u_0 \frac{d^2 u_2}{dt_f^2} + 4u_2 \frac{d^2 u_0}{dt_f^2} + 3 \frac{du_0}{dt_f} \frac{\partial u_2}{dt_f} + \frac{9}{2} \frac{u_2}{u_0} \left(\frac{du_0}{dt_f}\right)^2 + \frac{2u_2}{u_0^2(1+Q)^3}$$

$$- \frac{3F_C}{(1+Q)^2} \frac{u_2}{u_0} = \frac{F_A t_f^2}{(1+Q)^2} + \frac{3F_B}{(1+Q)^2} \frac{u_1^2}{u_0^2} - \frac{u_1^2}{u_0^3} \frac{1}{(1+Q)^3}$$

$$- 2\omega_2 u_0 \frac{d^2 u_0}{dt_f^2} - 4u_1 \frac{d^2 u_1}{dt_f^2} - \frac{6}{(1+Q)} \frac{u_1}{u_0} \frac{\partial^2 u_0}{dt_f^2}$$

$$- 3\omega_2 \left(\frac{du_0}{dt_f}\right)^2 - \frac{3}{2} \left(\frac{du_1}{dt_f}\right)^2 - 9 \frac{u_1}{u_0} \frac{du_0}{dt_f} \frac{du_1}{dt_f} - \frac{9}{2} \frac{u_1^2}{u_0^2} \left(\frac{du_0}{dt_f}\right)^2$$

$$(3.13a)$$

$$u_2(0) = 0.0$$

$$\frac{du_2(0)}{dt_f} = -\omega_2 \frac{du_0(0)}{dt_f} \qquad \text{Initial Conditions} \qquad (3.13b)$$

Order ϵ^3

$$u_0 \frac{d^2 u_3}{dt_f^2} + 4u_3 \frac{d^2 u_0}{dt_f^2} + 3 \frac{du_0}{dt_f} \frac{du_3}{dt_f} + \frac{9}{2} (1+Q)u_3 \left(\frac{du_0}{dt_f}\right)^2$$

$$+ \frac{2}{(1+Q)^3} \frac{u_3}{u_0^2} - \frac{3F_C}{(1+Q)^2} \frac{u_3}{u_0} = \frac{3F_A}{(1+Q)^2} \frac{u_1}{u_0} t_f^2$$

$$+ \frac{3F_B}{(1+Q)^2} t_f + \frac{6F_C}{(1+Q)^2} \frac{u_1}{u_0^2} + \frac{F_C}{(1+Q)^2} \frac{u_1^3}{u_0^3}$$

$$- \frac{2}{(1 + Q)^3} \frac{u_1 u_2}{u_0^3} - 6\omega_2 \frac{du_0}{dt_f} \frac{du_1}{dt_f} - 3\omega_3 \left(\frac{du_0}{dt_f}\right)^2$$

$$- 3 \frac{du_1}{dt_f} \frac{du_2}{dt_f} - 9 \frac{u_1}{u_0} \frac{du_0}{dt_f} \frac{du_2}{t_f} - 9\omega_2 \left(\frac{u_1}{u_0}\right)\left(\frac{du_0}{dt_f}\right)^2$$

$$- \frac{9}{2} \frac{u_1}{u_0} \left(\frac{du_1}{dt_f}\right)^2 - 3 \frac{u_2}{u_0} \frac{du_0}{dt_f} \frac{du_1}{dt_f} - 9 \frac{u_1^2}{u_0^2} \frac{du_0}{dt_f} \frac{du_1}{dt_f}$$

$$- 9\omega_2 \left(\frac{u_1}{u_0}\right)\left(\frac{du_0}{dt_f}\right)^2 - \frac{9}{2} \frac{u_1}{u_0} \left(\frac{du_1}{dt_f}\right)^2 - 3 \frac{u_2}{u_0} \frac{du_0}{dt_f} \frac{du_1}{dt_f}$$

$$- 9 \frac{u_1^2}{u_0^2} \frac{du_0}{dt_f} \frac{du_1}{dt_f} - 9 \frac{u_1 u_2}{u_0^2} \left(\frac{du_0}{dt_f}\right)^2 - \frac{3}{2} \frac{u_1^3}{u_0^3} \left(\frac{du_0}{dt_f}\right)^2$$

$$- 2\omega_2 u_0 \frac{d^2 u_1}{dt_f^2} - 2\omega_3 u_0 \frac{d^2 u_0}{dt_f^2} - 4u_1 \frac{d^2 u_2}{dt_f^2} - 8\omega_2 u_1 \frac{d^2 u_1}{dt_f^2}$$

$$- 4u_2 \frac{d^2 u_1}{dt_f^2} - 6 \frac{u_1^2}{u_0} \frac{\partial^2 u_1}{dt_f^2} - 12 \frac{u_1 u_2}{u_0} \frac{d^2 u_0}{dt_f^2} - 4 \frac{u_1^3}{u_0^2} \frac{d^2 u_0}{dt_f^2}$$

$$(3.14a)$$

$$u_3(0) = 0.0$$

$$\frac{du_3(0)}{dt_f} = - \omega_2 \frac{du_1(0)}{dt_f} - \omega_3 \frac{du_0(0)}{dt_f}$$

Initial Conditions

$$(3.14b)$$

3.2 Solution of the Multiple Scale Equations

3.2.1 The ϵ^0 Solution

The first step in obtaining the complete solution of the
isothermal Rayleigh-Plesset equation is to solve the normalized
zeroth order differential equation that results from the
application of the method of multiple scales. The zeroth order
equation, Eq. (3.11a), is still nonlinear but is now autonomous
because the time dependent forcing function has been reduced to
a constant. Equation (3.11a) is analogous to the autonomous
form of the Rayleigh-Plesset equation studied by Parkin [11]
where the term F_C corresponds to his piecewise autonomous step
function representation of the forcing function. From Eq. (3.11a)
one can examine the intricacies of this problem by investigating
the energy curves and phase plane trajectories. This form of
analysis is restricted to the autonomous zeroth order differential
equation and is very useful in determining the limits of the
periodic and non-periodic solutions which are based on the
location and character of the singularities that exist in the
autonomous system.

3.2.1.1 The Potential Energy Function

The zeroth order equation and initial conditions may be written
as

$$u_0 \frac{d^2 u_0}{dt_f^2} + \frac{3}{2} \left(\frac{du_0}{dt_f}\right)^2 = \frac{\gamma}{u_0^3} \frac{1}{(1 + Q)^5} - \frac{1}{u_0} \frac{1}{(1 + Q)^3} + \frac{F_C}{(1 + Q)^2}$$

$$u_0(0) = 1.0$$

$$\frac{du_0}{dt_f}(0) = 0.0 \quad .$$

It is of great interest to consider the different solutions of the zeroth order equation for the two cases when (1) $F_C = 0$ and (2) $F_C \neq 0$. One can replace the second order differential equation by a pair of coupled first order equations using the relation

$$v = \frac{du_0}{dt} \quad .$$

To simplify the expressions by dropping the subscript zero, the zeroth order equation and initial conditions can be rewritten as

$$u \frac{dv}{dt_f} + \frac{3}{2}v^2 = \frac{\gamma}{u^3}\frac{1}{(1+Q)^5} - \frac{1}{u}\frac{1}{(1+Q)^3} + \frac{F_C}{(1+Q)^2} \qquad (3.15)$$

$$u(0) = 0$$

$$v(0) = 1 \quad .$$

Using the transformation

$$u \frac{dv}{dt} + \frac{3}{2}v^2 = \frac{1}{2u^2}\frac{d}{du}\left(u^3 v^2\right) \qquad (3.16)$$

one may express Eq. (3.15) in integral form as

$$u^3 v^2 = \int \left[\frac{2\gamma}{u}\frac{1}{(1+Q)^5} - \frac{2u}{(1+0)^3} + \frac{2u^2 F_C}{(1+Q)^2}\right]du \quad . \qquad (3.17)$$

The left-hand side of Eq. (3.17) is proportional to the kinetic energy of the bubble motion while the right-hand side corresponds to the negative potential energy, $-V$, of the bubble. Evaluating the integral in Eq. (3.17) as an indefinite integral, one can write

$$- V = \frac{2\gamma \ell n u}{(1 + Q)^5} - \frac{u^2}{(1 + Q)^3} + \frac{2}{3} u^3 \frac{F_C}{(1 + Q)^2} + k \qquad (3.18)$$

where k is a constant of integration that permits one to adjust the level of V for different initial conditions. Setting $F_C = 0$ and evaluating Eq. (3.18) at the initial conditions defined for the zeroth order equation, one writes the potential energy function V

$$V = - \frac{2\gamma}{(1 + Q)^5} \ell n u + \frac{1}{(1 + Q)^3} \left(u^2 - 1\right) \qquad (3.19)$$

and the plot of Eq. (3.19) versus the normalized radius u is shown in Fig. 18 for values of $Q = 0.30$ to $Q = 0.0$. It is easy to see from Fig. 18 that as the value of Q decreases toward zero, the point of minimum potential energy shifts to the right. The relationship defining the location of this minimum energy is derived by setting the first derivative equal to zero. Thus,

$$\frac{dV}{du} = - \frac{2\gamma}{(1 + Q)^2} \frac{1}{u} + \frac{2u}{(1 + Q)^3} = 0$$

or

$$u = \pm \frac{\sqrt{\gamma}}{1 + Q} \qquad (3.20)$$
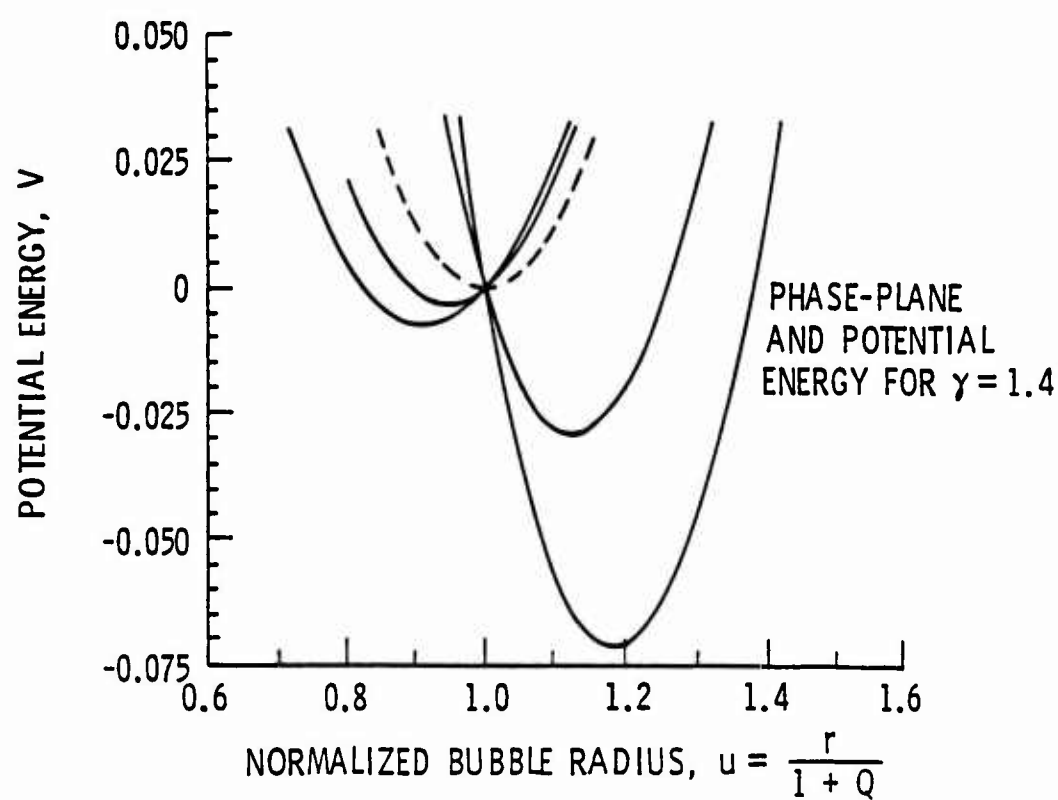
Figure 18. Potential Energy Plot for $F_c = 0$ and $Q = 0.3 \rightarrow 0.0$.

which defines analytically the location of minimum energy. In this study we restrict our attention to positive values of u and thus neglect the negative root. The importance of Eq. (3.20) will become evident later when we study the location and character of the singular points of Eq. (3.15). Moreover, the translation experienced by the minimum energy point is the critical condition that allows one to distinguish between two kinds of motion characteristic to the autonomous system.

If one evaluates Eq. (3.18) using the initial conditions from Eq. (3.15) and sets $F_C \neq 0$, the resulting potential energy function is written as

$$V = - \frac{2\gamma}{(1 + Q)^5} \, \ell nu + \frac{1}{(1 + Q)^3} (u^2 - 1) - \frac{2}{3} \frac{F_C}{(1 + Q)^2} (u^3 - 1) \ .$$

(3.21)

Equation (3.21) represents the potential energy function for the autonomous system having a non-zero forcing function and is plotted in Fig. 19. Clearly, the contribution to the potential energy function of the last term in Eq. (3.21) becomes overwhelming as u increases, causing the energy curve to turn downwards. As before, the location of the minimum and maximum points is determined by setting the first derivative equal to zero. Performing the same operation on Eq. (3.21), we find the result to be a cubic equation of the form

$$u^3 - \frac{1}{F_C(1 + Q)} u^2 + \frac{\gamma}{F_C(1 + Q)^3} = 0 \ .$$

(3.22)
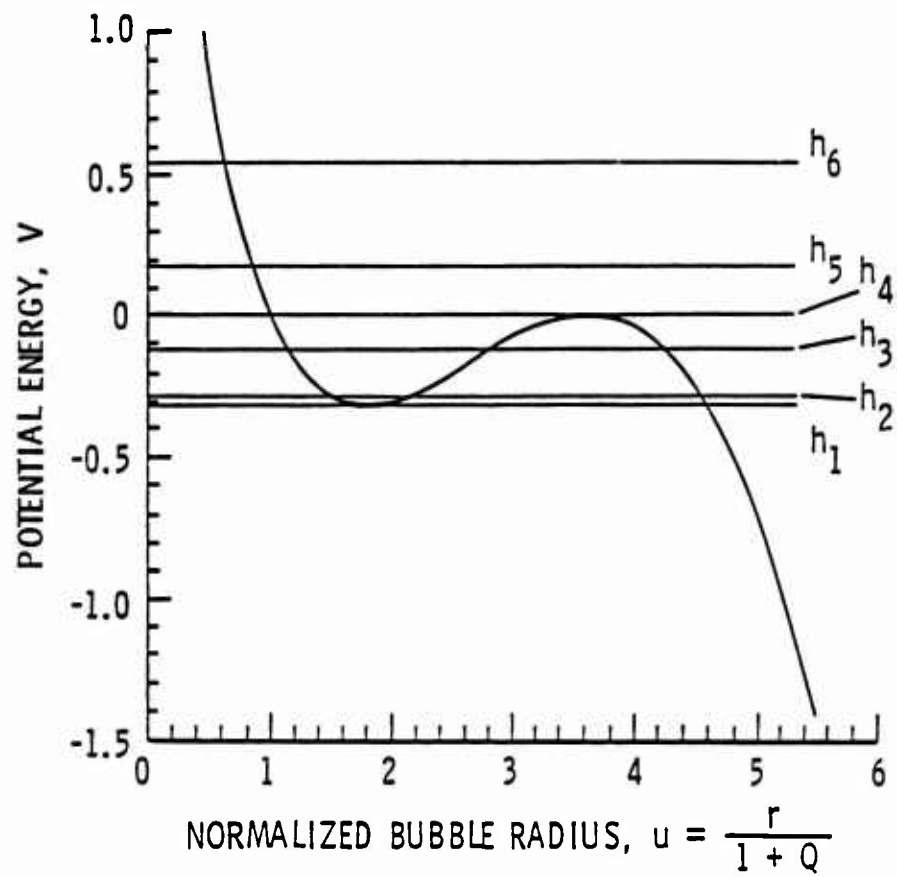
Figure 19.   Potential Energy Plot for $F_c \neq 0$.

The roots of Eq. (3.22) are found using Tartaglia's Method. For the case of three real and unequal roots, the roots of Eq. (3.22) are of the form

$$u_1 = x_1 - \frac{p}{3} \tag{3.23a}$$

where

$$x_i = m \cos\left(\theta_1 + \frac{2\pi(i-1)}{3}\right) \qquad i = 1,2,3$$

and

$$
\left.
\begin{aligned}
\theta_1 &= \frac{1}{3} \cos^{-1}\left(\frac{3b}{am}\right) \\[2mm]
m &= 2\sqrt{\frac{-a}{3}} \\[2mm]
a &= \frac{1}{3}(3q - p^2) \\[2mm]
b &= \frac{1}{27}(2p^3 - 9pq + 27r)
\end{aligned}
\right\} . \tag{3.23b}
$$

The parameters p, q and r are the coefficients of a cubic equation having the form

$$u^3 + pu^2 + qu + r = 0 \quad . \tag{3.24a}$$

Therefore,

$$p = -\frac{1}{F_c(1 + Q)} \quad ,$$

$$q = 0 \qquad \qquad ,$$

and

$$r = \frac{1}{F_C(1 + Q)^3} \quad .$$

(3.24b)

Thus, in terms of the original parameters of the cubic coefficients, the roots of Eq. (3.22) are

$$u_i = \frac{1}{3F_C(1 + Q)} + \frac{2}{3F_C(1 + Q)} \cos\left(\theta_1 + \frac{2\pi(i - 1)}{3}\right) \qquad i = 1,2,3$$

(3.25a)

where

$$\theta_1 = \frac{1}{3} \cos^{-1}\left[1 - \frac{27F_C^2\gamma}{2}\right] \quad .$$

Evaluating the roots for $Q = 0.3$, $\gamma = 1.4$, $F_C = 0.2$, one gets

$$i = 1 \quad , \quad u_1 = 3.600356643$$

$$i = 2 \quad , \quad u_2 = -0.825817193 \qquad (3.25b)$$

$$i = 3 \quad , \quad u_3 = 1.071614395 \quad .$$

Since we are interested in positive roots only, the second is neglected leaving the first and third root to define the location of the maximum and minimum points in Fig. 19.

3.2.1.2 Singular Points and the Phase Plane

Having derived an expression for the potential energy of the autonomous system, we can now look at the phase plane in conjunction with the potential energy to study the singularities that exist in the system. To begin the analysis we need to apply Eq. (3.16) to

(3.15) and use a generalized initial condition for the initial radius that states $u(0) = u_0$. The initial condition of the bubble wall velocity will remain zero because its actual initial value is so small that all analyses whether global or specific will be accurately represented by $\dot{u}(0) = 0$. Use of the generalized initial condition on the bubble wall radius will enable us to perform a global phase plane analysis to explore the properties of the autonomous system and to develop some knowledge about the physical parameters that lead to different classes of solutions. Afterwards, the initial conditions defined by Eq. (3.11b) will be used to look at a specific set of trajectories in the phase plane and how they relate to the global analysis.

Applying Eq. (3.16) to (3.15), one can write

$$\frac{d}{du}\left(u^3 v^2\right) = \frac{2\gamma}{u}\frac{1}{(1+Q)^5} - \frac{2u}{(1+Q)^3} + 2u^2\frac{F_C}{(1+Q)^2} \ . \qquad (3.26)$$

Using Eq. (3.26), one can derive an expression for the phase plane trajectory by computing the derivative on the left-hand side and solving the equation for dv/du. The result is

$$\frac{dv}{du} = \frac{\dfrac{\gamma}{(1+Q)^5} - \dfrac{u^2}{(1+Q)^3} + \dfrac{u^3 F_C}{(1+Q)^2} - \dfrac{3}{2}v^2 u^3}{u^4 v} = \frac{P(u,v)}{Q(u,v)} \qquad (3.27)$$

which defines the bubble wall velocity as a function of the bubble wall radius and the other physical parameters of the flow. The singular points of the autonomous system are located at those points which satisfy the conditions $Q = P = 0$. Because $u > 0$, $Q = 0$ when the initial condition for the bubble wall velocity is

satisfied. Thus, all singular points are located along the u-axis at positions satisfying $P(u,0) = 0$. Evaluating $P(u,0) = 0$, one gets the cubic equation

$$u^3 - \frac{1}{F_C(1 + Q)} u^2 + \frac{\gamma}{F_C(1 + Q)^3} = 0$$

which is exactly the same as Eq. (3.22). As we saw earlier, the roots of Eq. (3.22) define the locations on the u-axis of the maximum and minimum points of the potential energy function. Thus, we can say that the location of the maximum and minimum points on the potential energy curve correspond exactly to the location of the singular points of the system.

In order to determine the character of these singularities one can apply Liapunov's Method (see Ref. [15]) which requires finding the characteristic roots of the Jacobian matrix

$$\begin{bmatrix} \frac{\partial Q}{\partial u}(u,0) & \frac{\partial P}{\partial u}(u,0) \\ \frac{\partial Q}{\partial v}(u,0) & \frac{\partial P}{\partial v}(u,0) \end{bmatrix}.$$

The value of u in the argument of each derivative function corresponds to the values of the real roots denoted by Eq. (3.20) for $F_C = 0$ and Eq. (3.25) for $F_C \neq 0$.

When $F_C = 0$, the characteristic equation is

$$\lambda^2 = -2u^5 \tag{3.28a}$$

or

$$\lambda_{1,2} = \pm i \frac{\sqrt{2}}{(1 + Q)^5} u^5. \tag{3.28b}$$

When Eq. (3.28b) is evaluated at the positive root of Eq. (3.20),
the result is two purely imaginary characteristic roots meaning
the positive root is characterized as a vortex point. In a small
neighborhood in the phase plane, all motion will circle around this
vortex point thus defining a periodic solution for u.

When $F_C \neq 0$, the characteristic equation becomes

$$\lambda^2 = -\frac{2}{(1 + Q)^5} u^5 + \frac{3F_C}{(1 + Q)^6} u^6 \quad . \tag{3.29}$$

By evaluating Eq. (3.29) at the positive roots of Eq. (3.22), one
can determine the nature of those roots. For the smallest positive
root in Eq. (3.25b), the characteristic roots are purely imaginary
meaning the root is a vortex point. For the largest root in
Eq. (3.25b), the characteristic roots are both real meaning the
root is a saddle point. The location of the saddle point
corresponds to the outermost limit on the u-axis that a trajectory
representing a periodic solution will pass. Ma and Wang [17]
obtained similar results for this specific case. These results
are also completely consistent with those of Parkin [11] who found
for $F_C = 0$ that only one vortex point exists. And for $F_C \neq 0$,
a vortex and saddle point exist on the u-axis with the vortex
point located closer to the initial radius u_0 than the saddle
point. Moreover, the roots that lie on the negative u-axis are
not pertinent to our problem and should not affect the solution.

Rearranging Eq. (3.17) for the bubble wall velocity, one can write

$$\dot{u} = \pm \sqrt{\dfrac{\dfrac{2\gamma}{(1 + Q)^5} \ell nu - \dfrac{1}{(1 + Q)^3} (u^2 - u_o) + \dfrac{2}{3} \dfrac{F_C}{(1 + Q)^2} (u^3 - u_o)}{u^3}}$$

(3.30)

which defines the family of trajectories in the positive phase plane. The family of curves resulting from Eq. (3.30) is a series of closed loops and open curves representing periodic and non-periodic solutions, respectively. The plus and minus designation of Eq. (3.30) defines the trajectories above and below the u-axis. The extent of the closed loop periodic solutions is determined by the location of the singularities which were found to coincide with the position on the u-axis of the minimum and maximum potential energies. Plots of the potential energy and phase plane trajectories are shown in Figs. 20 and 21. Figure 20 corresponds to the potential energy and phase plane trajectories when $F_C = 0$, $\gamma = 1.4$. Notice the location of the minimum potential energy corresponds to the vortex point in the phase plane about which the periodic trajectories are focused. It is important to point out that the location of the minimum potential energy translates from left to right as the value of Q decreases from Q = 0.30 to Q = 0.00. The dotted curve in the upper potential energy plot corresponds to the case where the trajectory and the vortex are isolated at the origin in the phase plane for a critical value of Q_{crit} = 0.183216. This critical motion is then defined by $u(\tau) = 1$ and $\dot{u}(\tau) = 0$ for all time. The importance of this critical condition is that it separates two physically distinct types of motion that the bubble experiences depending on its initial size. The trajectories to the left of

DIMENSIONLESS INITIAL RADIUS, $r(0) = 1 + Q$ $(Q < 1)$
NORMALIZED INITIAL CONDITION, $u(0) = 1$

POTENTIAL ENERGY, V

0.050

0.025

0

-0.025

-0.050

-0.075

PHASE-PLANE
AND POTENTIAL
ENERGY FOR $\gamma = 1.4$

0.6   0.8   1.0   1.2   1.4   1.6

NORMALIZED BUBBLE RADIUS, $u = \dfrac{r}{1 + Q}$

$u_V = \dfrac{\sqrt{\gamma}}{1 + Q}$

NORMALIZED BUBBLE WALL VELOCITY, $\dot{u} = \dfrac{\dot{r}}{1 + Q}$

0.3

0.2

0.1

0

-0.1

-0.2

-0.3

$Q = 0.30$

$Q = 0.25$

u_V

$Q = 0.0$

$Q = 0.05$

VORTEX IS LOCATED
AT THE NORMALIZED
INITIAL CONDITION
FOR $Q_{CRIT} = 0.183216$
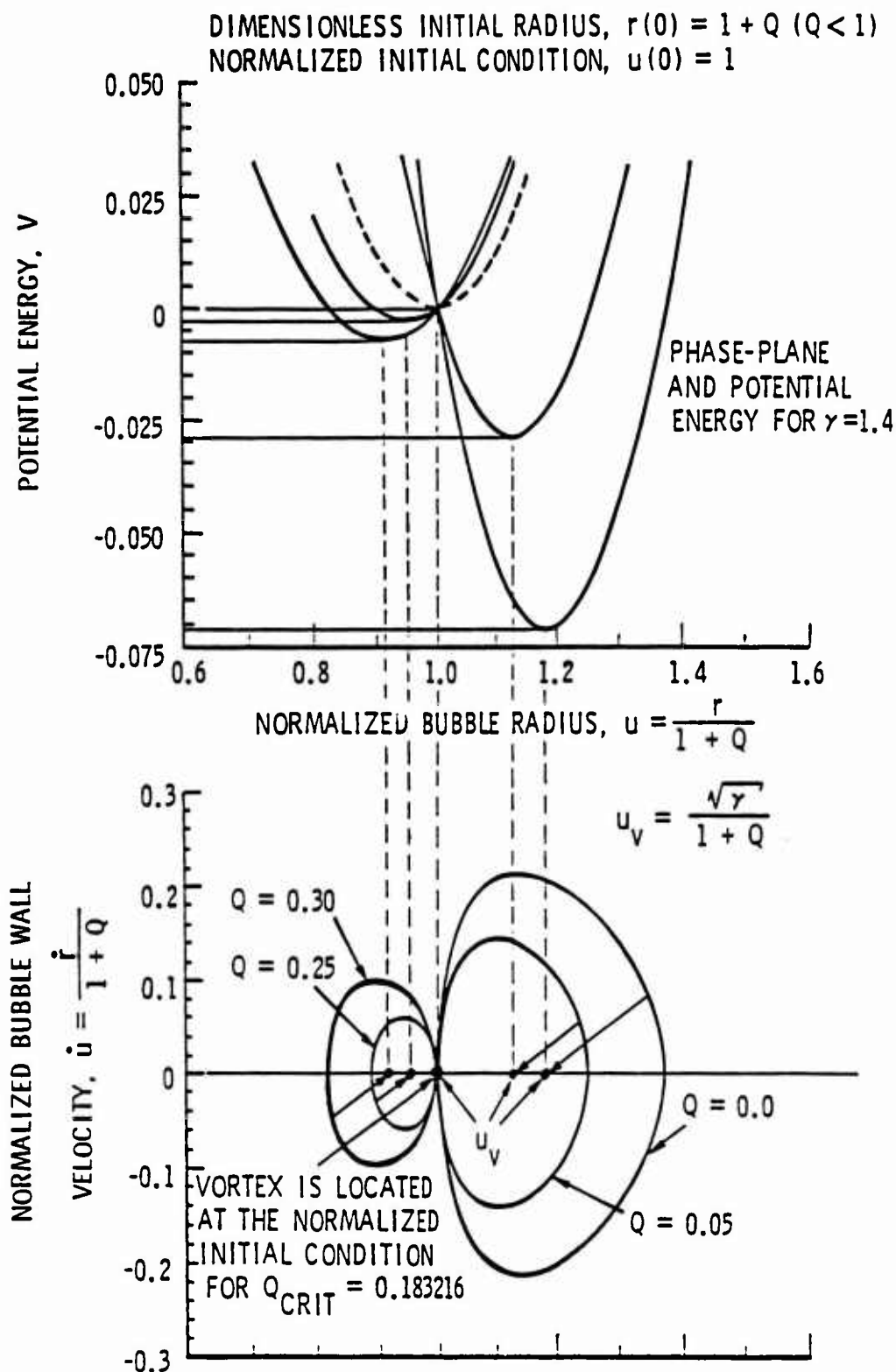
Figure 20. Phase Plane and Level Line Potential Energy Plot
for the Zero-Order Analysis when $F_c = 0$.
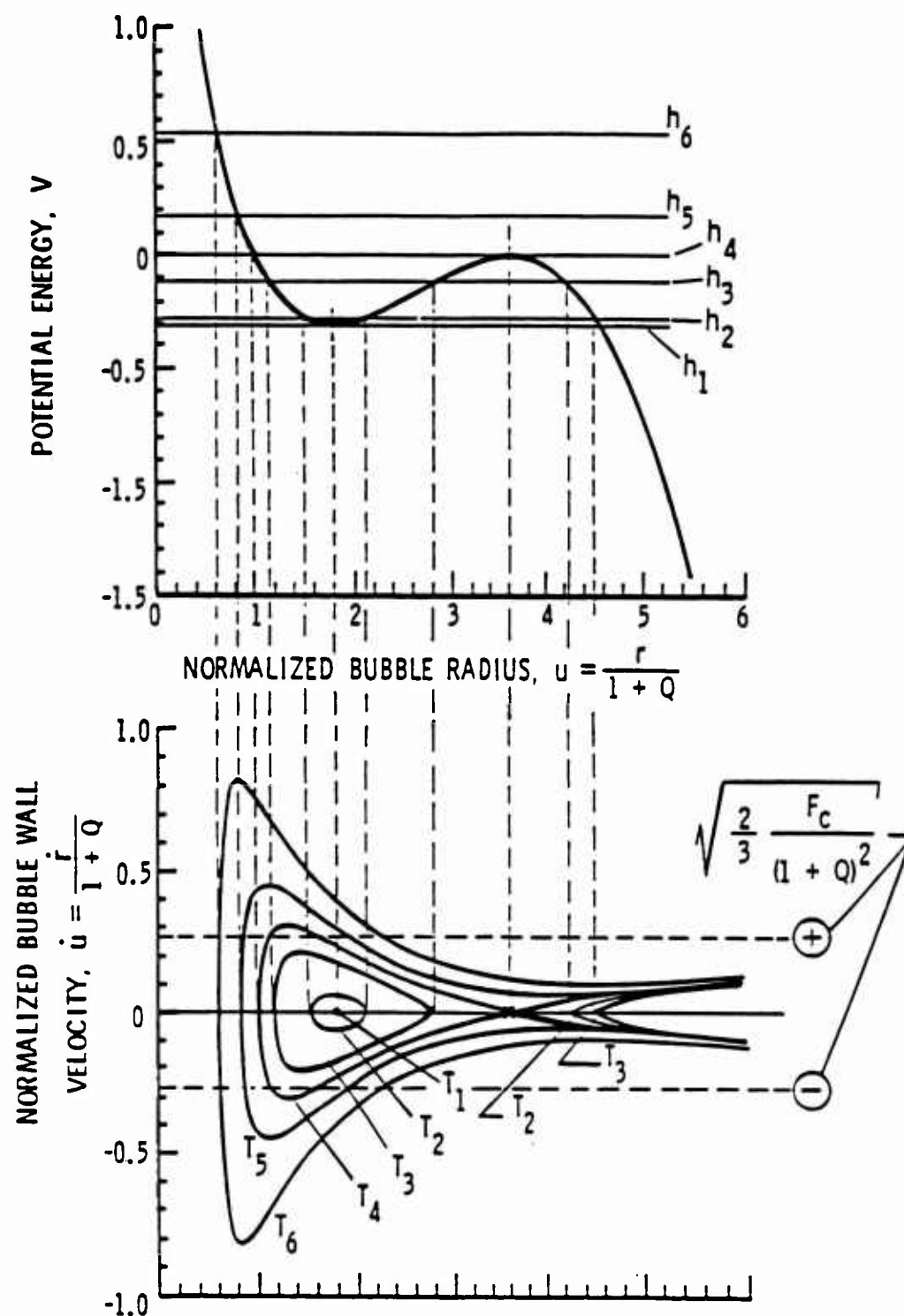
Figure 21. Phase Plane and Level Line Potential Energy Plot for the Zero-Order Analysis when $F_c \neq 0$.

$u(\tau) = 1$ represent small scale oscillations of a flaccid air bubble while those to the right of $u(\tau) = 1$ have larger amplitudes of oscillation involving vaporous growth. Since we are considering primarily the vaporous growth region, we will limit our discussion and investigation to those trajectories that lie to the right of $u(\tau) = 1$. The location of the vortex points, which coincides with the minimum potential energies, is defined by

$$u_v = \frac{\sqrt{\gamma}}{(1 + Q)} \ .$$ (3.31)

Thus, one can write at $u_v = 1$

$$Q_{crit} = \sqrt{\gamma} - 1$$ (3.32)

for any value of γ. If $Q = 0$, then $\gamma = 1$ which is the lowest possible value of the dissolved air content for positive Q values. Since Q was previously defined in Eq. (2.63) as

$$Q = \frac{KWe}{8} \ ,$$

the minimum limit on Q corresponds to $V_o = 0$ or $K = 0$.

If one now considers the potential energy and phase plane trajectories for $F_C \neq 0$ at $\gamma = 1.4$, it can be seen from Fig. 21 that the nature of the curve is quite different from the case when $F_C = 0$. To simplify the analysis we will look at only one energy curve with its corresponding phase plane trajectories. From Fig. 21 one can see that the minimum point on the energy curve coincides with the vortex point in the phase plane while the maximum energy point concides with the saddle point. The location of the saddle point defines the maximum normalized bubble radius through which a trajectory

representing a periodic solution passes. Therefore, all trajectories representing periodic solutions lie to the left of the saddle point and circle about the vortex point located just to the right of some generalized initial condition $u(0) = 1 + Q$.

The outermost trajectory representing a periodic solution and passing through the saddle point is called the separatrix. The parameters that define the separatrix as the outermost limit of all periodic trajectories is characterized by the critical parameters γ_c and $F_{C_{crit}}$. These critical parameters are determined by simultaneous solution of

$$V(u) = 0 \tag{3.33}$$

and

$$\frac{dV}{du}(u) = 0 \quad . \tag{3.34}$$

Equations (3.33) and (3.34) are to be evaluated at the location of the saddle point as determined from Eq. (3.25). All trajectories that lie outside of the separatrix represent bubbles which will grow to an infinite radius across an infinite time interval. In this study we are mainly interested in the trajectories that represent periodic solutions.

To solve for the critical parameters that determine the separatrix, one can write Eqs. (3.33) and (3.34) as

$$V(u) = \frac{2\gamma}{(1 + Q)^5}\, \ell n u - \frac{1}{(1 + Q)^3}\, (u^2 - 1) + \frac{2}{3}\, \frac{F_C}{(1 + Q)^2}\, (u^3 - 1) = 0$$

$$\tag{3.35}$$

and

$$\frac{dV}{du} = \frac{2\gamma}{(1+Q)^5}\frac{1}{u} - \frac{u}{(1+Q)^3} + \frac{F_C}{(1+Q)^2}u^2 = 0 \quad . \tag{3.36}$$

Solving Eqs. (3.35) and (3.36) for γ and then solving simultaneously for $F_{C_{crit}}$ one gets

$$F_{C_{crit}} = \frac{3(u^2 - 1) - 6u^2\ell nu}{(1+Q)[2(u^3 - 1) - 6u^3\ell nu]} \tag{3.37}$$

which defines the critical forcing parameter as a function of Q.
Rearranging Eq. (3.36) for γ and substituting Eq. (3.37) for $F_{C_{crit}}$ one can write the expression for γ_{crit} as

$$\gamma_{crit} = (1+Q)^2 u^2 \left[1 - u\left(\frac{u^2(\frac{1}{2} - \ell nu) - \frac{1}{2}}{u^3(\frac{1}{3} - \ell nu) - \frac{1}{3}}\right)\right] \quad . \tag{3.38}$$

Thus, Eqs. (3.37) and (3.38) are the critical parameters which when used in conjunction with Eq. (3.30) define the critical trajectory called the separatrix. Parkin [11] asserted that the separatrix corresponded to a barrier between Class 1 and Class 4 solutions for a non-zero forcing function parameter, F_C. Recall that a Class 4 solution corresponds to a bubble which grows to an infinite radius in an infinite amount of time. If one chooses a value of the forcing parameter larger than that of $F_{C_{crit}}$ or an air content larger than γ_{crit}, then the trajectories corresponding to a Class 4 solution would be found outside of the separatrix. Choosing values of γ_{crit} and $F_{C_{crit}}$ near zero results in small scale oscillations about the vortex point and is classified as a Class 1 solution. Critical values of the air content parameter and forcing function parameter evaluated at the location of the

saddle point for Q = 0.30 are $F_{C_{crit}}$ = 0.1834101 and

γ_{crit} = 3.1022749. Figure 22 is a plot of the critical parameters

versus the normalized bubble radius. In this study we are

interested in values of u > 1. Therefore, it is not necessary to

begin the origin of u at zero. It is important to note that the

magnitudes calculated for the critical parameters in Fig. 22 and the

amplitude and frequency of oscillation indicates in Fig. 21 are

comparable to those calculated by Parkin [11]. This apparent

consistency in the generalized phase plane allows us to consider the

more specific case of the phase plane when we use the initial

conditions formulated earlier. Also, if we let u → ∞ then we

see the phase plane trajectories asymptotically approach a value

equal to

$$\dot{u} = \pm \sqrt{\frac{2}{3} \frac{F_C}{(1 + Q)^2}} \; . \tag{3.39}$$

The asymptotes are represented by the horizontal dotted lines on

the phase plane plot in Fig. 21 and apply to non-periodic

trajectories as τ → ∞.

If one analyzes the phase plane when the initial conditions of

Eq. (3.11b) are used, the resulting equation is similar to

Eq. (3.30) except that u(0) = 1. The phase plane equation is

written as

$$\dot{u} = \pm \sqrt{\frac{\dfrac{2\gamma}{(1 + Q)^5} \ell n u - \dfrac{1}{(1 + Q)^3} (u^2 - 1) + \dfrac{2}{3} \dfrac{F_C}{(1 + Q)^2} (u^3 - 1)}{u^3}}$$

$$\tag{3.40}$$
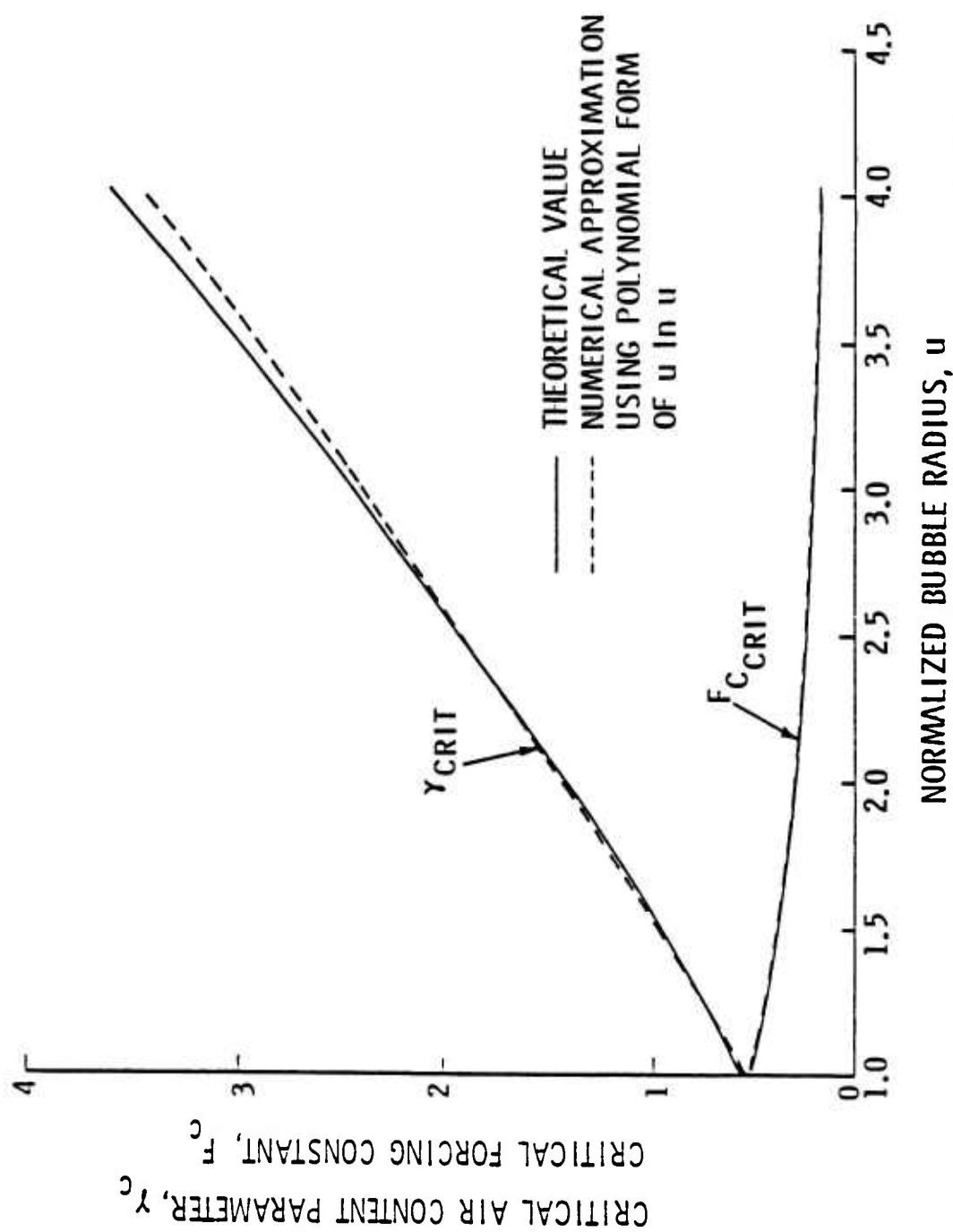
Figure 22. Critical Parameters, Y_{crit} and $F_{C_{crit}}$, that will Produce a Bubble Growth in Accordance with the Separatrix.

which satisfies the initial conditions exactly. By varying the
forcing function parameter F_C about the value of the critical
parameter $F_{C_{crit}}$, one obtains the phase plane plot shown in Fig. 23.
Notice that all trajectories begin from $u = 1$, $\dot{u} = 0$ and follow a
trend similar to the trajectories shown in the general phase plane.
As noted earlier in the derivation of $\dot{u}(0)$, the value of $\dot{u}(0)$ has
a magnitude approximately equal to 1×10^{-8} fps. The fact that this
initial velocity is not equal to zero is very important because it
allows us to explain the existence of the trajectories when there
is no forcing. If one looks at the parabolic coefficients of the
forcing function represented by Eq. (2.54), it is easy to see that
the zeroth order term $C_1 = 0.0$. Therefore if the bubble has zero
wall velocity at the initial point, then the bubble will grow only
if a force favorable to growth is applied. Because the zeroth
order forcing constant is zero there must be an initial wall
velocity enabling the bubble to traverse along any one trajectory
as shown in Fig. 23. Otherwise the phase plane would be
represented by a single point in the phase plane at $\dot{u} = 0$, $u = 1$.
Thus, approximation of the initial velocity as zero allows one to
simplify the equations without sacrificing the accuracy of the
calculation.

In summary, we have looked at the phase plane plots, potential
energy and singularities for the autonomous zeroth order differen-
tial equation $F_C > 0$ and $F_C = 0$. The singularities which exist in the
system for $F_C > 0$ explicitly define the limits between periodic and
non-periodic solutions. The character of these singularities was
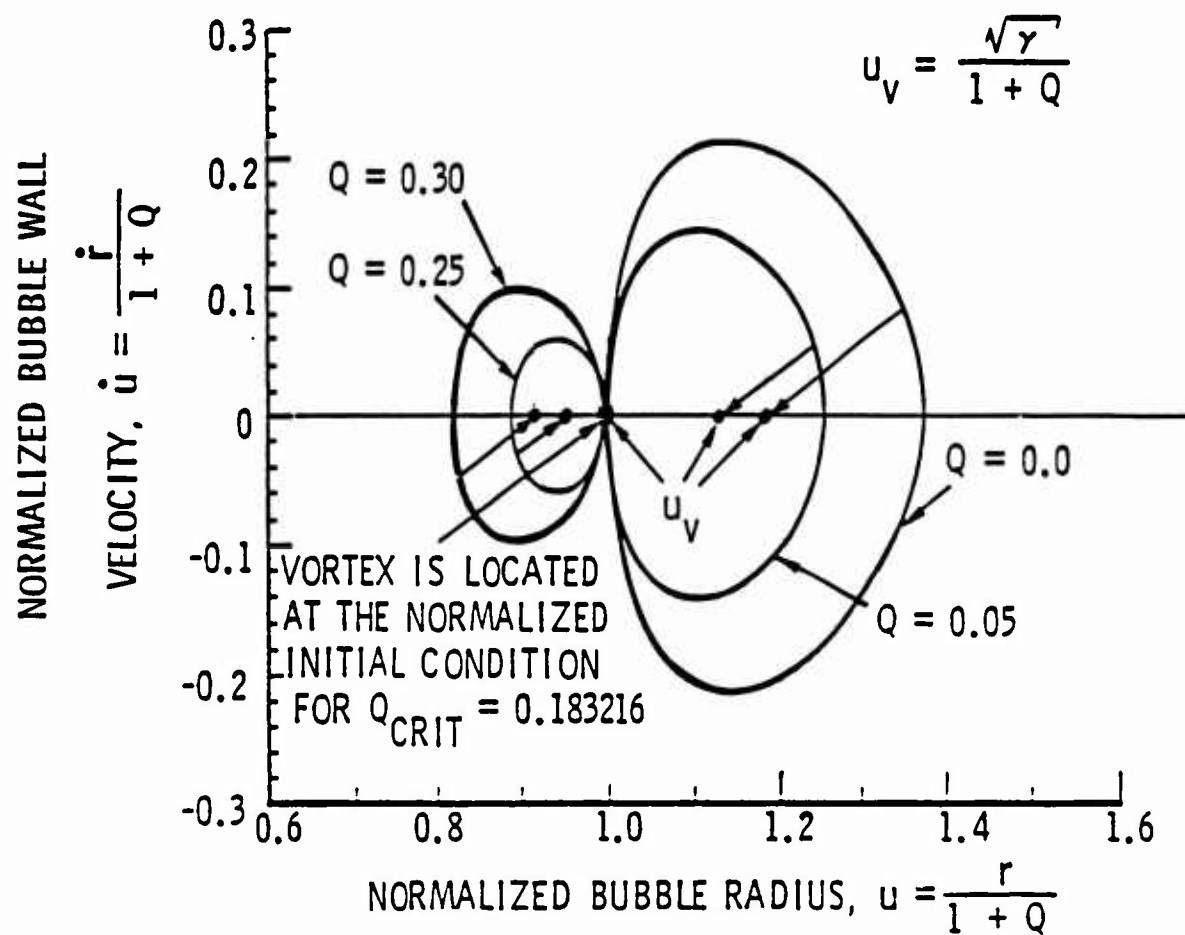
Figure 23.   Phase–Plane Trajectories Originating From the Initial Conditions.

verified by Liapunov's Method and revealed a vortex point near the general initial condition u = u(0) and a saddle point located farther away from the initial radius. As a result, the phase plane plot showed trajectories representing periodic solutions circling about the vortex point while the saddle point acted as a bridge between the periodic and non-periodic trajectories. Also, the location along the u-axis of the vortex and saddle points was exactly the same as the location of the minimum and maximum points exhibited by the potential energy function. Using the location of the saddle point, we were able to derive from the potential energy function and its derivative expressions for the critical parameters γ_c and $F_{C_{crit}}$ which are used in Eq. (3.40) to define the separatrix. The separatrix which is now a function of Q and u is used to show the separation between Class 1 and Class 4 solutions. Thus, the trajectory representing the separatrix is the outermost limit where a periodic solution exists. All solutions within the separatrix are periodic motions and are the main focus of this study. And all trajectories representing periodic or non-periodic solutions approach an asymptotic value indicating a constant rate of growth or collapse of a bubble as its radius grows infinitely.

Having established limits between the periodic and non-periodic solutions, one is now ready to put the zeroth order differential equation into integral form in order to determine an approximate solution of the individual bubble oscillations.

3.2.1.3 Polynomial approximation of the logarithmic air content parameter

In an effort to solve the zeroth order differential equation, one must rewrite Eq. (3.40) using the positive root only as

$$\frac{du}{d\tau} = \frac{\sqrt{\frac{2\gamma}{(1+0)^5}\ell nu - \frac{1}{(1+0)^3}(u^2-1) + \frac{2}{3}\frac{F_C}{(1+0)^2}(u^3-1)}}{u^{3/2}}$$

(3.41)

By inverting the variables in Eq. (3.41), an expression for the period of oscillation can be written in the form of a definite integral as

$$\tau = \int_{u=1}^{u} \frac{x^{3/2}dx}{\sqrt{\frac{2\gamma}{(1+0)^5}\ell nx - \frac{1}{(1+0)^3}(x^2-1) + \frac{2}{3}\frac{F_C}{(1+Q)^2}(x^3-1)}}$$

(3.42)

The lower limit of the integral is the initial normalized radius while the upper limit is the value of the normalized radius u, between u = 1 and u = u_s where u_s corresponds to the maximum value of u when $\dot{u}$ = 0 in the phase plane plot in Fig. 23. As it stands, Eq. (3.42) is not soluable by any standard analytic technique. It closely resembles the form of an elliptic integral except that the numerator does not have a whole numbered exponent and the denominator contains a natural log term.

In order to shape Eq. (3.41) into a form which may be solved by some known analytic technique, one must first multiply the numerator and denominator by the square root of the normalized radius. The integral is then

$$\tau = \int\limits_{u=1}^{u=U_s} \frac{u^2 du}{\sqrt{\dfrac{2\gamma}{(1+Q)^5} u \, \ell n u - \dfrac{1}{(1+Q)^3}(u^3 - u) + \dfrac{2}{3}\dfrac{F_C}{(1+Q)^2}(u^4 - u)}}$$

(3.43)

which still contains a natural logarithm in the denominator. Generally, one would numerically integrate Eq. (3.43) and probably obtain very accurate results. Because the emphasis of this study is to obtain an analytic solution to the Rayleigh-Plesset equation, certain modifications of Eq. (3.43) must be made enabling one to get an analytic solution to the zero order equation. If one considers the function $u \ell n u$, which is contained within the square root of the denominator, it is easily seen that the function is a rather smooth function of constantly increasing magnitude. By fitting the $u \ell n u$ function with a cubic polynomial the entire denominator can be written as the square root of a polynomial. For the zero order equation, the term $F_C = 0$. Then the polynomial in the denominator would be a cubic .

In order to fit the $u \ell n u$ function with a cubic polynomial four points must be used to model the function in the region of interest. Thus, for the four points, u_1, u_2, u_3, u_4, one writes

$$f(u_1) = u_1 \ell n u_1 = a u_1^3 + b u_1^2 + c u_1 + d$$

$$f(u_2) = u_2 \ell n u_2 = a u_2^3 + b u_2^2 + c u_2 + d$$

(3.44)

$$f(u_3) = u_3 \ell n u_3 = a u_3^3 + b u_3^2 + c u_3 + d$$

$$f(u_4) = u_4 \ell n u_4 = a u_4^3 + b u_4^2 + c u_4 + d \quad .$$

In matrix form, Eq. (3.44) is written as

$$
\begin{bmatrix}
u_1^3 & u_1^2 & u_1 & 1 \\
u_2^3 & u_2^2 & u_2 & 1 \\
u_3^3 & u_3^2 & u_3 & 1 \\
u_4^3 & u_4^2 & u_4 & 1
\end{bmatrix}
\begin{bmatrix}
a \\
b \\
c \\
d
\end{bmatrix}
=
\begin{bmatrix}
u_1 \ell n u_1 \\
u_2 \ell n u_2 \\
u_3 \ell n u_3 \\
u_4 \ell n u_4
\end{bmatrix}
$$

which when solved with the IMSL subroutine called LINV3F produces
the coefficients

$$a = - 0.050304$$

$$b = 0.578693$$

$$c = - 0.001871$$

$$d = - 0.526519 \quad .$$

The numerical values of u_1, u_2, u_3, u_4 corresponded to the values of
the normalized radius starting at the initial condition $u_1 = 1$ and
ending close to the location of the saddle point $u_4 = 3.60$. Points
u_2 and u_3 were arbitrarily chosen to be $u_2 = 1.80$ and $u_3 = 2.60$.
Table 1 shows the % error between the function $u\ell n u$ and the cubic
polynomial $f = au^3 + bu^2 + cu + d$. It is evident that the error
falls in the range of $-1.0\% <$ error $< 1.0\%$.

To see the effect of the approximation on the zeroth order
equation, one can rewrite Eq. (3.40) using the cubic polynomial to
get

TABLE 1

Polynomial Curve Fit of $u \ln u$

u	$u \ln u$	$f = au^3 + bu^2 + cu + d$	% error
1.0	0.00000	0.00000	0.00000
1.2	0.21879	0.21763	− 0.53019
1.4	0.47106	0.46707	− 0.84794
1.6	0.75201	0.74590	− 0.81249
1.8	1.05802	1.05171	− 0.59681
2.0	1.38629	1.38208	− 0.30376
2.4	2.10112	2.10686	+ 0.27318
2.6	2.48433	2.49644	+ 0.48737
2.8	2.88293	2.90092	+ 0.62408
3.2	3.72208	3.74495	+ 0.61441
3.6	4.61136	4.61963	+ 0.17927

$$\dot{u} = \pm \sqrt{\dfrac{\dfrac{2\gamma}{(1+Q)^5}(au^3 + bu^2 + cu + d) - \dfrac{1}{(1+Q)^3}(u^3 - u) + \dfrac{2}{3}\dfrac{F_C}{(1+Q)^2}(u^4 - u)}{u^2}}$$

(3.45)

Using Eq. (3.45) with the values of γ_c and $F_{C_{crit}}$ when $Q = 0.30$, the separatrix is calculated and compared to the original calculation using the $u\ell nu$ function in Fig. 24. Clearly, the accuracy of the cubic fit on the logarithm term resulted in a very nice fit of the separatrix. We can expect any future calculations to be equally accurate.

Rewriting Eq. (3.43) with cubic polynomial fit and $F_C = 0$, one gets

$$\tau = \int_{u=1}^{u} \frac{u^2 du}{Au^3 + Bu^2 + Cu + D}$$

(3.46)

where the coefficients of the polynomial in the demoniator are

$$A = \frac{2\gamma a}{(1+Q)^5} - \frac{1}{(1+Q)^3} \qquad\qquad B = \frac{2\gamma b}{(1+Q)^5}$$

$$C = \frac{2\gamma c}{(1+Q)^5} + \frac{1}{(1+Q)^3} \qquad\qquad D = \frac{2\gamma d}{(1+Q)^5}.$$

(3.47)
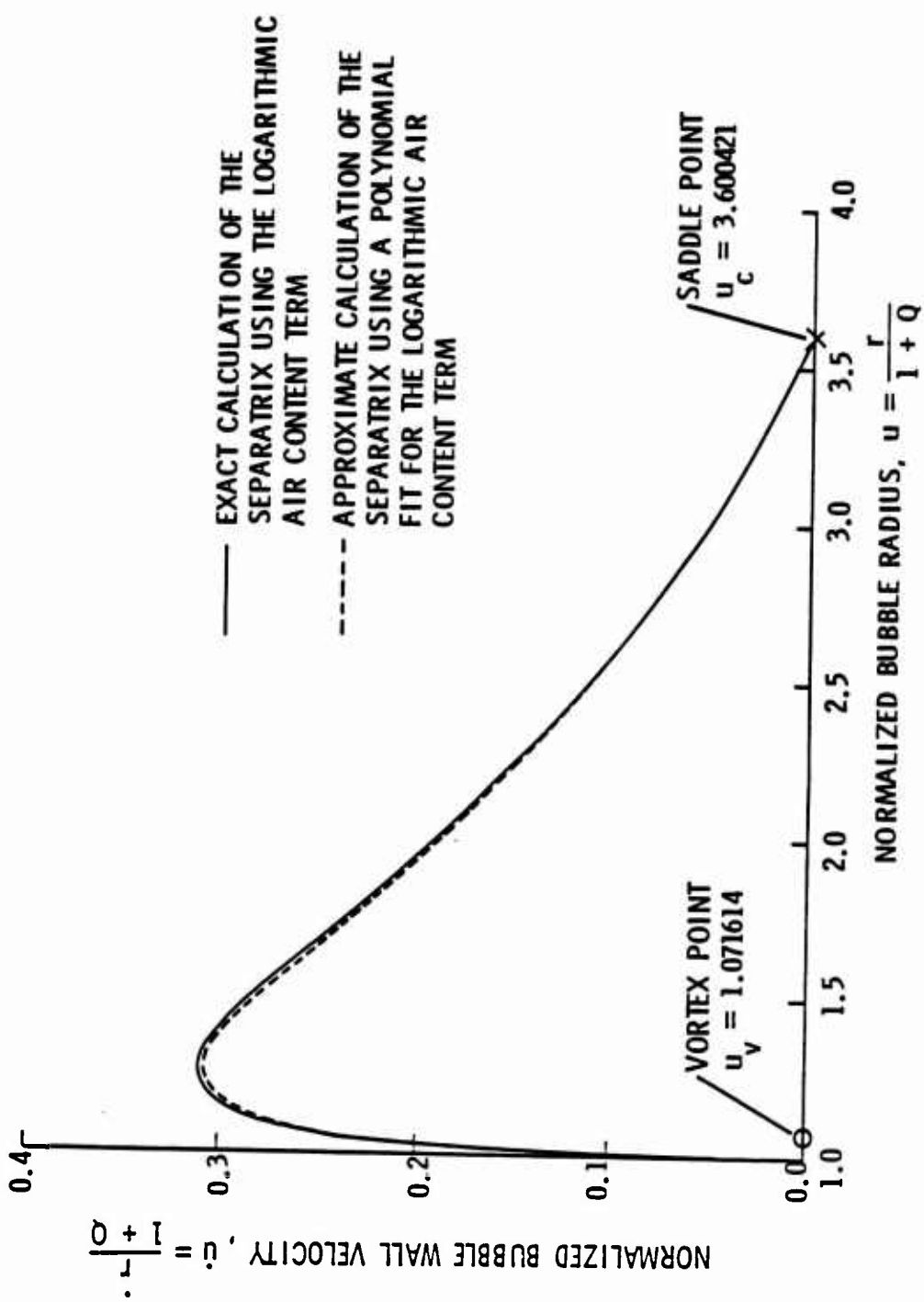
Figure 24. Separatrix Comparison Using the Polynominal Approximation to the Logarithmic Air Content Parameter.

Now, Eq. (3.46) is in a form which allows one to calculate analytically the value of the integral. Solution of the integral will be completed in the next section.

3.2.1.4 An Approximate Zero Order Solution using Elliptic Functions

Having established an approximate form of the integral representing the period of oscillation of a bubble, an analytic solution in the form of elliptic functions must be formulated. Because the numerator is a squared term and the denominator is the square root of a polynomial, an integral from Byrd and Friedman [13] can be applied. The solution is dependent on the roots of the denominator and can be expressed in terms of incomplete elliptic integrals, the first, second and third kinds and a product of Jacobian elliptic functions.

The first thing to do is to calculate the three roots of the cubic polynomial in the denominator of the integrand. Because the roots can vary due to the choice of γ and Q, we will choose $\gamma = 1.4$ and $Q = 0.0$ to get the largest possible roots available for the zero order solution.

Using Eq. (3.46), the radicand should be written as

$$A\left[u^3 + pu^2 + qu + r\right]$$

where $p = B/A$, $q = C/A$ and $r = D/A$. If we set

$$u_v = \frac{\sqrt{\gamma}}{1 + Q} \quad,$$

which denotes the phase-plane location of the vortex point.

Then the coefficients p, q, r and A become

$$p = \frac{2bu_v^2}{2au_v^2 - 1} \quad ,$$

$$q = \frac{2cu_v^2 + 1}{2au_v^2 - 1} \quad ,$$

$$r = \frac{2du_v^2}{2au_v^2 - 1} \quad ,$$

$$A = \frac{1}{(1 + Q)^3} \left[2au_v^2 - 1\right] \quad .$$

Letting the three real roots of this modified cubic be u_1, u_2 and u_3, we can order the roots as

$$u_1 > u > u_2 > u_3$$

with u_1 being the largest root and u_3 being the smallest. From Fig. 20 it is clear to see that all the trajectories in the phase plane originate from $u = 1$. We can therefore assume that the modified cubic always has a root at unity. Normally the cubic can be factored using Tartaglia's Method, but because we know one of the roots is $u = 1$ the other roots can be found by dividing the modified cubic by $u - 1$ and solving the resulting quadratic equation.

Long division of the modified cubic by $u - 1$ gives

$$x^2 + x(p + 1) + (q + p + 1)$$

with a remainder of

$$\frac{2u_v^2(a + b + c + d)}{2au_v^2 - 1} \quad .$$

Then with the numerical values of the coefficients a, b, c and d from the curve fit of $u \ln u$ (p. 85), one can calculate the remainder to be equal to zero. Therefore, the remaining two roots are found from the quadratic equation. Upon factorizing the quadratic equation and applying the appropriate coefficients, the remaining two roots are

$$\left| \frac{1.0568u_v^2 - 1}{2(1 + 0.100608u_v^2)} \right| \left| 1 \pm \sqrt{1 + \frac{4.212144u_v^2(1 + 0.100608u_v^2)}{(1.0568u_v^2 - 1)^2}} \right| \quad .$$

The numerical equivalents of these two roots when $\gamma = 1.4$ and $Q = 0.0$ are

$$u = 1.3662$$

and

$$u = -0.9459 \quad .$$

Comparison of all three roots with the range of integration as prescribed by the phase plane of Fig. 20 justifies the ordering of the roots as

$$u_1 = 1.3662 \quad , \quad u_2 = 1.00 \quad , \quad u_3 = -0.9459 \quad .$$

Consequently Eq. (3.46) can be rewritten using u_1, u_2 and u_3 as

$$\tau = \sqrt{\frac{(1 + Q)^3}{(2au_v^2 - 1)}} \int_{u=1}^{u} \frac{x^2 du}{(x_1 - x)(x - x_2)(x - x_3)} \qquad (3.48)$$

Since all trajectories shown in Fig. 20 originate at $u = 1$, the analysis conducted above for the trajectories that lie to the right of $u = 1$ should also work for the trajectories that lie to the left of $u = 1$.

It has been previously stated (p. 75) that the trajectories to the left of $u = 1$ represent small scale oscillations of a flaccid air bubble. Indeed, the main focus of this work is to study the bubble growth as it occurs in the vaporous growth region. However, in an effort to maintain completeness in the solution of the zero-order equation one should be able to use a similar factorization as shown above to define the ordering of the roots for the trajectories to the left of $u = 1$. These roots could then be used in the solution of Eq. (3.48) to describe the time history of these small scale flaccid air bubble oscillations.

Considering the same factorization as before, the roots are written as

$u_1 = 1.0$

$$u_{2,3} = \frac{2au_v^2 + 2bu_v^2 - 1}{2(1 - 2au_v^2)}$$

$$\left[1 \pm \sqrt{1 + \frac{8u_v^2(a + b + c) - 16u_v^4(a^2 + ab + ac)}{\left(2au_v^2 + 2bu_v^2 - 1\right)^2}} \right] \quad .$$

Using a polynomial curve fit for the function $u\ell nu = au^3 + bu^3 + cu + d$

where

$$a = -0.205484$$

$$b = 1.111631$$

$$c = -0.606996$$

$$d = -0.299157$$

over the range $u = 0.8$ to $u = 1.0$, one can write

$$u_{2,3} = \frac{1.8123u_v^2 - 1}{2(1 + 0.41095u_v^2)}$$

$$\left[1 \pm \sqrt{1 + \frac{2.39326u_v^2(1 + 0.41095u_v^2)}{\left(..8123u_v^2 - 1\right)^2}} \right] \quad .$$

Choosing $\gamma = 1.4$ and $Q = 0.30$ then one finds the parameter u_v equal to $u_v = 0.910166$ and the roots are

$$u_1 = 1.00$$

$$u_2 = 0.823184$$

$$u_3 = -0.449188$$

Therefore, the ordering of the roots as

$$u_1 > u > u_2 > u_3$$

is equivalent to the ordering of the roots for the trajectories that lie to the right of $u = 1$. Comparison of the roots u_1, u_2 and u_3 against the roots as calculated by numerical methods resulted in errors of approximately 0.60%. Thus, the factorization method is a reliable means by which the roots of the cubic polynomial in the denominator of Eq. (3.46) can be calculated.

It is interesting to note that when values of γ and Q are chosen such that the parameter u_v increases in magnitude from less than one to greater than one, the roots u_1, u_2 and u_3 migrate from left to right along the u-axis. When the parameter u_v equals unity there is a double root at $u = 1$ which sets the upper and lower limit of Eq. (3.48) equal to unity. Previous analysis reminds us that for a double root at unity a bubble radius will neither increase nor decrease in size as time increases. Thus, it will be at this point that the analysis will continue, considering only values of the parameter u_v greater than or equal to unity, even though an equivalent analysis could be performed for values of u_v less than one. Refering to Byrd and Friedman, Eq. (3.48) can be written as

$$\tau = g b^m \frac{1}{\alpha^4} \left[\alpha_1^4 u + 2\alpha_1^2 (\alpha - \alpha_1^2) V_1 + (\alpha^2 - \alpha_1^2)^2 V_2 \right]$$

where

$$V_1 = \frac{1}{k'^2} \left[E(\phi,k) - k^2 SnuCdu \right]$$

$$(3.49)$$

$$V_2 = \frac{1}{3k'^4} \left[2(2 - k^2)E(\phi,k) - k'^2 F(\phi,k) \right.$$

$$\left. - k^2 SnuCdu \left(k'^2 nd^2 u + 4 - 2k^2 \right) \right] \; .$$

The parameters in Eq. (3.49) are functions of the roots, u_1, u_2 and u_3 and are defined as follows:

Modulus

$$k = \sqrt{\frac{u_1 - u_2}{u_1 - u_3}}$$

Complimentary Modulus

$$k' = \sqrt{1 - k^2}$$

$$g = \frac{2}{\sqrt{u_1 - u_3}}$$

Modular Angle

$$\phi = \operatorname{Sin}^{-1} \sqrt{\frac{(u_1 - u_3)(u - u_2)}{(u_1 - u_2)(u - u_3)}}$$

Note: u is the upper limit of integration.

Incomplete Elliptic Integral of the First Kind

$$F(\phi,k) = \int_0^\phi \frac{d\theta}{\sqrt{1 - k^2\sin^2\theta}}$$

Incomplete Elliptic Integral of the Second Kind

$$E(\phi,k) = \int_0^\phi \sqrt{1 - k^2\sin^2\theta}\ d\theta$$

Jacobian Elliptic Functions

$$Snu = \sin\phi = \sqrt{\frac{(u_1 - u_3)(u - u_2)}{(u_1 - u_2)(u - u_3)}}$$

$$Cnu = \cos\phi$$

$$dnu = \sqrt{1 - k^2\sin^2\phi}$$

$$ndu = \frac{1}{dnu}\ .$$

Rewriting Eq. (3.49) in terms of u_1, u_2 and u_3, one gets

$$\tau = F(\phi,k)\left[gu_3^2 - gu_2^2\left(1 - \frac{u_3}{u_2}\right)^2 \frac{1}{3k'^2}\right]$$

$$+ E(\phi,k)\left[2gu_2u_3\left(1 - \frac{u_3}{u_2}\right)\left(\frac{1}{k'^2}\right) + gu_2^2\left(1 - \frac{u_3}{u_2}\right)^2\left(\frac{2(2 - k^2)}{3k'^4}\right)\right]$$

$$- SnuCdu\left[2gu_2u_3\left(1 - \frac{u_3}{u_2}\right)\left(\frac{k^2}{k'^2}\right) + gu_2^2\left(1 - \frac{u_3}{u_2}\right)^2\left(\frac{k^2}{3k'^4}\right)(4 - 2k^2)\right]$$

$$- SnuCdund^2u\left[gu_2^2\left(1 - \frac{u_3}{u_2}\right)^2\left(\frac{k^2}{3k'^2}\right)\right] \quad . \tag{3.50}$$

Now, if one considers the terms inside the square parentheses
in Eq. (3.50) for a particular value of Q and γ, the quantities
inside the square parentheses are considered constant. All
combinations of the elliptic functions in front of the square
parentheses are functions of ϕ which are functions of the variable
u. Therefore, $\tau = f(u)$ which is the inverse of what we want; namely,
$u = f(\tau)$. Also, since all the elliptic functions in Eq. (3.50) do
not have well defined inverses, an alternate strategy must be used
to invert Eq. (3.50) in order to write an expression describing the
growth of the normalized bubble radius versus the bubble time.

Since all terms in the square parentheses in Eq. (3.50)
represent constants, one can rewrite Eq. (3.50) as

$$\tau = F(\phi,k)V_1 + E(\phi,k)V_2 - SnuCduV_3 - SnuCdund^2uV_4 \tag{3.51}$$

where V_1, V_2, V_3 and V_4 are constants for a particular value of Q and γ. Now since the sum of the elliptic functions in Eq. (3.51) does not have a known inverse, an approximation of each function must be derived that allows one to invert the equation to get $u = f(\tau)$. Because the functions $F(\phi,k)$ and $E(\phi,k)$ are defined as definite integrals, a numerical routine must be used to evaluate the functions across the range of the roots u_1 and u_2. The functions $F(\phi,k)$ and $E(\phi,k)$ are considered incomplete elliptic integrals when $\phi < \pi/2$. If $\phi = \pi/2$ then the functions are considered complete and are tabulated in Byrd and Friedman's Table of Elliptic Integrals [13]. Unfortunately, the tables are not comprehensive enough to include every possible value of $F(\phi,k)$ and $E(\phi,k)$ for different values of ϕ so that the numerical routine utilizing Simpson's 1/3 Rule was used.

In Fig. 25, the function $F(\phi,k)$ was plotted as a function of the modular angle ϕ. Because the values of Q and γ vary in accordance with the different phase plane trajectories located to the right of the initial condition as shown in Fig. 20, extreme values of k were computed to represent those trajectories. Using these extreme values of k, curves representing the maximum and minimum range that the function $F(\phi,k)$ would fall are plotted as solid lines in Fig. 25. All other values that $F(\phi,k)$ might attain would lie in between those two solid lines. Recall the modulus k is defined by
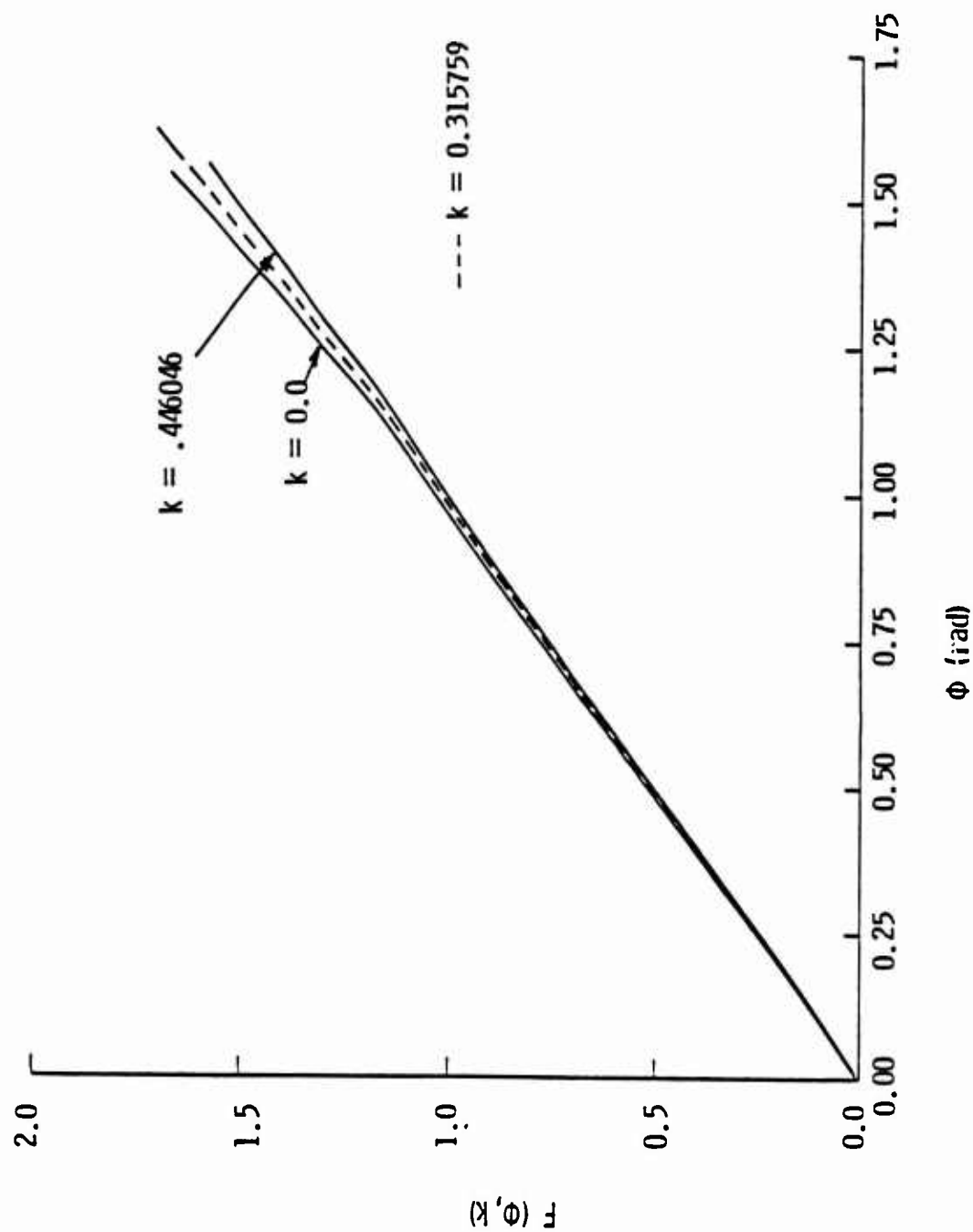
$$k = \sqrt{\frac{u_1 - u_2}{u_1 - u_3}} \tag{3.52}$$

Figure 25. Plots of the Incomplete Elliptic Integral of the First Kind as a Function of the Modular Angle ϕ and the Modulus, k.

where u_1, u_2 and u_3 are the roots of the cubic polynomial in the denominator of Eq. (3.46). When $Q = 0.183216$ and $\gamma = 1.4$, the minimum potential energy falls directly on the initial condition. The cubic polynomial in the denominator of Eq. (3.46) has double root at $u_1 = u_2 = 1.0$. Consequently, $k = 0$ is the minimum value of k used to plot the extreme upper value of the elliptic function. Likewise, when $Q = 0.0$ and $\gamma = 1.4$, the cubic polynomial has roots such that $u_1 > u_2 > u_3$. The result is a maximum value of $k = 0.446046$ which is used to compute the extreme lower value of the elliptic functions. This same procedure can be used for the other elliptic functions that come out of Eq. (3.51). Notice that for $F(\phi,k)$ and $E(\phi,k)$, the maximum curve corresponds to $k = 0$. The opposite is true when looking at the curves for SnuCdu and SnuCdund^{2}u in Figs. 27 and 28.

Having determined a maximum and minimum range for the elliptic functions, it was of great benefit to derive a separate functional representation for each elliptic function shown in Figs. 25 through 28. To do this, a median curve lying in the middle of the two solid lines of each figure was plotted. The median curve is shown as a dotted line and was calculated using $k = 0.315759$ as the modulus. Each median line is used to represent the entire range of each elliptic function since there could be an infinite number of representative curves for all combinations of Q and γ chosen. Finally, since each median line is roughly parabolic in shape, a parabolic approximation of each dotted line in Figs. 25 through 28
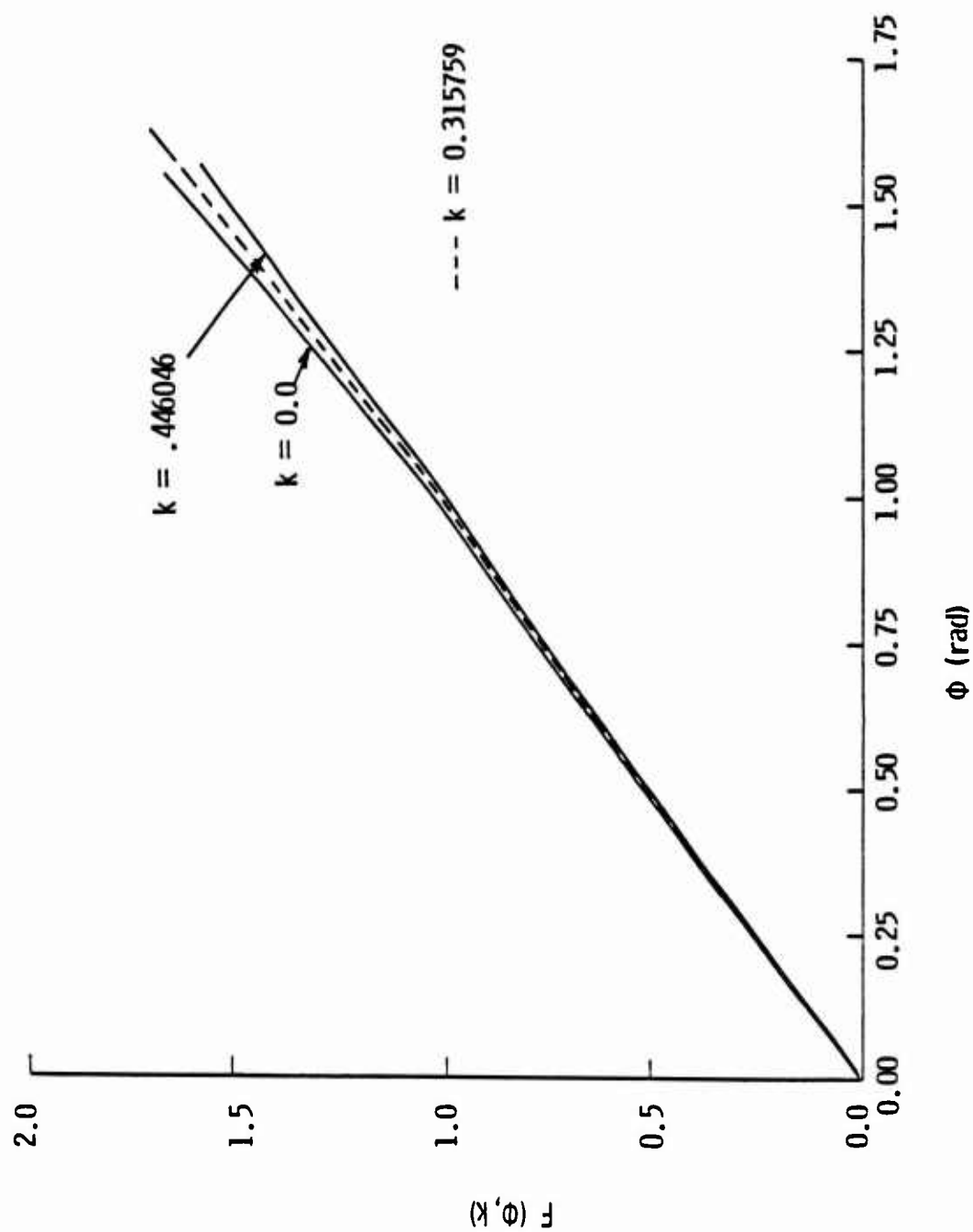
Figure 26. Plots of the Incomplete Elliptic Integral of the Second Kind as a Function of the Modular Angle ϕ and the Modulus, k.
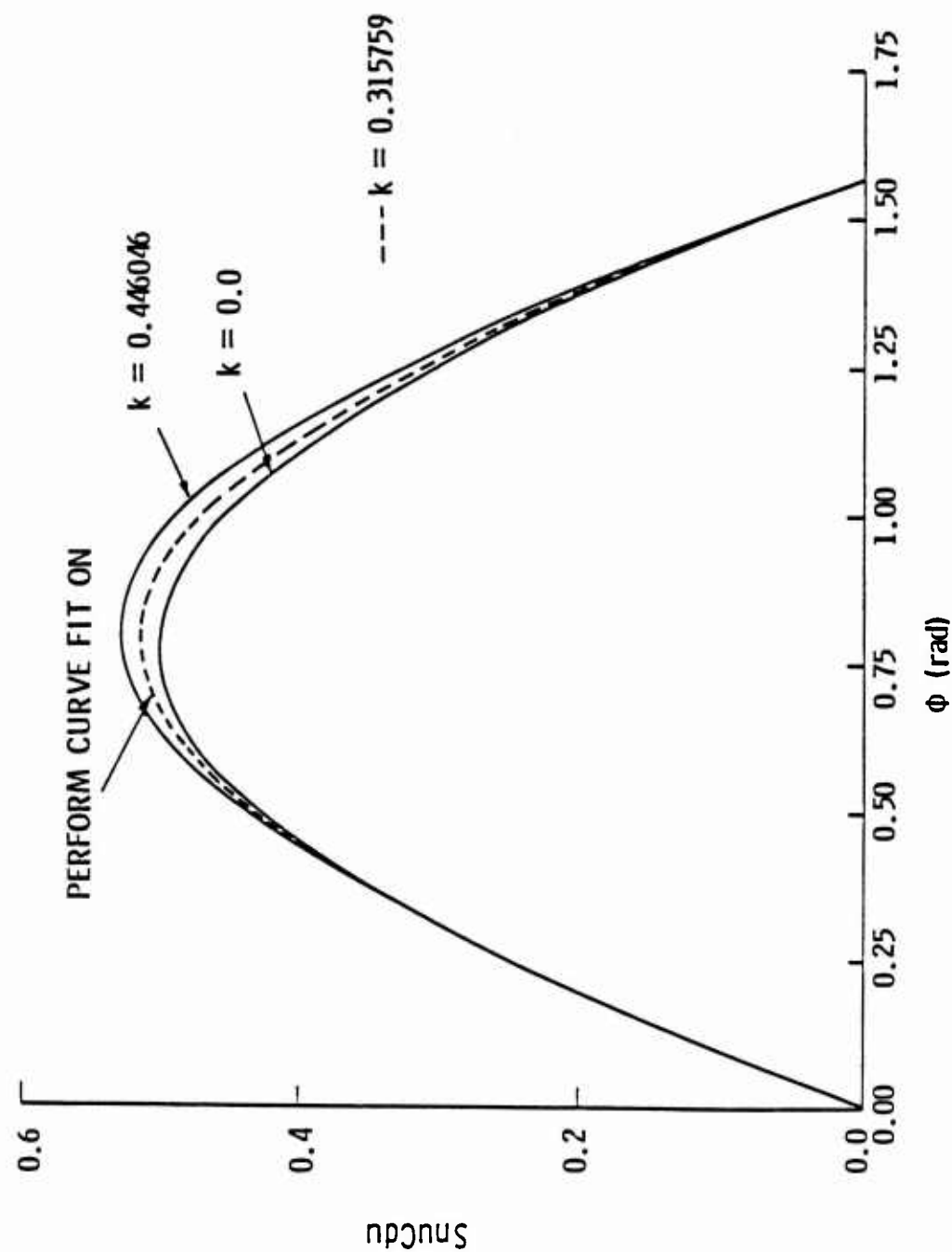
Figure 27. Plots of the Jacobian Elliptic Function Product SnuCdu as a Function of the Modular Angle φ and Modulus, k.
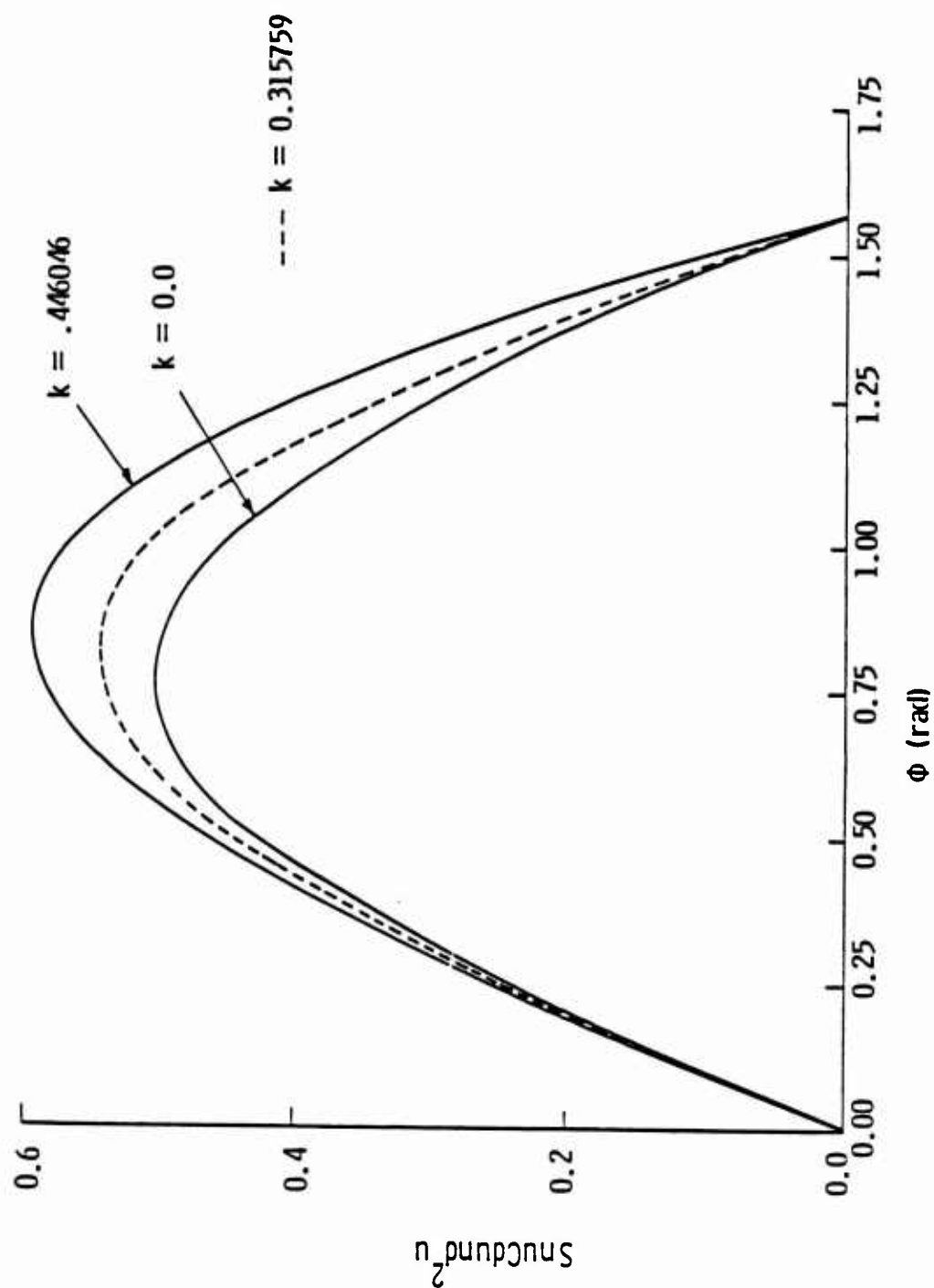
Figure 28. Plots of the Jacobian Elliptic Function Product SnuCdund²u as a Function of the Modular Angle φ and Modulus, k.

was derived. The coefficients were derived by fitting each dotted

line at three representative points starting with the zero point.

Using the following parabolic equations

$$F(\phi,k) = A_1\phi^2 + B_1\phi + C_1$$

$$E(\phi,k) = A_2\phi^2 + B_2\phi + C_2$$

$$(3.53)$$

$$SnuCdu = A_3\phi^2 + B_3\phi + C_3$$

$$SnuCdund^2u = A_4\phi^2 + B_4\phi + C_4$$

the coefficients were computed as

$$A_1 = 0.021844$$

$$B_1 = 0.992116$$

$$A_2 = -0.02073$$

$$B_2 = 1.007155$$

$$A_3 = -0.83226$$

$$B_3 = 1.307305$$

$$A_4 = -0.88065$$

$$B_4 = 1.38332$$

$$C_1 = C_2 = C_3 = C_4 = 0.0 \quad .$$

Figures 29 through 32 are plots of the resultant curve fits (dotted line) of the median representative of the various elliptic functions (solid lines). Now, one can rewrite Eq. (3.51) as

$$\tau = V_1(A_1\phi^2 + B_1\phi + C_1) + V_2(A_2\phi^2 + B_2\phi + C_2)$$

$$+ V_3(A_3\phi^2 + B_3\phi + C_3) + V_4(A_4\phi^2 + B_4\phi + C_4) \tag{3.54}$$

which has no term larger than second order in ϕ.

Grouping like powers of ϕ, we write Eq. (3.54) in the general form of a parabola as

$$\tau = \bar{a}\phi^2 + \bar{b}\phi + \bar{c} \tag{3.55}$$

where

$$\bar{a} = V_1A_1 + V_2A_2 - V_3A_3 - V_4A_4$$

$$\bar{b} = V_1B_1 + V_2B_2 - V_3B_3 - V_4B_4$$

$$\bar{c} = V_1C_1 + V_2C_2 - V_3C_3 - V_4C_4 \ .$$

It should be noted that Eq. (3.55) is now written as a function of ϕ. But, because the definition of the modular angle ϕ is written as a function of u, we still have $\tau = f(u)$. It is desired to get the inverse $f = g(\tau)$. Therefore, Eq. (3.55) can be inverted by using the quadratic formula. Subtracting τ and applying the quadratic formula, one gets

$$\phi = \frac{-\bar{b} \pm \sqrt{\bar{b}^2 - 4\bar{a}(\bar{c} - \tau)}}{2\bar{a}} \ . \tag{3.56}$$

Figure 29. Parabolic Curve Fit of the Incomplete Elliptic Integral of the First Kind strictly as a Function of the Modular Angle ϕ.
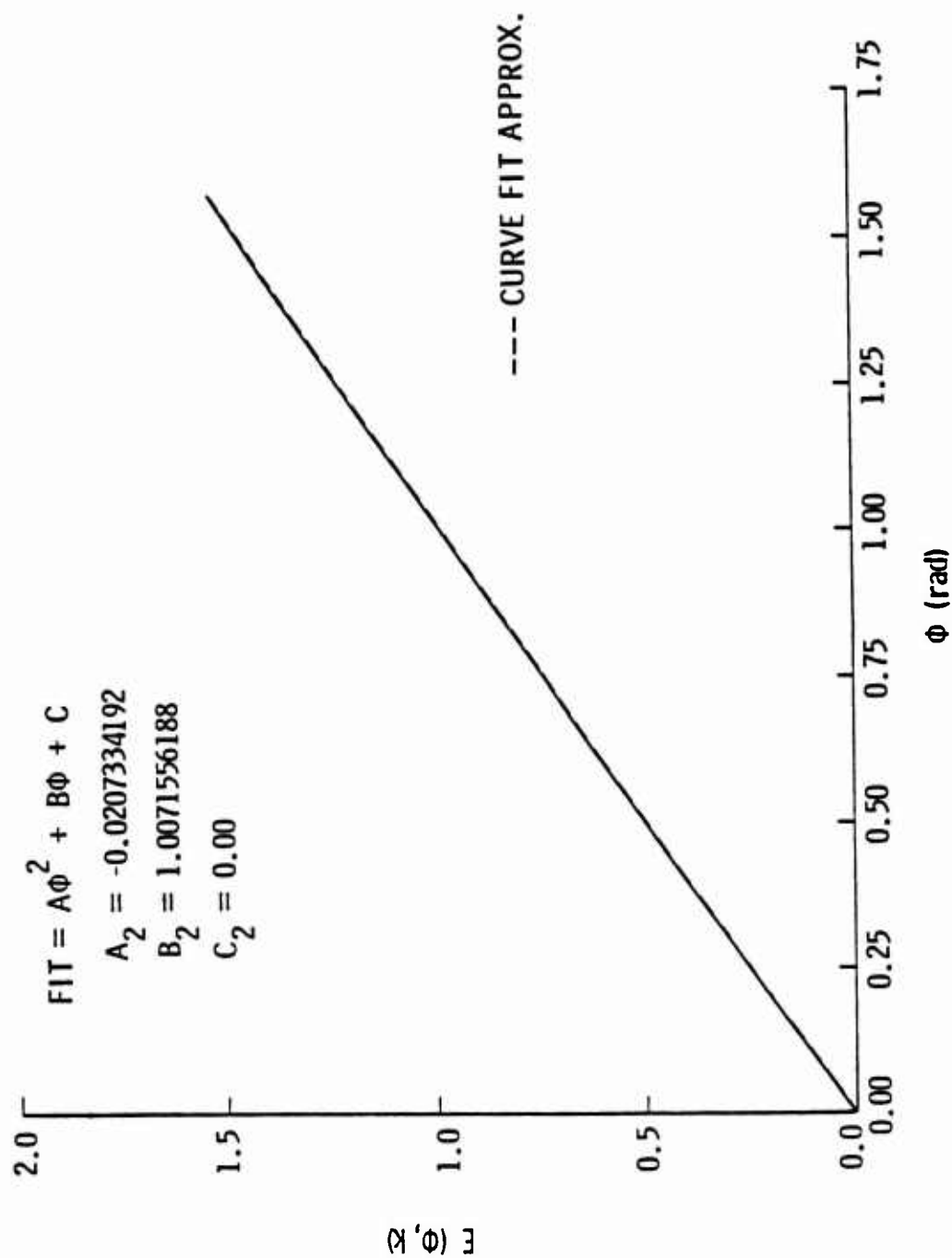
Figure 30. Parabolic Curve Fit of the Incomplete Elliptic Integral of the Second Kind strictly as a Function of the Modular Angle ϕ.

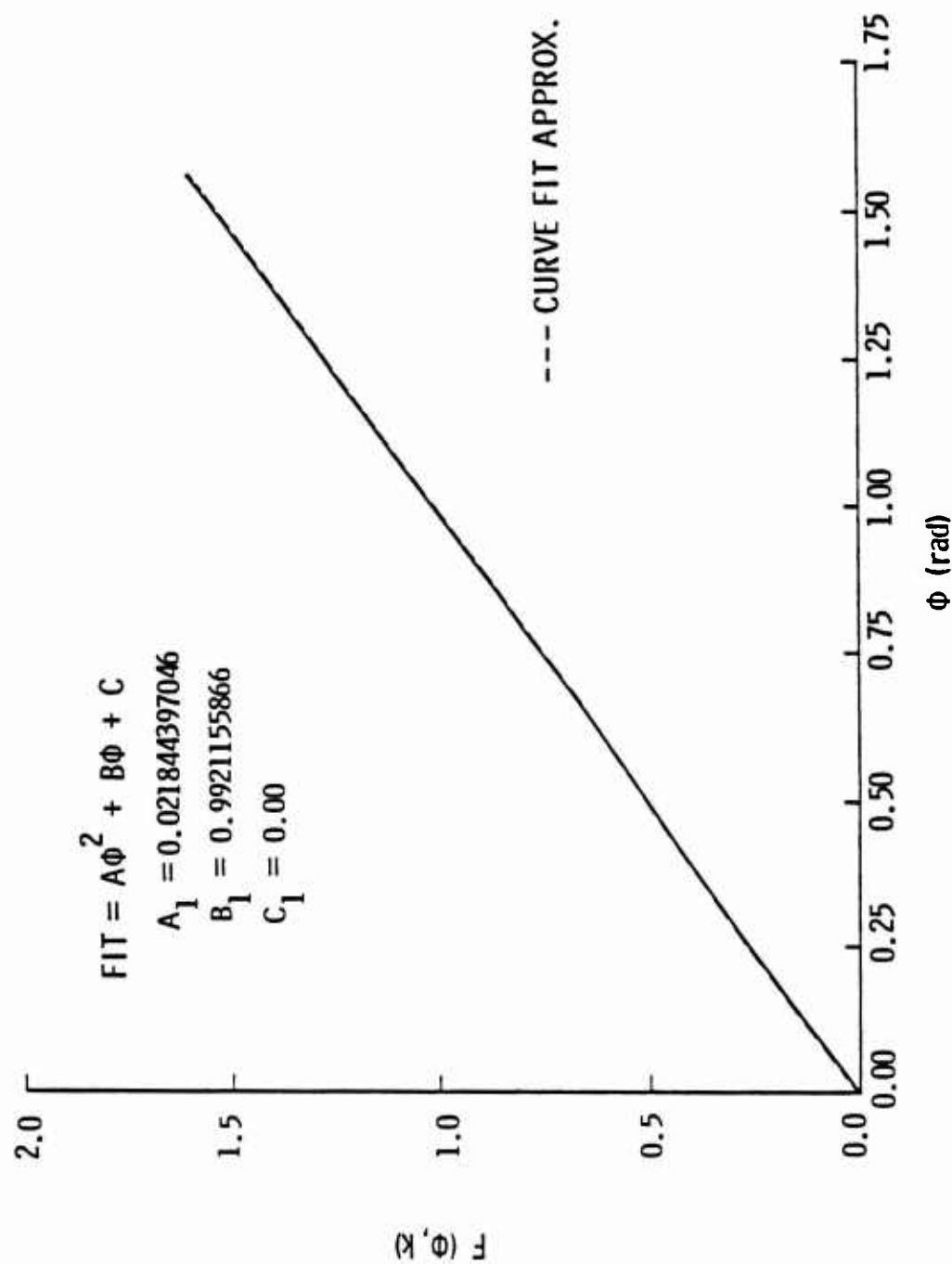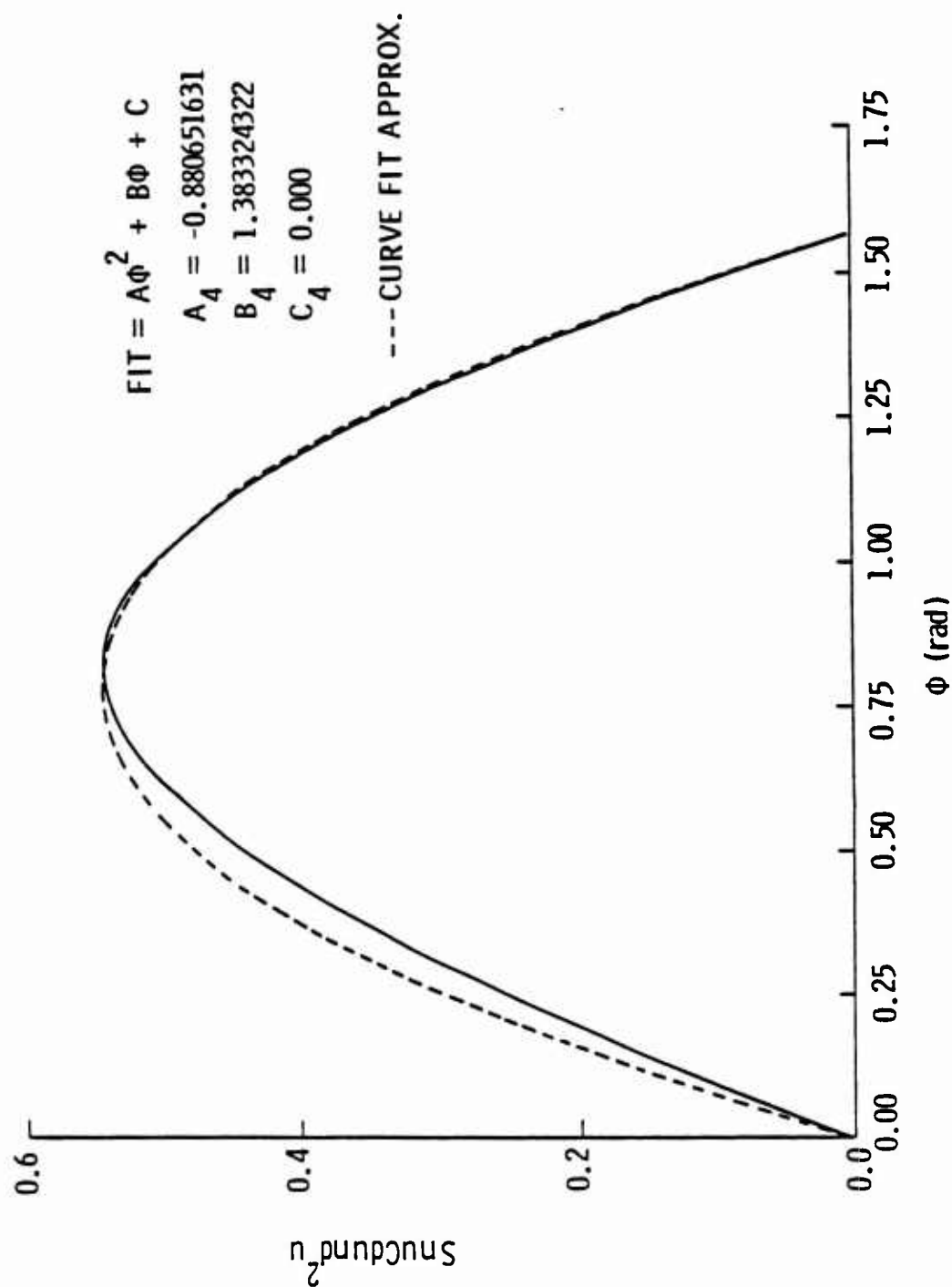Figure 32. Parabolic Curve Fit of the Product of Jacobian Elliptic Functions SnuCdund^{2}u as a Function of the Modular Angle ϕ.

$FIT = A\phi^2 + B\phi + C$

$A_4 = -0.880651631$

$B_4 = 1.383324322$

$C_4 = 0.000$

--- CURVE FIT APPROX.

ϕ (rad)

Snucdund^{2}u

Since $C_1 = C_2 = C_3 = C_4 = 0$ and ϕ must equal zero at $\tau = 0$, one must choose the positive branch of the square root in Eq. (3.56) to represent the inverse. Having established $\phi = f(\tau)$, one can now use the fact that

$$\sin \phi = \sqrt{\frac{(u_1 - u_3)(u - u_2)}{(u_1 - u_2)(u - u_3)}} \tag{3.57}$$

to derive an expression in the form $u = f(\tau)$. Solving for u from Eq. (3.57), one gets

$$u = \left[\frac{(u_3 - u_2)}{k^2 \sin^2 \phi - 1}\right] + u_3 \quad . \tag{3.58}$$

Substituting expressions for $k(u_1, u_2, u_3)$ and ϕ, one can write $u = f(\tau)$ as

$$u = \frac{u_3 - u_2}{\left(\dfrac{u_1 - u_2}{u_1 - u_3}\right) \sin^2 \left(\dfrac{-\bar{b} + \sqrt{\bar{b}^2 + 4\bar{a}\tau}}{2\bar{a}}\right)} + u_3 \tag{3.59}$$

where u_1, u_2 and u_3 are functions of Q, F_C and γ as defined by Eq. (3.25a). The resultant plot of the normalized bubble radius as a function of the bubble time is shown in Fig. 33. Each curve beginning at $\tau = 0$ corresponds to a particular trajectory in the phase plane. Each trajectory is characterized by the author's choice of Q and γ in such a manner that the trajectory is always located at or to the right of the initial condition. Since each trajectory is centered about a vortex point whose location along the u-axis is defined by

$$u_v = \frac{\sqrt{\gamma}}{(1 + Q)} \quad ,$$
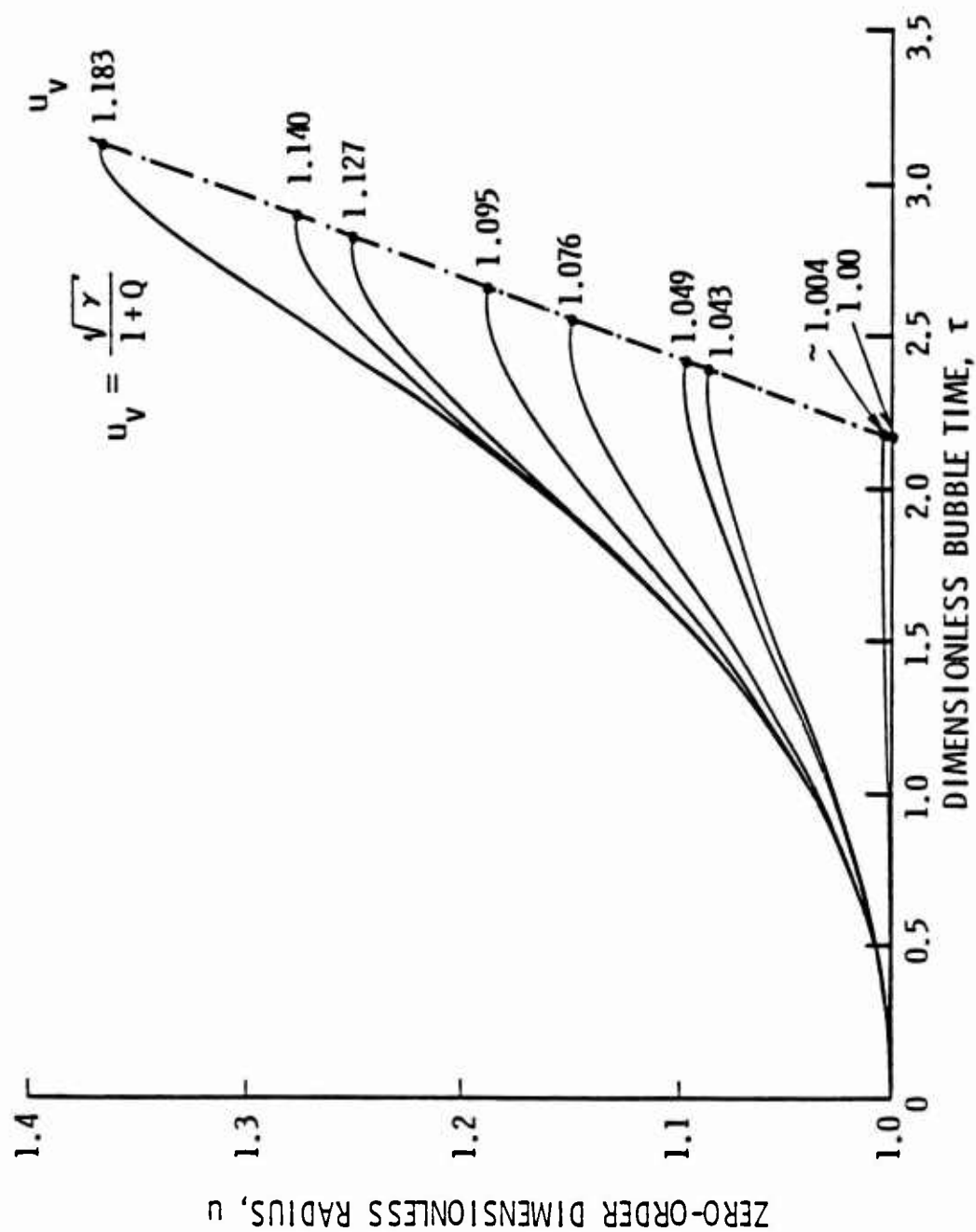
Figure 33. A Plot of Numerical Data Showing the Zero Order Solution, $u = u(\tau)$.

each curve in Fig. 33 has a particular value of u_v labeled at the half period. If the calculation had been carried across the upper and lower half of the phase plane trajectory, then all the curves in Fig. 33 would return to the τ-axis completing a whole period of oscillation.

It is interesting to note that these oscillations are of a very high frequency and as a bubble passes through a region favorable to vaporous growth or collapse, these free oscillations occur a number of times before the bubble reaches the separation point. From Fig. 11, one can determine that at $K = 0.60$ the dimensionless time from the initial point up to the separation point equals approximately 760 units of bubble time, i.e., $\tau = 760$. If the complete period of oscillation is $\tau_{period} \times 6.2$ units of bubble time, one could calculate the number of individual free oscillations to be $N_{cycles} \approx 122$. In laboratory time, this means that a particular bubble will oscillate ≈ 122 times over a time period of 0.144 seconds.

Having established some knowledge about the zeroth order solution in terms of elliptic functions, one now desires a more usable form of the solution, preferably in terms of trigonometric functions, that will closely approximate Fig. 33. Looking at the curves in Fig. 33, one could say they are roughly of the shape $u = 1 - \cos \tau$. Using a more general form of the curve $1 - \cos \tau$, one can write

$$u = A + B \cos\left(\pi \ \tau/\tau_f\right) + C \cos\left(2\pi \ \tau/\tau_f\right) \tag{3.60}$$

where τ_f is the dimensionless time corresponding to the time it takes to reach the end of a half period and A, B and C are coefficients to be determined. Using the following three conditions

$$@ \ \tau = 0 \quad , \quad u = 1 \quad ,$$

$$@ \ \tau = \tau_m \quad , \quad u = u_m \quad ,$$

and

$$@ \ \tau = \tau_f \quad , \quad u = u_f \quad ,$$

one can solve simultaneously for A, B and C to get

$$A = \frac{1}{2} \left(1 + u_f \right) - \frac{u_m - \frac{1}{2}\left(1 + u_f\right) - \frac{1}{2}\left(1 - u_f\right)\cos\left(\pi \ \tau_m/\tau_f\right)}{\cos\left(2\pi \ \tau_m/\tau_f\right) - 1}$$

$$B = \frac{1}{2} \left(1 - u_f \right) \tag{3.61}$$

$$C = \frac{u_m - \frac{1}{2}\left(1 + u_f\right) - \frac{1}{2}\left(1 - u_f\right)\cos\left(\pi \ \tau_m/\tau_f\right)}{\cos\left(2\pi \ \tau_m/\tau_f\right) - 1}$$

The parameters u_m and u_f correspond to the values of u along a line representing midpoint values of the zeroth order solution and the values of u along a line representing values at the end of a half period. Figure 34 shows the lines along which the values of u_m and u_f were taken. Upon plotting these values of u_m and u_f against the parameter u_v, the following curve fits were derived:

$$u_m = - 4.0477 \ u_v^2 + 9.2935 \ u_v - 4.2458 \tag{3.62}$$

$$u_f = 1.99873 \ u_v - 0.99873 \ . \tag{3.63}$$
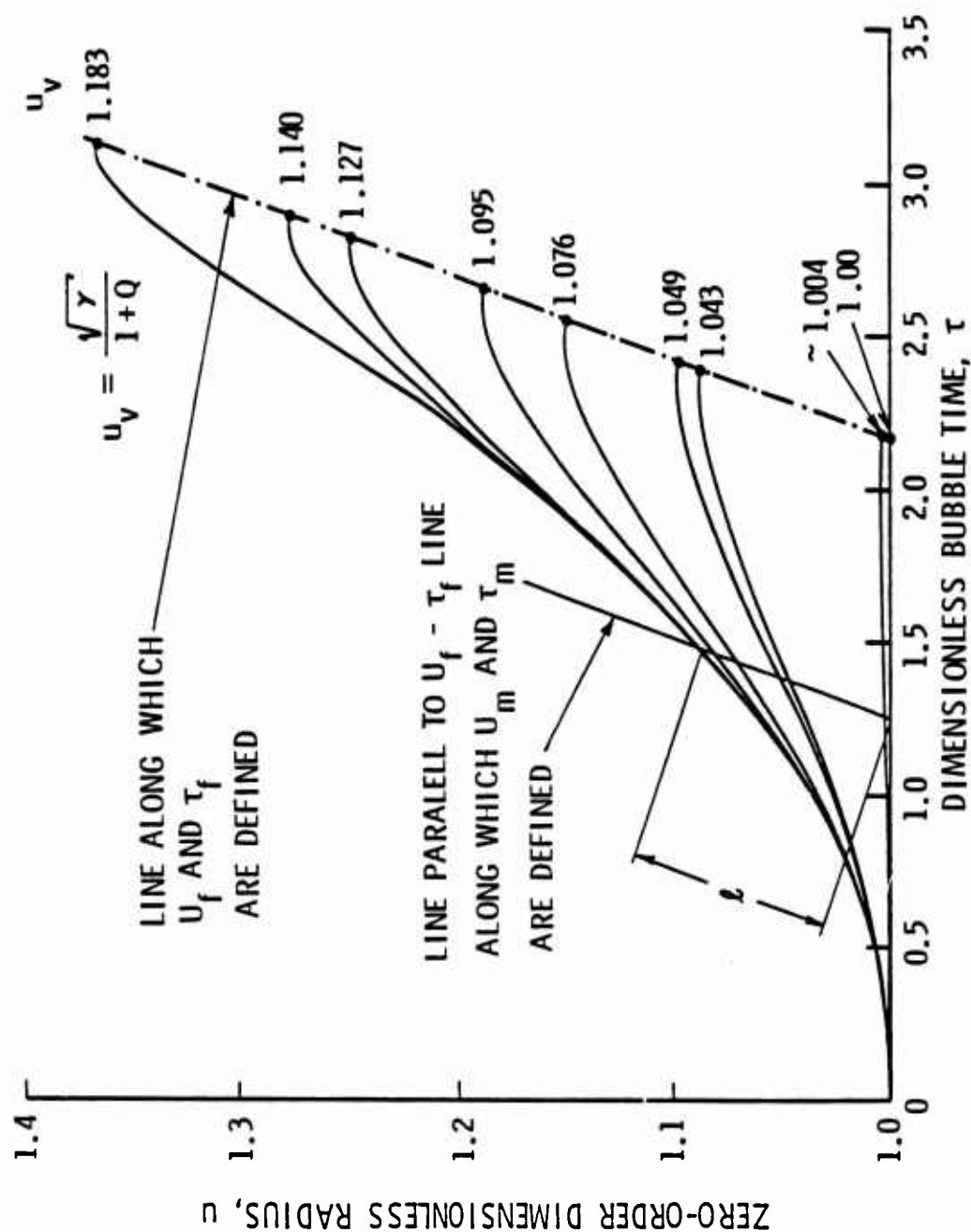
Figure 34. A Plot of the Zero Order Solution Showing some of the Parameters used to Derive a Parametric Solution of the Zero Order Solution.

The times that correspond to the values u_m and u_f are defined as τ_m and τ_f and are read off the same lines that u_m and u_f were in Fig. 34. Plotting τ_m and τ_f against the parameter u_v resulted in a parabolic curve fit for τ_m as

$$\tau_m = 1.25 + \ell \sin \theta \qquad (3.64)$$

where

$$\ell = -4.3239(u_v - 1)^2 + 1.2804(u_v - 1)$$

and a linear fit for τ_f as

$$\tau_f = 2.1587 + 5.6764 \, u_v \sin \theta \quad . \qquad (3.65)$$

The parameter θ defined the angle that the line along which u_f and τ_f deviated from the vertical. Measurement of θ gives $\theta = 1.208$ radians. Figures 35 and 36 show the approximate curve fits of the parameters u_m versus u_v and ℓ versus $(u_v - 1)$. The curve fits show relatively good accuracy and thus can be used with confidence in determining an approximation to the zeroth order solution. Therefore, plotting Eq. (3.60) in combination with Eqs. (3.61), (3.62), (3.63), (3.64) and (3.65) against the dimensionless bubble time τ gives a maximum error of ~ 4.5% of the zero order solution as shown in Fig. 37. In order to reduce the error even more, Eq. (3.60) was rewritten as

$$u = (1 - e)\left[A + B \cos\left(\pi \, \tau/\tau_f\right) + C \cos\left(2\pi \, \tau/\tau_f\right)\right] \qquad (3.66)$$

where e is some functional approximation of the relative error used to reduce the error between the solid and dotted lines shown in Fig. 37. Writing e as
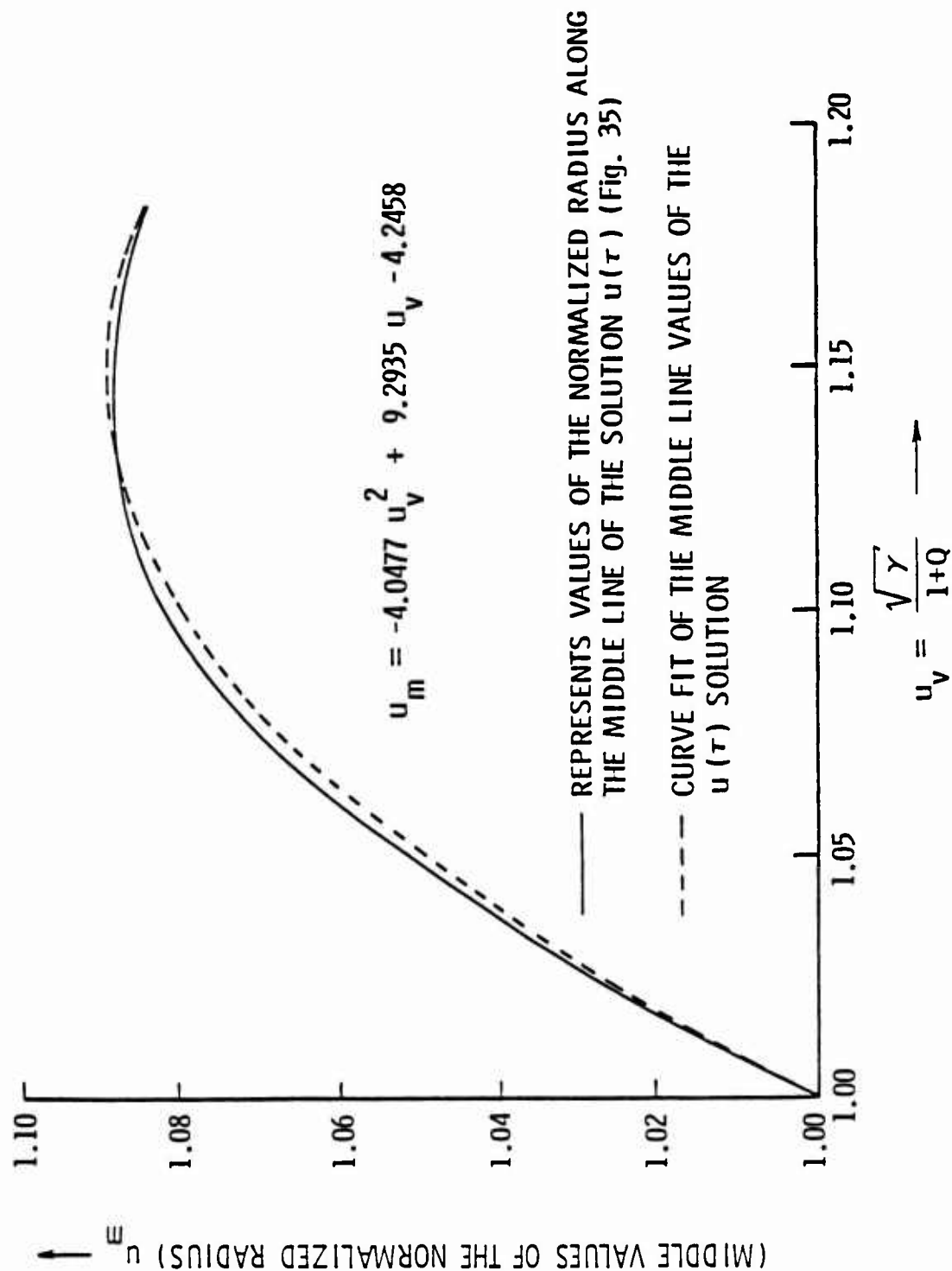
Figure 35. Curve Fit of the Middle Values of the Zero Order Solution, u_m, as a Function of the Parameter, u_v, which Defines the Location of the Vortex Point for Each Trajectory.
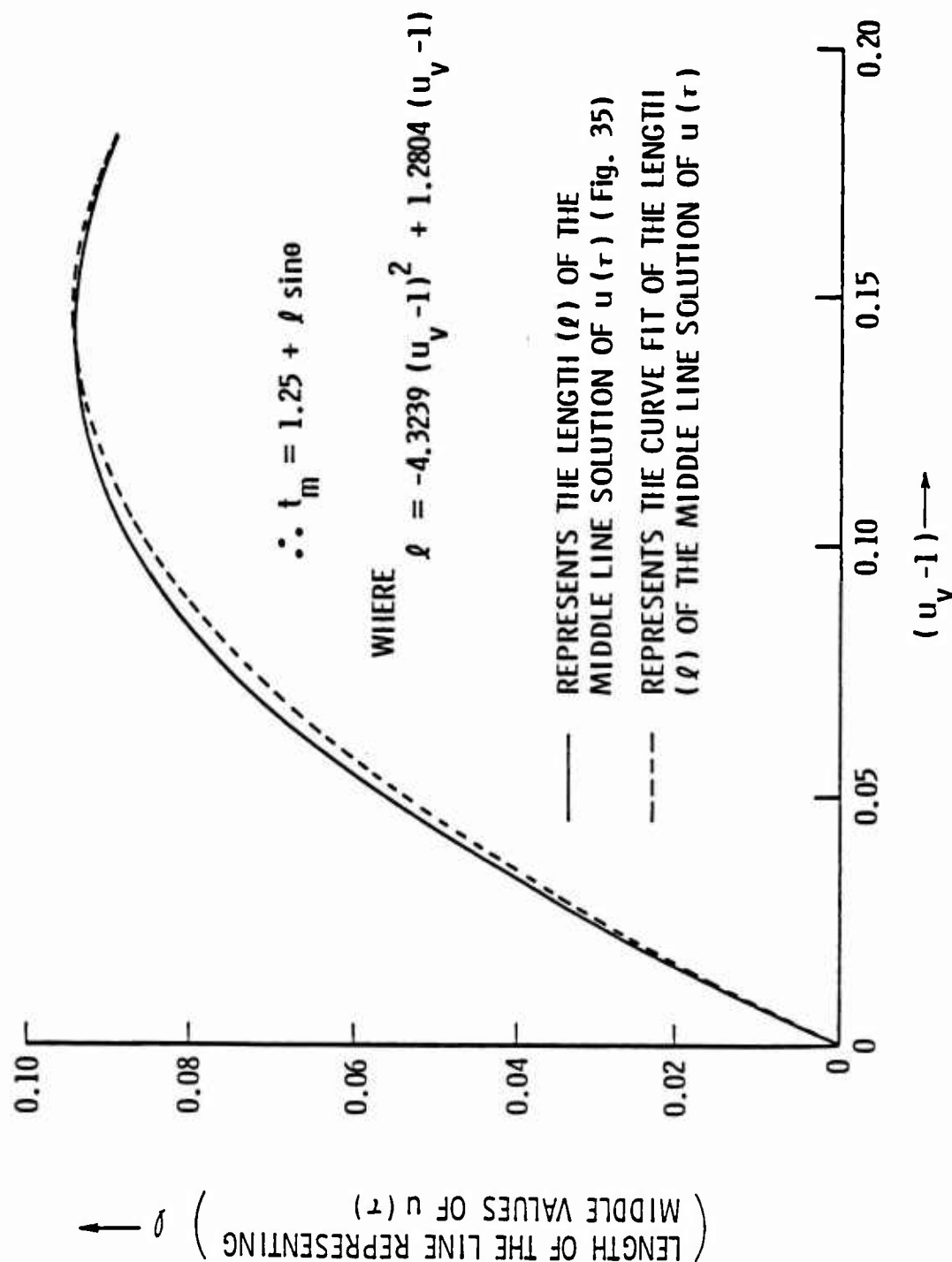
Figure 36. Curve Fit of the Middle Time Values of the Zero Order Solution as a Function of the Parameter, $(u_v - 1)$, which is a Parameter of the Vortex Point Location for Each Trajectory.
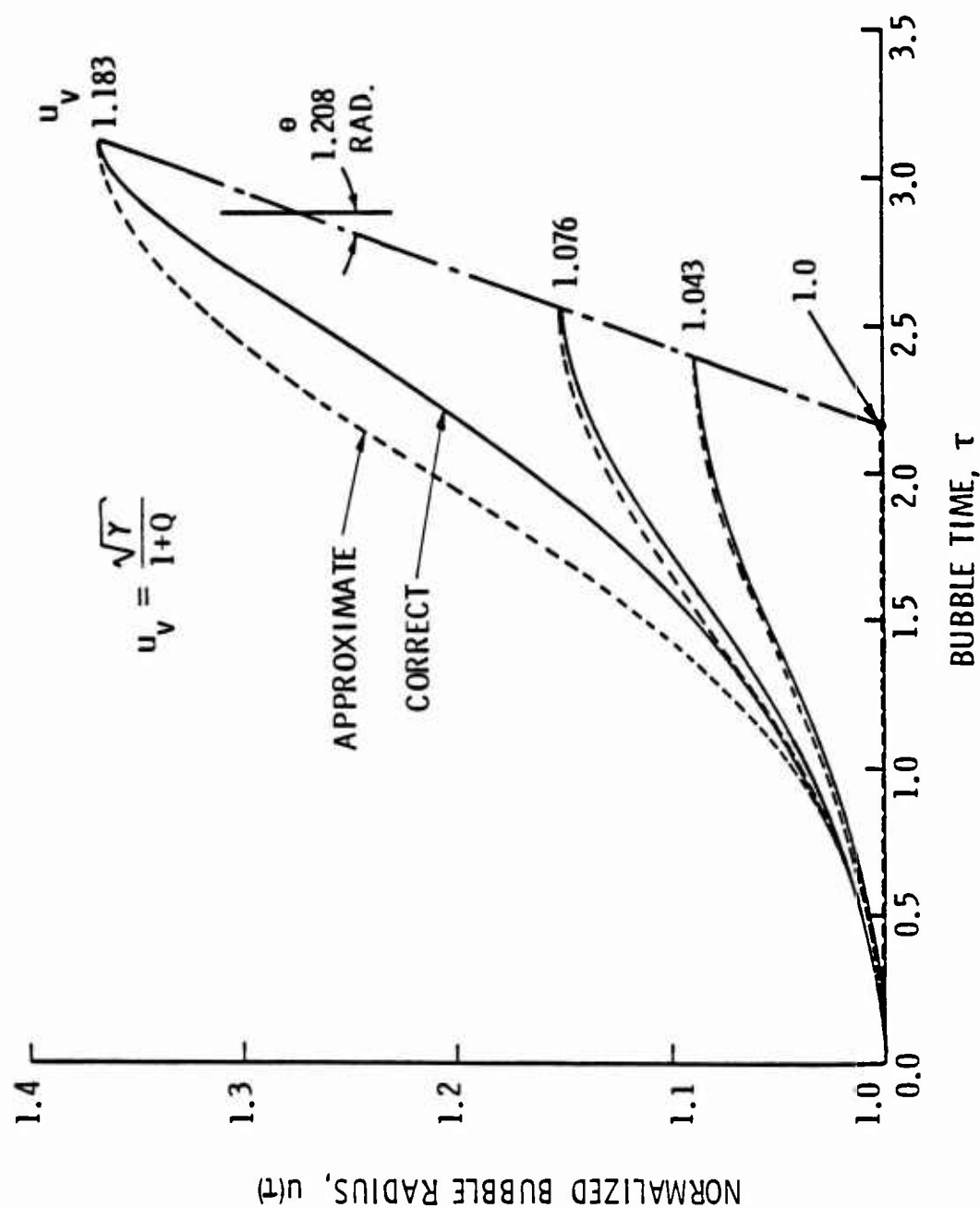
Figure 37. Comparison of an Approximating Curve Fit, Eq. (3.60), with the Numerical Data for the Zero Order Solution from Fig. 33.

$$e = A + B \cos\left(\pi \ \tau/\tau_f\right) + C \cos\left(2\pi \ \tau/\tau_f\right) \qquad (3.67)$$

and solving for the coefficients a new approximation of the zeroth order solution can be written. Using the conditions on e that

$$e = 0 \ @ \ \tau = 0$$

$$e = e_m \ @ \ \tau = \tau_m$$

$$e = 0 \ @ \ \tau = \tau_f$$

the coefficients A, B and C are written as

$$A = \frac{e_m}{1 - \cos\left(2\pi \ \tau_m/\tau_f\right)}$$

$$B = 0 \qquad (3.68)$$

$$C = - \ \frac{e_m}{1 - \cos\left(2\pi \ \tau_m/\tau_f\right)}$$

where e_m is the maximum error indicated for each value of u_v used. Plotting the values of e_m versus u_v, one can find an approximate curve fit for e_m which is written as

$$e_m = 0.09774 \ u_v^2 + 0.1585 \ u_v - 0.1136 \ . \qquad (3.69)$$

The parameters τ_m and τ_f were defined previously by Eqs. (3.64) and (3.65). A plot of Eq. (3.66) with (3.67), (3.68) and (3.69) gives an approximation of the zeroth order solution with a maximum error of ~ 1.5% for all possible values of u_v. Figure 38 shows the
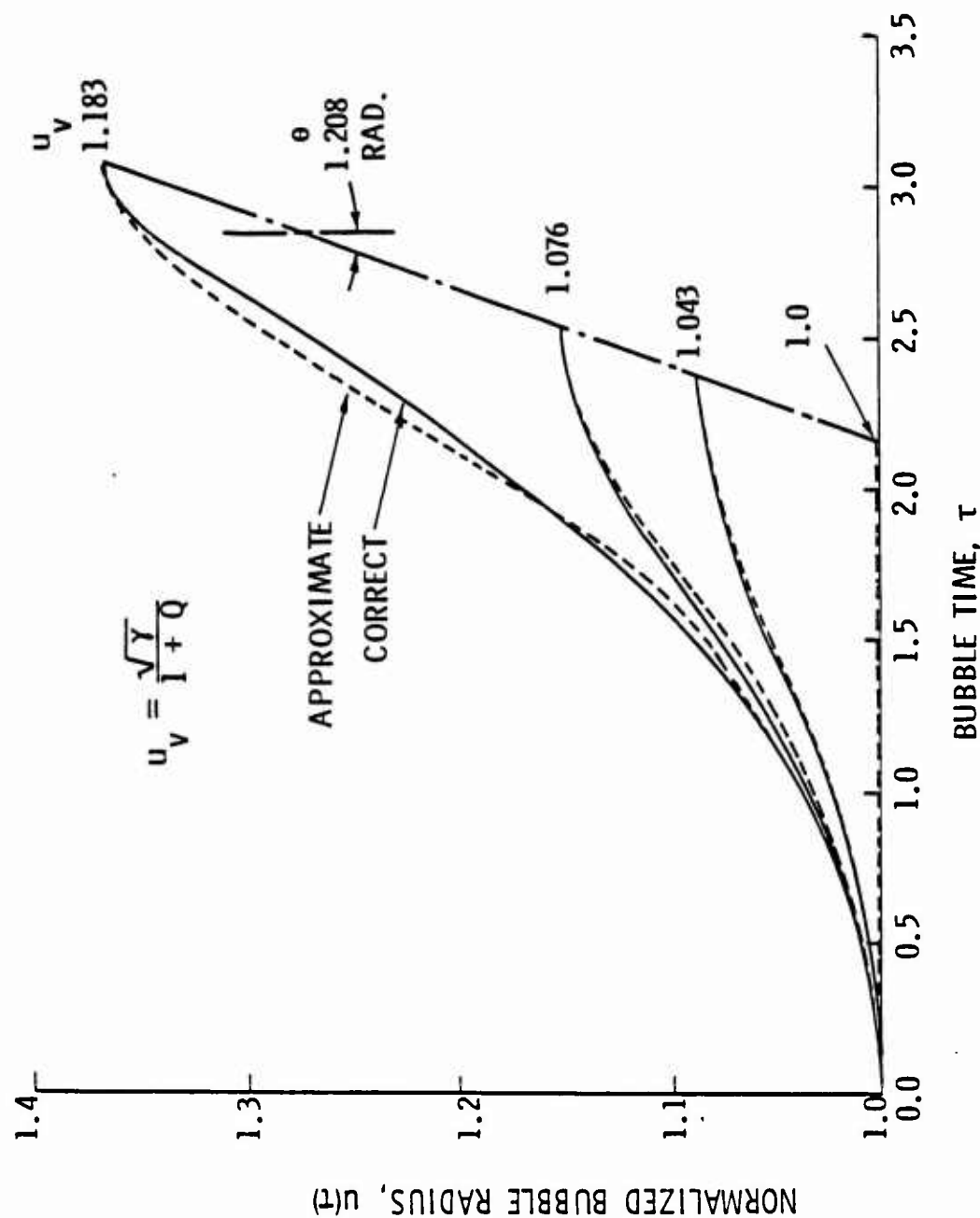
Figure 38. Revised Comparison of an Approximating Curve Fit, Eq. (3.60), using an Error Term, Eq. (3-69), to Approximate the Zero Order Solution, Fig. 33.

approximate and correct curves of the zeroth order solution plotted
as functions of the bubble time τ. Thus, a fairly accurate closed
form solution exists which can now be used to analyze the first
order equation.

CHAPTER 4

SUMMARY AND CONCLUSIONS

Having found a partial multiple scales solution of the pulse forced Rayleigh-Plesset equation of cavitation bubble dynamics, we must discuss and summarize the features of this work. First, before any analysis was performed, certain assumptions were made. It was assumed that one can model the dynamics of bubble-ring cavitation as though each bubble were a small isolated spherical bubble distributed throughout the flow. For the microbubbles of radius, R_o, distributed in the flow, all interactions with adjacent bubbles and walls were neglected. This assumption was made strictly in the interest of simplifying the problem. Also, it is assumed cavitation is initiated from these microbubbles of radius, R_o, in the minimum pressure region which is on the boundary of the submerged body. This fact was reflected in the formulation of the dynamical equation by using the pressure distribution. Recent measurements made by Holl and Carroll [1] revealed a very low pressure area along the surface of the body which, under special conditions, created an environment favorable for bubble growth. Using the specific pressure coefficient data collected by Holl and Carroll [1], a forcing function was derived as a function of the dimensionless bubble time, τ. The forcing function, $F(\tau)$, produced a pulse-like force which, when incorporated into the problem, caused the dynamical equation to be non-autonomous. Past

studies by Parkin [11] were made using a piecewise autonomous step
function to approximate the forcing function. This alleviated some
of the problems that would have arisen if the forcing function were
modeled as a parabola, which more closely represents the true nature
of the pulsed force. In an effort to capture the parabolic nature
of the forcing function, a parabolic fit was derived which satisfied
the physical requirements that the forcing function exhibited in the
region where vaporous growth occurred.

To this point, the development of the problem is straight-
forward. A differential equation and initial conditions exist
that describes the dynamics of growth along with a forcing
function representing the pulsed-force that acts on the
microbubbles. The problem seems like an ideal candidate for a
computer solution where detailed histories of the bubble growth
could be plotted using an appropriate numerical routine. The
problem with a numerical solution is the loss of the parametric
analysis of the critical parameters that govern cavitation
inception in this type of flow. Also, the differential operator
of the Rayleigh-Plesset equation does not directly lend itself
to a nice solution in terms of common well-behaved functions.
Therefore, parametric analysis of the various solutions coming
from the governing dynamical equation is nearly impossible.
Figure 39 is a prime example of how the solution varies with
respect to the various flow parameters. The curves in Fig. 39
represent isothermal cavitation bubble growth in response to
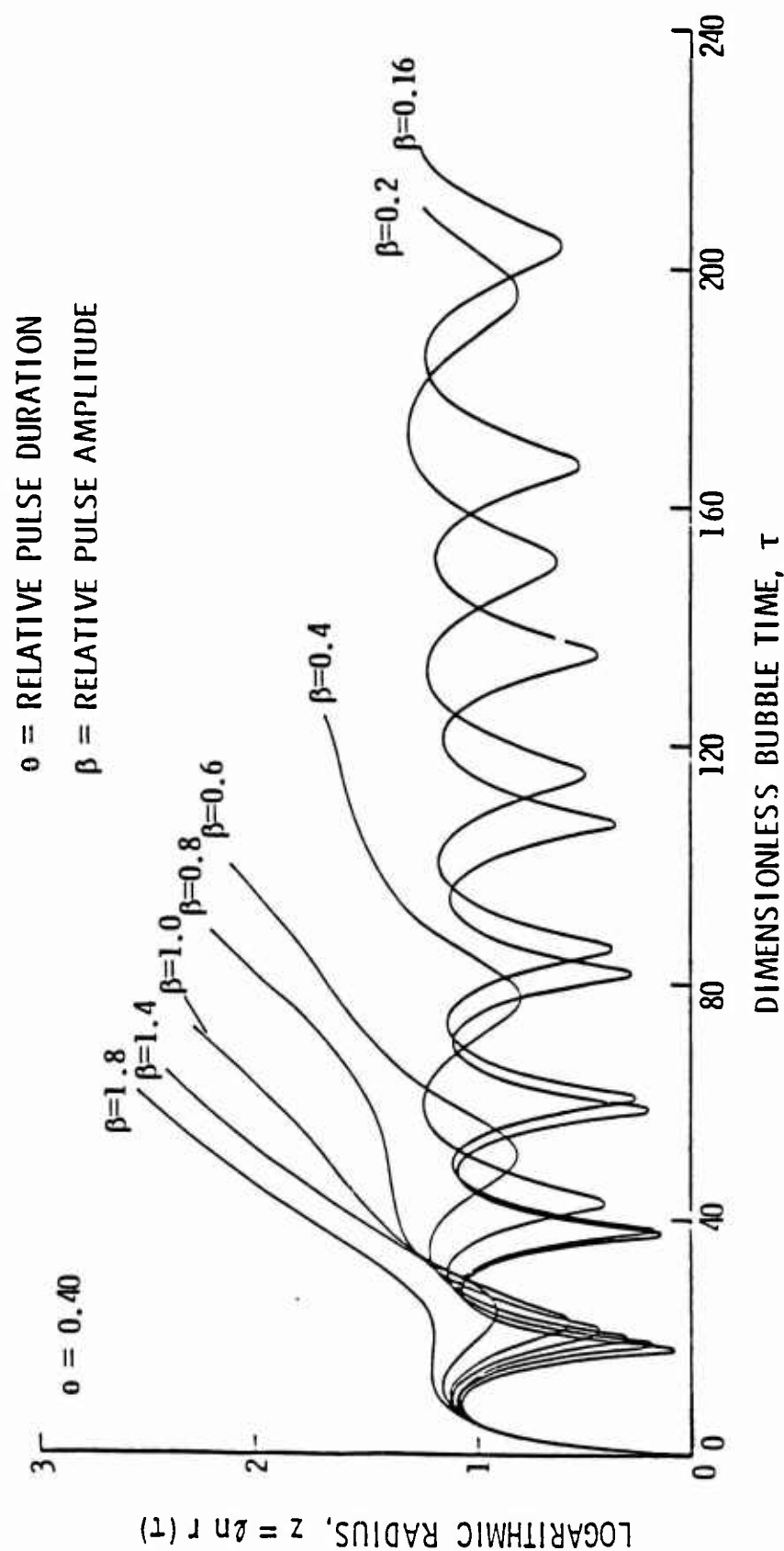
Figure 39(a). Isothermal Cavitation-Bubble Growth Curves in Response to Parabolic-Pulse Forcing Functions.
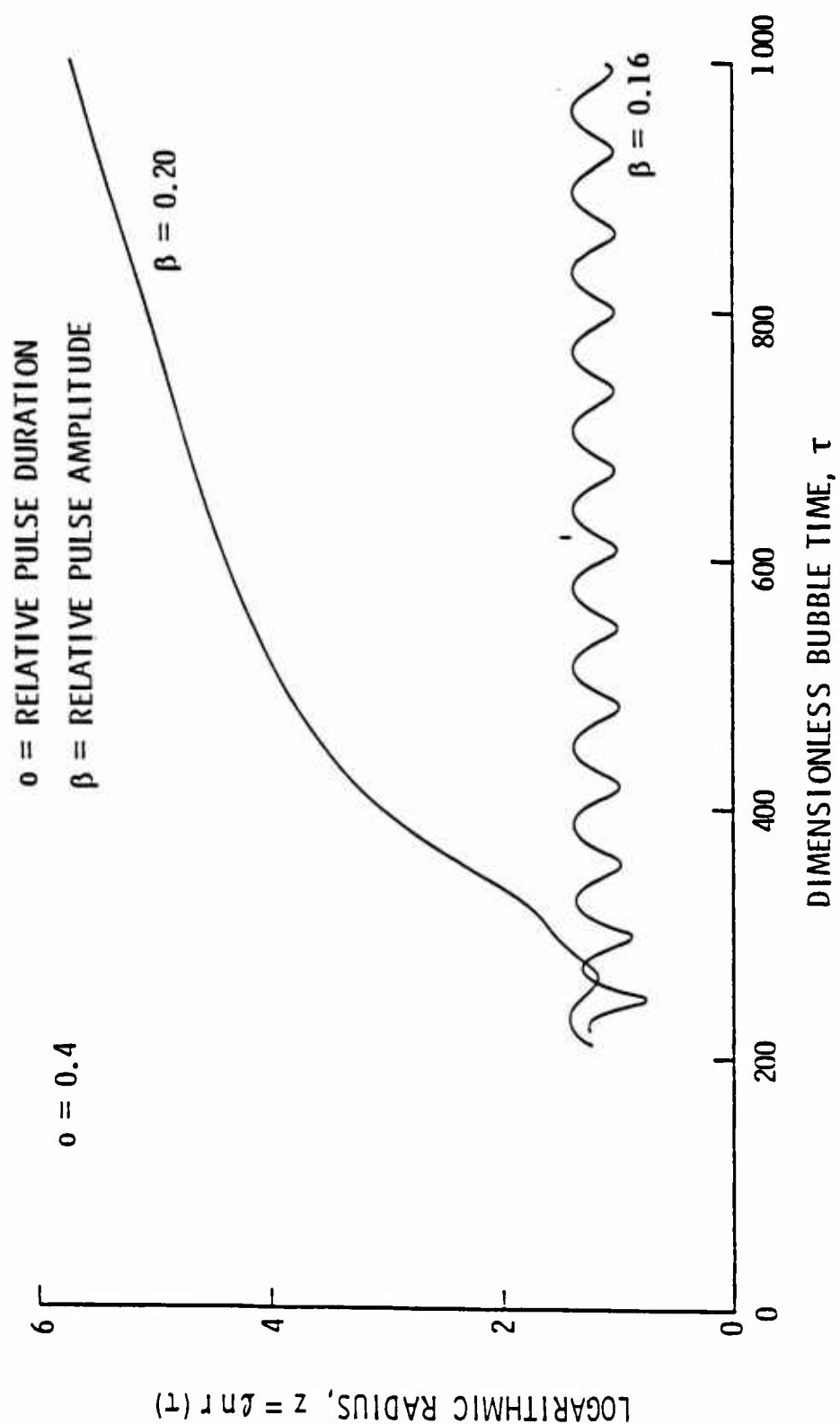
Figure 39(b). Isothermal Cavitation-Bubble Growth Curves in Response to Parabolic-Pulse Forcing Functions.

single parabolic-pulse forcing functions. The transient response
is directly affected by the relative pulse height and relative
pulse duration. By understanding the parametric relationships
that define the growth, one can better analyze the specific flow
characteristics without relying on the computer to produce
detailed histories of growth.

On the other hand, certain information can be derived from
the numerical solutions as shown in Fig. 39. The curves show
essentially no growth for certain values of the parameter β while
higher values of β cause explosive growth. One can predict the
existence of two different classes of bubble growth where the
interface between the two classes of growth is a particular cutoff
value of β. Analysis of the governing equations should then
reveal a parametric relationship that allows one to predict that
cutoff value of β. It should be noted that the curves in Fig. 39
are unpublished results obtained by Parkin under the direction of
M. S. Plesset. Also, the parameters shown in Fig. 39 pertain to
Parkin's work.

Using a multiple scales analysis, a series of differential
equations and initial conditions representing the zeroth, first
and second orders of ϵ are derived. From the zeroth order
equation, the global representation of the phase-plane trajectories
and corresponding vortex and saddle points are found. If the
autonomous form of the trajectory equation is plotted, then the
saddle point disappears and the trajectories become closed-loop

paths centered around a vortex point. The location of this vortex point can be located rather precisely using Liapunov's method or the corresponding potential energy curve.

An important result of the phase-plane analysis for the autonomous zeroth order equation is that a critical condition was found which represents the point of separation between two physically distinct types of motion. The trajectories that lie to the left of this critical point are representative of small scale flaccid air bubble oscillations while those to the right have a somewhat larger amplitude of oscillation due to vaporous growth. The critical parameter that defines the various trajectories is

$$u_v = \frac{\sqrt{\gamma}}{1 + Q} \cdot \tag{3.31}$$

In particular, the parameter, u_v, defines the location of the vortex point for each trajectory. For u_v greater than one, the vortex point and corresponding trajectory lie to the right of the initial condition. For u_v less than one, the vortex point and trajectory lie to the left of the initial condition. Because this work concerns itself primarily with vaporous growth, we have considered only values of u_v greater than one.

Having defined the phase-plane trajectories for the zeroth order autonomous form of the Rayleigh-Plesset equation, an approximate solution to the zeroth order equation was found. From the trajaectory equations one can write the bubble time equation for τ in quadrature form as

$$\tau = \int_{u=1}^{u} \frac{x^2 dx}{\sqrt{\frac{2\gamma}{(1+0)^5} x \ln x - \frac{1}{(1+0)^3} (x^3 - x)}} \quad . \tag{4.1}$$

Equation (4.1) is generally solved numerically, but since a parametric solution is desired, an approximate solution is obtained by fitting the uℓnu function with a cubic polynomial. The resulting integral is solved using a Table of Elliptic Integrals. The solution, which is expressed in terms of incomplete elliptic integrals of the first, second and third kinds and a product of Jacobian elliptic functions, is dependent on the roots of the denominator of Eq. (4.1). The roots of the denominator are found rather easily using the fact that one of the roots is equal to unity. This stems from the phase-plane trajectories which all originate from the point u = 1. Thus, the modified cubic in the denominator can be reduced to a quadratic form which is subsequently factored using the quadratic-equation. The roots are then ordered from the largest to the smallest which allows one to calculate the appropriate solution to the integral.

Since the solution is not readily invertible, an approximate inverse solution of the form

$$u = (1 - e)[A + B \cos \omega t + C \cos 2\omega t] \tag{4.2}$$

where A, B, C and w are functions of u_v. The error parameter, e, simply reduces the error of the approximate trigonometric inverse. Use of Eq. (4.2) allows one to look at one-half of a period for a particular value of u_v. Thus, a parametric study of the

approximate solution u as a function of the parameter u_v. Therefore an approximate solution to the zeroth-order autonomous Rayleigh-Plesset equation exists that describes the growth of the bubble radius as a function of bubble time, τ.

It is important to note that this work concerns itself solely with cavitation inception. At no time does this formulation allow for recirculation of the nuclei within the laminar separation bubble. If the theory were concerned with desinence, then the dynamical equation and solution would be very different.

Finally, after considering the approximations that have been made to derive a solution to the zeroth order Rayleigh-Plesset equation, a comparison of the results is made. One can see there is good agreement between the amplitudes of oscillation shown in Fig. 39 with the amplitudes shown in Fig. 33. This apparent consistency between the older results of Fig. 39 and the results achieved by use of the multiple scales analysis is encouraging. Though the results of Fig. 33 do not show the explosive bubble growth that the older results exhibit, this matter will be dealt with in the first-order solution.

REFERENCES

(1)   Holl, J. William, and Carroll, James A., "Observations of the
      Various Types of Limited Cavitation on Axisymmetric Bodies,"
      Journal of Fluids Engineering, Vol. 103, pp. 415-424 (September
      1981).

(2)   Carroll, J. R., "Observations of the Effects of Boundary Layer
      and Nuclei on Cavitation of Axisymmetric Bodies, M.S. Thesis,
      Department of Aerospace Engineering, The Pennsylvania State
      University (August 1981).

(3)   Parkin, B. R. and J. W. Holl, "Incipient Cavitation Scaling
      Experiments for Hemispherical and 1.5 Caliber Ogive-Nosed
      Bodies," Report NOrd 7958-264, Applied Research Laboratory,
      The Pennsylvania State University (May 1954).

(4)   Arakeri, V. H., "A Note on the Transition Observations on an
      Axisymmetric Body and Some Related Fluctuating Wall Pressure
      Measurements," ASME Journal of Fluids Engineering, Vol. 97,
      (March 1976).

(5)   Keller, A. P., "The Influence of the Cavitation Nucleus
      Spectrum on Cavitation Inception, Investigated with a
      Scattered Light Counting Method," Journal of Basic
      Engineering, pp. 917-925 (December 1972).

(6)   Brockett, T., "Some Environmental Effects on Headform
      Cavitation Inception," Report No. 3974, David W. Taylor
      Naval Ship Research and Development Center, Bethesda, MD
      (October 1972).

(7)   Arakeri, V. H., "Viscous Effects of Inception and Development
      of Cavitation on Axisymmetric Bodies, Ph.D. Thesis, California
      Institute of Technology (1973).

(8)   Arakeri, V. H., and A. J. Acosta, "Viscous Effects in the
      Inception of Cavitation on Axisymmetric Bodies,"
      ASME Journal of Fluids Engineering, Vol. 95, No. 4, pp. 519-528
      (December 1973).

(9)   van der Meulen, J. H. J., "A Holographic Study of Cavitation
      on Axisymmetric Bodies and the Influence of Polymer Additives,"
      Publication No. 509, Netherlands Ship Model Basin,
      Wageningen, The Netherlands (1976).

(10) Gates, E. M., "The Influence of Freestream Turbulence,
      Freestream Nuclei Populations and a Drag-Reducing
      Polymer on Cavitation Inception on Two-Axisymmetric
      Bodies," Ph.D. Thesis, California Institute of Technology
      (April 1977).

REFERENCES [continuation]

(11) Parkin, B. R., "A Theory for Cavitation Inception in a Flow having Laminar Separation," ARL/PSU TM 79-198, Applied Research Laboratory, The Pennsylvania State University (November 19, 1979).

(12) CRC Math Tables, 25th Edition, Academic Press (April 1978).

(13) Byrd, P. F. and M. D. Friedman, Handbook of Elliptic-Integrals for Engineers and Scientists, Springer-Verlag, New York, NY (1971).

(14) Cole, J. D. and J. Kevorkian, Perturbation Methods in Applied Mathematics, Springer-Verlag, New York, NY (1981).

(15) Van Dyke, M., Perturbation Methods in Fluid Mechanics, Parabolic Press, Palo Alto, CA (1975).

(16) Nayfeh, A. H. and D. T. Mook, Nonlinear Oscillations, John Wiley & Sons, New York, NY (1979).

(17) Ferziger, J. H., Numerical Methods for Engineering Applications, John Wiley & Sons, New York, NY (1981).

(18) Ma, J. T. S. and P. K. C. Wang, "The Effect of Initial Air Content on the Dynamics of Bubbles in Liquids," I.B.M. Journal of Research and Development, Vol. 6, No. 4, p. 472 (October 1962).

(19) Bender, C. M. and S. A. Orszag, Advanced Mathematical Methods for Scientists and Engineers, McGraw-Hill, New York, NY (1978).

(20) Robertson, J. M. McGinley, J. H. and Holl, J. W., "On Several Laws of Cavitation Scaling," La Houille Blanche, No. 1, pp. 540-554 (September 1957).

APPENDIX A.   FORTRAN CODE DISCUSSION

A1.   The Basic Algorithm

In the basic formulation of the problem, it was required that we could perform a parabolic curve fit as well as numerically integrate the experimental C_p data obtained by Holl and Carroll [1]. The form of the integral arose when an expression for the dimensionless bubble time was derived using the kinematics of the flow. During the development of the Fortran code, care was taken to satisfy all the criteria laid down in Chapter 2. The code was designed to handle an odd or even number of data points and to output values of the computed integral, the coefficients of the parabolic curve fit, the integrand and the experimental data.

The first step of the code read in the data in a form x_i, $f(x_i)$. These data were then used to compute the coefficients A, B and C of the curve fit. The coefficients were then used to calculate the integral contained within the bubble time equation, Eq. (2.8).

Calculation of the coefficients A, B and C was performed by expanding a third order Lagrange Polynomial, $P_j(s)$, where

$$P_j(s) = \frac{\displaystyle\prod_{\substack{i=0 \\ i \neq j}}^{n} (s - s_i)}{\displaystyle\prod_{\substack{i=0 \\ i \neq 0}}^{n} (s_j - s_i)} \quad . \tag{A.1.1}$$

The polynomial was then multiplied by the functional value $f(s_j)$ for each data point and summed n times, where n corresponds to the degree of the polynomial approximation desired. Thus, the polynomial has the form

$$p_n(s) = \sum_{j=0}^{n} f(s_j) P_j(s) \qquad (A.1.2)$$

where $p_n(s)$ is the desired polynomial of degree n which exactly fits n data points. Equation (A.1.2) represents the form of the polynomial used to fit the experimetal data taken by Holl and Carroll [1]. The formulae for these calculations are derived by expanding Eq. (A.1.2) and using n = 3 to perform a parabolic approximation across n = 3 data points. A parabolic fit was derived for each set of the three consecutive data points beginning with the first data point. The coefficients A, B and C were calculated for consecutive triads of data points until all points were used. The result is a set of coefficients A, B and C that represent the coefficients of a piecewise parabolic approximation of consecutive triads of data. This type of curve fit proved advantageous for fitting a curve over the irregular portions of the pressure distribution while use of a single parabola resulted in a poor fit due to its inability to capture the irregularities near the separation point and the pressure recovery region.

Since a smooth representation of the pressure distribution along the arc of the body was desired, several points were interpolated between the experimental points using the appropriate

set of parabolic coefficients derived from the curve fit. The resulting curve fit pressure distribution along with the experimental data taken by Holl and Carroll [1] are shown in Fig. 2. By using the interpolated pressure distribution, a better representation of the initial conditions was made.

Having calculated a piecewise parabolic curve fit of the experimental data, an integration routine using the coefficients A, B and C of the curve fit was derived. The integration procedure was designed to integrate any integrand that could be approximated by the curve fit. In the case of the experimental data, the integrand was written as

$$C_p(s) = As^2 + Bs + C \quad . \tag{A.1.3}$$

The integral I(s) was evaluated as the following definite integral,

$$I(s) = \int_{s_1}^{s_2} (As^2 + Bs + C)ds = [\frac{A}{3} s^3 + \frac{B}{2} s^2 + Cs] \Big|_{s_1}^{s_2} \quad . \tag{A.1.4}$$

Therefore,

$$I(s) = (s_2 - s_1)[\frac{A}{3} (s_2^2 + s_2 s_1 + s_1^2) + \frac{B}{2} (s_2 + s_1) + C] \tag{A.1.5}$$

which represents the value of the integral I(s) across the specified time interval.

When computing the bubble-time parameter from Eq. (2.8) the integrand, one writes f(s) as

$$f(s) = \frac{1}{\sqrt{1 - C_p(s)}} \; . \tag{A.1.6}$$

Substitution of the curve fit for $C_p(s)$ into Eq. (A.1.6) produced tabulated values of the integrand $f(s)$ for different arc length positions along the body. Application of the parabolic curve fit routine to Eq. (A.1.6) produces a piecewise parabolic approximation of the integrand $f(s)$ which is then integrated exactly as $C_p(s)$ was integrated using Eq. (A.1.5).

Because the code is required to produce an output point for every input point and to handle an even or odd number of data points, two separate integration formulae are used. The first integration formula, I_1, integrates across the first two points in a triad of data points while the second formula, I_2, integrates across the entire triad of data points. By integrating across consecutive triads of data, i.e.,

$$[x(1),x(2),x(3)] \; , \; [x(3),x(4),x(5)], \; \ldots \; ,$$

one can get a total sum for the integral found in Eq. (2.8) which allows one to find the bubble time for different arc length positions. Figure Al shows how the integral is computed for an even or odd number of data points. When n = 5, there is an even number of intervals and I_1 and I_2 are computed across two triads of data points. When n = 6, there is an odd number of intervals and I_1 amd I_2 are computed across two triads of data points and across one group of two data points. Since I_2 requires three data
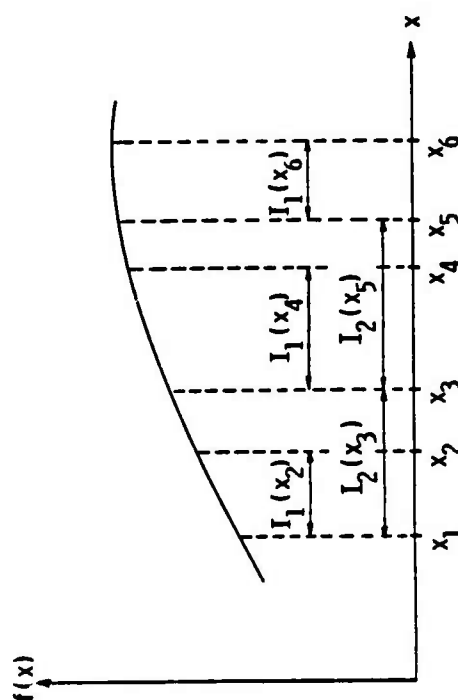
Figure A1. Schematic Diagram Showing the Range across which the Integrals I_1 and I_2 are Calculated.

For n odd (n = 5)

$\underline{i}$	Data Points	I_1 Calculation	I_2 Calculation
i = 1	(x_1, x_2, x_3)	$I_1(x_2) = I_1(x_2 - x_1)$	$I_2(x_3) = I_2(x_3 - x_1)$
i = 3	(x_3, x_4, x_5)	$I_1(x_4) = I_1(x_4 - x_3) + I_2(x_3)$	$I_2(x_5) = I_2(x_5 - x_3) - I_2(x_3)$

For n even (n = 6)

$\underline{i}$	Data Points	I_1 Calculation	I_2 Calculation
i = 1	(x_1, x_2, x_3)	$I_1(x_2) = I_1(x_2 - x_1)$	$I_2(x_3) = I_2(x_3 - x_1)$
i = 3	(x_3, x_4, x_5)	$I_1(x_4) = I_1(x_4 - x_3) + I_2(x_3)$	$I_2(x_5) = I_2(x_5 - x_3) - I_2(x_3)$
i = 5	(x_5, x_6)	$I_1(x_6) = I_1(x_6 - x_5) + I_2(x_5)$	$I_2(x_7) = 0.0$

points across which it is calculated we must set I_2 at $x(7)$ equal

to zero. This procedure is used across the entire set of data to

produce the required I_i for $i = 1,2,...,n$. Figure A2 is the flow

chart for the integration procedure. It satisfies all requirements

put forth in Chapter II but it does not describe the procedures

for computing the coefficients A, B and C. The specifics of these

calculations are described in Section 3 of Appendix A.

A2. Evaluation of the Stagnation Point Singularity

Flow about a symmetrical hemispherical headform produces a

stagnation point at the nose of the headform characterized by a

zero fluid velocity and a maximum pressure. The history of a very

small flaccid air bubble traveling close to the stagnation

streamline would show a constantly decreasing radius up to the

stagnation point where a minimum radius occurs. Past th

stagnation point along a meridian on the body the flaccid bubble

would experience an increasing radius. It should be noted that

we speak of the bubble as traveling close to the stagnation

streamline and not exactly on the stagnation streamline because

it would take an infinite amount of time to reach the stagnation

point as it travels from infinity. Also, along the body arc the

flow velocity is zero, but the bubble is traveling in the
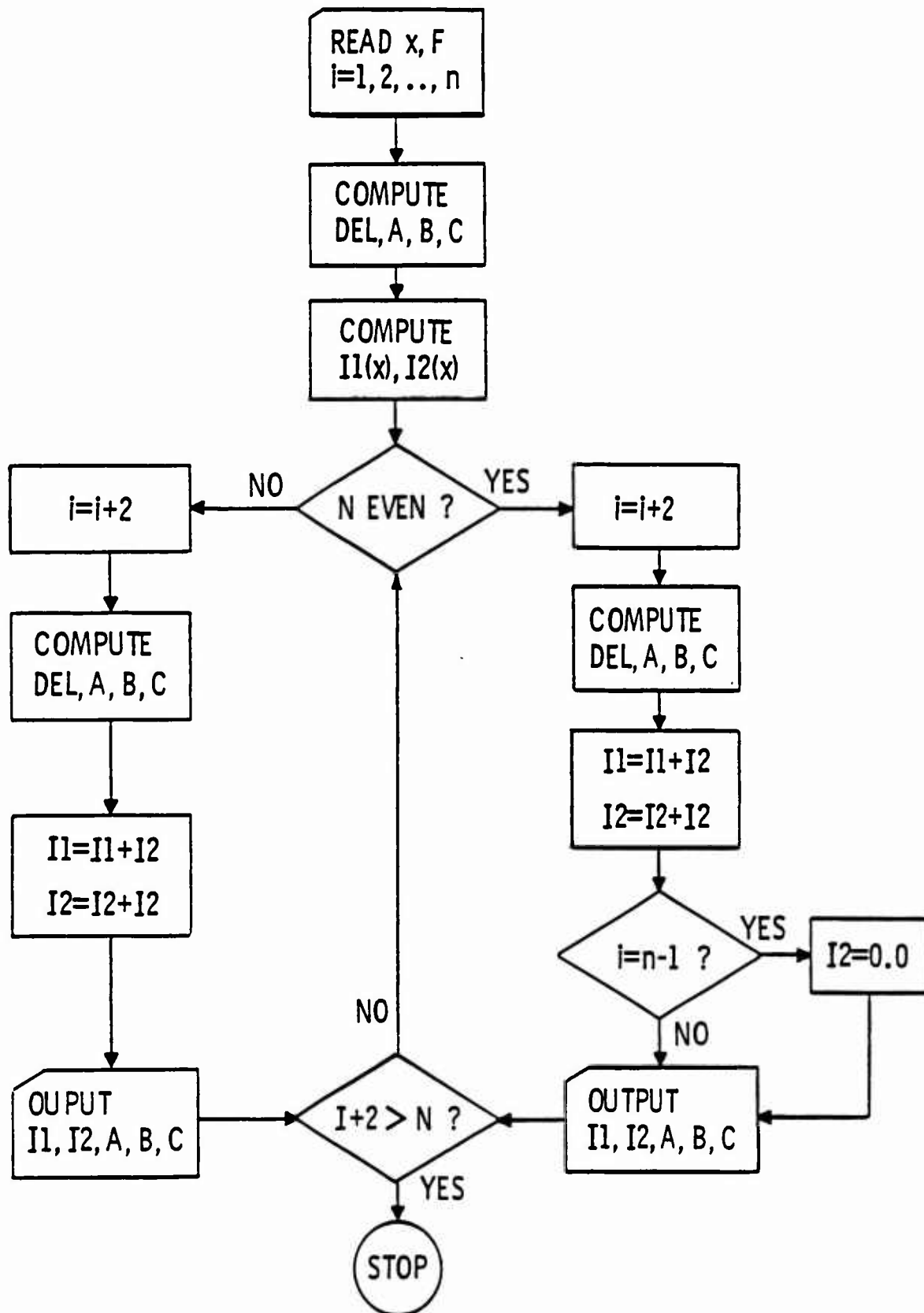
boundary layer and not on the body.

Figure A2. Flow Chart Representing the Algorithm by Which the
Integral is Calculated for an Even or Uneven Number
of Data Points.

If we define a pressure coefficient, C_p, as

$$C_p = \frac{P - P_o}{1/2\rho V_o^2} \qquad (A.2.1)$$

we could expect to see a minimum bubble radius at a maximum pressure coefficient of unity and a maximum bubble radius at a minimum pressure coefficient, $C_{P_{min}}$, provided that no cavitation takes place. The definition of the pressure coefficient leads to a singularity when computing the dimensionless translation time for a bubble on the stagnation streamline. As determined earlier, the dimensionless time was written as

$$\tau_i = \frac{D}{V_o} \sqrt{\frac{2\sigma}{\rho R_o^3}} \int_{s_1}^{s_i} \frac{ds}{\sqrt{1 - C_p(s)}} \qquad i = 1, 2, \ldots, n \qquad (A.2.2)$$

where the singularity in the integrand is an integrable square root singularity. Since the computer code was not designed to integrate across a singularity, an analytic technique was used on the interval containing the singularity while the remainder of the data was integrated by use of the computer code.

The interval containing the singularity was composed of the following points:

C_p	s
1.0000	0.00000
0.9895	0.00279
0.9791	0.00557

Since the computer code produced a piecewise parabolic approximation of the experimental data, we will write the equation for C_p across the interval containing the singularity as

$$C_p(s) = As^2 + Bs + 1 \quad . \tag{A.2.3}$$

Evaluation of the coefficients across the interval containing the singularity gives

$$A = - 0.87307$$
$$B = - 3.74416 \quad .$$

Substituting $C_p(s)$ into the integral one gets

$$I(s) = \int_{s_1}^{s_1} \frac{ds}{\sqrt{- As^2 - Bs}}$$

which when solved using math tables [12] one finds $I(s) = 0.000983$. This value of I is then added onto the values of the integral for successive intervals as computed by the computer code. Figure A3 and Fig. A4 show the integrand, $f(s)$,

$$f(s) = \frac{1}{\sqrt{1 - C_p(s)}}$$

and the integral, $I(s)$,

$$I(s) = \int_{s_1}^{s_1} \frac{ds}{\sqrt{1 - C_p(s)}}$$

each plotted against the body arc length s. It is clearly seen that the singularity at the nose of the body causes the integrand to increase to infinity but that the integral at the singularity is null.
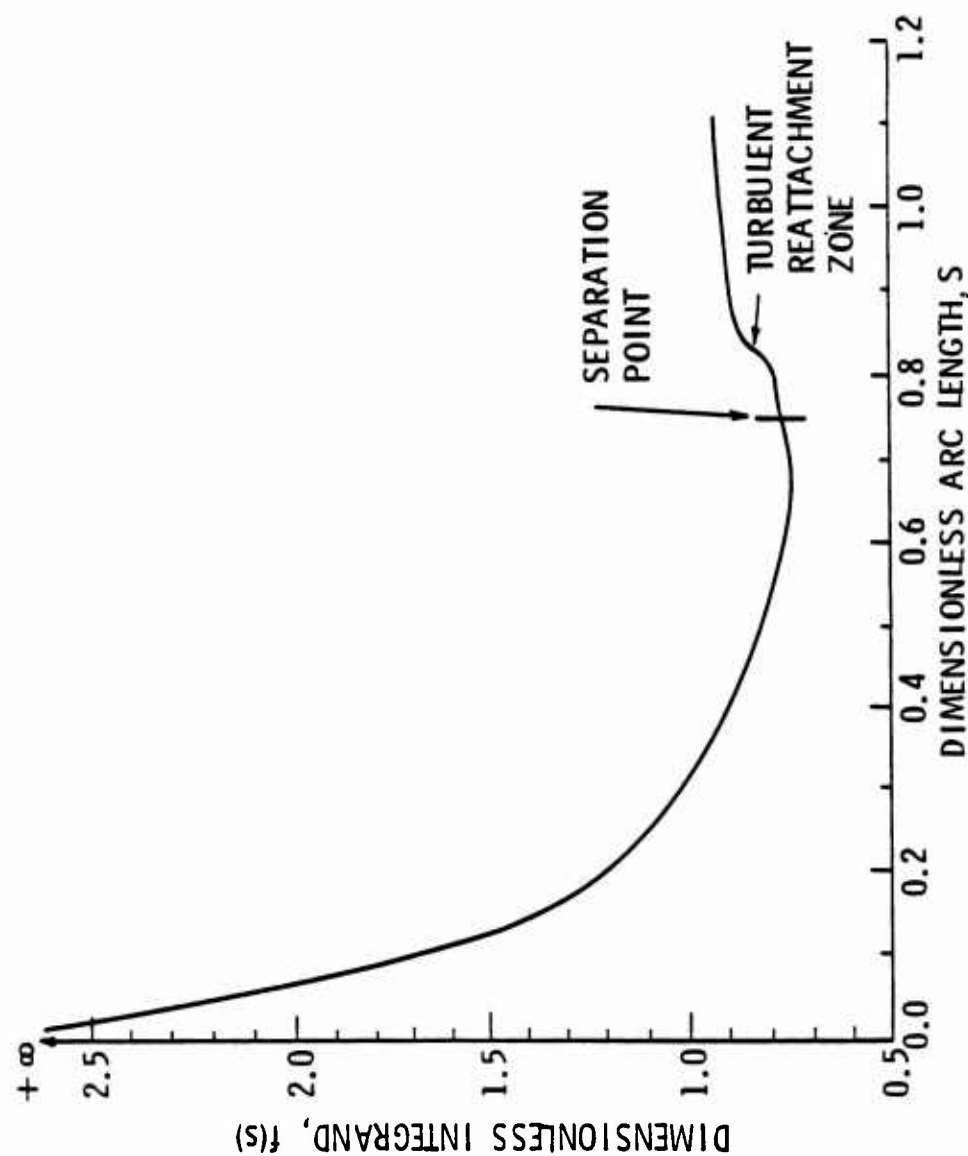
Figure A3. Plot of the Dimensionless Integrand $f(s) = \dfrac{1}{\sqrt{1 - C_p(s)}}$

as a Function of the Dimensionless Arc Length along
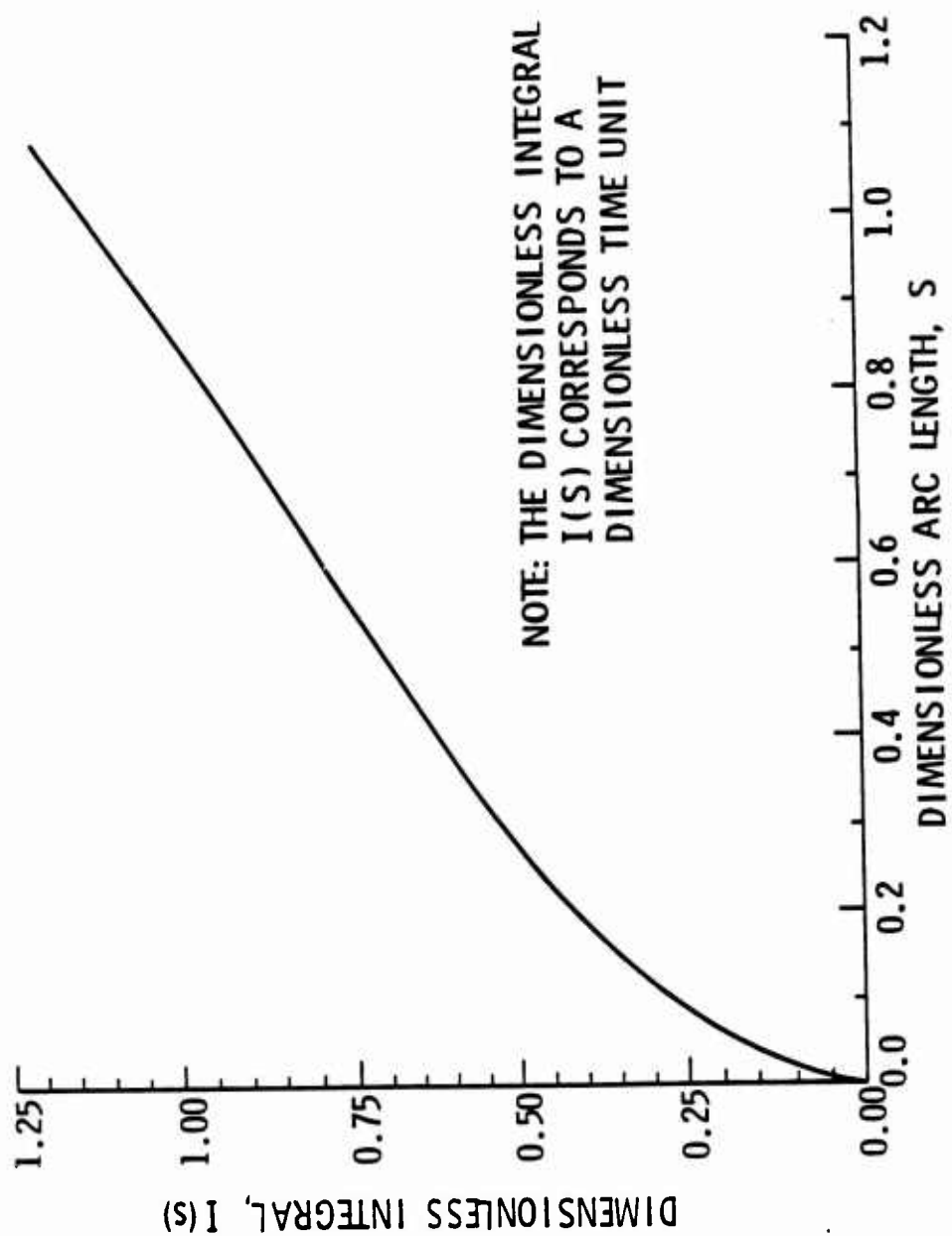
the Headform.

NOTE: THE DIMENSIONLESS INTEGRAL I(S) CORRESPONDS TO A DIMENSIONLESS TIME UNIT

Figure A4. Plot of the Dimensionless Integral I(s) Which Represents the Dimensionless Bubble Time as a Function of the Dimensionless Arc Length.

A3. Derivation of the Computer Code Formulae

Having tabulated information on the pressure distribution around a hemispherical headform, one must be able to integrate the data based on the bubble time integral discussed in Chapter 2. It was stated before that these data are unevenly spaced and may be odd or even in number. Also, since we desire one output point for each input point, we need two integration formulae to do this. For tabulated data of the form $(x_i, f(x_i))$ where $i = 1,2,\ldots,n$ is being the total number of data points, the integration equation will be developed for a triad of data points and then used across each successive triad until all data have been used.

The procedure for defining the integration formulae begins by calculating a parabolic curve fit for each triad of data. The coefficients A, B and C are calculated using Eqs. (A.1.1) and (A.1.2) as discussed in Appendix A. By expanding these equations for $i = 1,2,3$ one gets

$$P_n(s) = \sum_{i=1}^{3} f(s_i) \frac{\prod_{\substack{j=1 \\ i \neq j}}^{3} (s - s_j)}{\prod_{\substack{j=1 \\ i \neq j}}^{n} (s_j - s_i)} = f(s_1) \frac{(s - s_2)(s - s_3)}{(s_1 - s_2)(s_1 - s_3)}$$

$$+ f(s_2) \frac{(s - s_1)(s - s_3)}{(s_2 - s_1)(s_2 - s_3)} + f(s_3) \frac{(s - s_1)(s - s_2)}{(s_3 - s_1)(s_3 - s_2)} \ .$$

Factoring like powers of s one gets an equation resembling a parabola which looks like

$$p_n(s) = s^2 \left[\frac{f_1(s_2 - s_3)}{(s_1 - s_2)(s_1 - s_3)(s_2 - s_3)} + \frac{f_2(s_3 - s_1)}{(s_2 - s_3)(s_2 - s_1)(s_3 - s_1)} + \frac{f_3(s_1 - s_2)}{(s_3 - s_1)(s_3 - s_2)(s_1 - s_2)} \right]$$

$$+ s \left[\frac{f_1(s_2 + s_3)(s_3 - s_2)}{(s_1 - s_2)(s_1 - s_3)(s_2 - s_3)} + \frac{f_2(s_1 + s_3)(s_1 - s_3)}{(s_2 - s_3)(s_2 - s_1)(s_3 - s_1)} + \frac{f_3(s_1 + s_2)(s_2 - s_1)}{(s_3 - s_1)(s_3 - s_2)(s_1 - s_2)} \right]$$

$$+ \left[\frac{f_1(s_2 s_3)(s_2 - s_3)}{(s_1 - s_2)(s_1 - s_3)(s_2 - s_3)} + \frac{f_2(s_1 s_3)(s_3 - s_1)}{(s_2 - s_3)(s_2 - s_1)(s_3 - s_1)} + \frac{f_3(s_1 s_2)(s_1 - s_2)}{(s_3 - s_1)(s_3 - s_2)(s_1 - s_2)} \right]$$

The above equation can be written in a more simplified form as

$$p_n(s) = (As^2 + Bs + C)/\Delta$$

where

$$A = f_1(s_2 - s_3) + f_2(s_3 - s_1) + f_3(s_1 - s_2)$$

$$B = f_1(s_2 + s_3)(s_3 - s_2) + f_2(s_1 + s_3)(s_1 - s_3) + f_3(s_1 + s_2)(s_2 - s_1)$$

$$C = f_1(s_2 s_3)(s_2 - s_3) + f_2(s_1 s_3)(s_3 - s_1) + f_3(s_1 s_2)(s_1 - s_2)$$

$$\Delta = s_1^2(s_2 - s_3) + s_2^2(s_3 - s_1) + s_3^2(s_1 - s_2) .$$

The parabolic form of curve fit can now be integrated across the appropriate limits to obtain the two integration formula required for obtaining an output point for each input point when the number of data points can be odd or even and the data are unevenly spaced. Therefore, we define the two integration formulae as I_1 and I_2 where

$$I_1 = \int_{s_1}^{s_2} p_n(s)\,ds$$

and

$$I_2 = \int_{s_1}^{s_3} p_n(s)\,ds \quad .$$

Upon evaluation of the definite integrals, one can write

$$I_1 = \frac{(s_2 - s_1)}{\Delta}\left[\frac{A}{3}\left(s_2^2 + s_1 s_2 + s_1^2\right) + \frac{B}{2}\left(s_2 + s_1\right) + C\right]$$

and

$$I_2 = \frac{(s_3 - s_1)}{\Delta}\left[\frac{A}{3}\left(s_3^2 + s_1 s_3 + s_1^2\right) + \frac{B}{2}\left(s_3 + s_1\right) + C\right] \quad .$$

These integration formulae can be used for any data which are tabulated in the form of s_i, $f(s_i)$ and can be modeled by successive parabolic curve fits according to the parameters A, B, C and Δ defined earlier in this section. One must keep in mind that the integration routine is only as good as the

curve fit since the coefficients of the curve fit play a major role
in the result of the integration. The remainder of Appendix A
will deal primarily with the accuracy of the curve fit and
integration formulae.

A4. Accuracy of the Parabolic Curve Fit

When using any type of numerical approximation, it is important
that the user be aware of the limitations and accuracy of the
particular approximation technique being used. Failure to use an
approximation technique with suitable accuracy could result in
erroneous calculations and analysis.

In this work, it was imperative that the approximation
technique used to calculate the piecewise parabolic curve fit
and numerical integration were extremely accurate. The curve
fit approximation was compared against a sample function and the
accuracy was checked for different interval lengths.

The sample function used was $f(x) = \sin x$. The first
interval length used was $Dx = 0.157$ for $x = 0$ to $x = \pi$. The
second interval length to be used was $Dx = 0.314$ for $x = 0$ to
$x = \pi$ while a third interval length of $Dx = 0.628$ was used
across $x = 0$ to $x = \pi$.

Execution of the code produced the coefficients of the
parabolic curve fit which was compared to the sample function.
When using the shortest interval, $Dx = 0.157$, the code
produced a curve fit accurate to five decimal places. Doubling
the interval length produced a curve fit accurate to four

decimal places. And when the interval length was made four times the first interval or Dx = 0.628, the accuracy dropped to three decimal places.

Due to the irregularities of the C_p data, several points were interpolated between the original data points. This effectively reduced the interval lengths so that the curve fit was accurate to five decimal places. Therefore, the method described in the previous sections of the Appendix produced a curve fit which allowed an accurate fit of the C_p data. Section 1 of Appendix A addressed the problem im more detail but the accuracy of the results will be given. Again, using a sample function to test the integration procedure against the parabolic coefficients of the curve fit needed to be calculated. For the same function $f(x) = \sin x$ from $x = 0$ to $x = \pi$ the value of the definite integral is exactly equal to 2. Using the parabolic coefficients in the integration procedure gave the value of the integral equal to 1.999977. This calculation was performed with an interval length of Dx = 0.157. Further calculations were performed on even and odd numbers of data points with longer and shorter interval and it was found that the accuracy of the integration procedure paralleled the accuracy of the curve fit. Thus, when using the curve fit routine and integration procedure in this work, the interval lengths were short enough to produce five decimal place accuracy.

APPENDIX B.   DATA TABULATION

B1.   Conversion of the Axial Length Data to Arc Length Data

Based on the geometry of the headform set forth in Fig. 1, the following equations are used to convert the axial length, x/D, which is the parameter that Holl and Carroll [1] measured the C_p data against, to a dimensionless arc length s. The parameter s was used throughout this work to describe the dimensionless arc length along the surface arc of the body.

For $0^\circ < \theta < 90^\circ$

$$s = \frac{1}{2} \cos^{-1} \left(1 - 2(x/D) \right)$$

For $\theta > 90^\circ$

$$s = 0.785 + \frac{x}{D}$$

It should be noted that for $\theta > 90^\circ$ the dimensionless arc length s increases the same as the parameter x/D due to the presence of the cylindrical afterbody. Therefore, the value of x/D is simply added on to the value of s beyond $\theta = 90^\circ$. Section 2 of Appendix B contains a tabulation of s versus x/D with the corresponding averaged values of C_p.

B2. C_p versus s (averaged)

x/D	s	C_p
0.000	0.000	1.0000
0.280	0.557	- 0.6168
0.335	0.617	- 0.7343
0.390	0.674	- 0.7812
0.430	0.715	- 0.7432
0.465	0.748	- 0.6578
0.480	0.765	- 0.6370
0.500	0.785	- 0.6163
0.515	0.800	- 0.6128
0.530	0.815	- 0.5518
0.545	0.830	- 0.4183
0.560	0.845	- 0.3303
0.575	0.860	- 0.2988
0.625	0.910	- 0.2307
0.675	0.960	- 0.2073
0.725	1.010	- 0.1805
0.775	1.060	- 0.1620
0.825	1.110	- 0.1443